University of New Mexico
UNM Digital Repository

Optical Science and Engineering ETDs | Engineering ETDs

1-28-2015

BEAM COMBINING OF FIBER LASERS AND VERTICAL EXTERNAL CAVITY SURFACE EMITTING LASERS USING VOLUME BRAGG GRATINGS

Chunte Lu

Follow this and additional works at: https://digitalrepository.unm.edu/ose_etds

Recommended Citation
Lu, Chunte. "BEAM COMBINING OF FIBER LASERS AND VERTICAL EXTERNAL CAVITY SURFACE EMITTING LASERS USING VOLUME BRAGG GRATINGS." (2015). https://digitalrepository.unm.edu/ose_etds/21

This Dissertation is brought to you for free and open access by the Engineering ETDs at UNM Digital Repository. It has been accepted for inclusion in Optical Science and Engineering ETDs by an authorized administrator of UNM Digital Repository. For more information, please contact disc@unm.edu.

Chunte Andrew Lu
Candidate

Optical Science and Engineering, Physics & Astronomy
Department

This dissertation is approved, and it is acceptable in quality and form for publication:

Approved by the Dissertation Committee:

Ganesh Balakrishnan , Chairperson

Jean-Claude Diels

Daniel Feezell

Timothy Newell

BEAM COMBINING OF FIBER LASERS AND VERTICAL EXTERNAL CAVITY SURFACE EMITTING LASERS USING VOLUME BRAGG GRATINGS

by

CHUNTE ANDREW LU

B.S., Electrical Engr., The University of Akron 2003
M.S., Optical Science & Engr.., The University of New Mexico, 2010

DISSERTATION

Submitted in Partial Fulfillment of the
Requirements for the Degree of

Doctor of Philosophy
Optical Science and Engineering

The University of New Mexico
Albuquerque, New Mexico

December 2014

©2014, Chunte Andrew Lu

Acknowledgements

I would like to thank Professor Ganesh Balakrishnan, for advising me throughout my dissertation and it has been a great honor to be one of his PhD students. My gratitude also extends to my committee members, Prof. Jean-Claude Diels, Prof. Daniel Feezell, Dr. Timothy Newell, and Prof. Luke Lester for their advices on my dissertation. I am also very grateful for my mentors at the Air Force Research Laboratory, Dr. Thomas Shay, Dr. William Roach, Dr. Ron Kaspi, Dr. Alan Paxton, Dr. Erik Bochove, and Dr. Gerald Moore for their constant encouragement and support. The dissertation would not have succeeded without the state-of-the-art volume Bragg gratings beam combiners and thanks to Dr. Leonid Glebov and his research group at OptiGrate Inc. for providing such critical technology. In addition, I would like to thank Dr. Alexander Albrecht and Mr. Christopher Hains from the research group for their help and support. I am also indebted to Dr. Jerome Moloney and Dr. Maik Scheller from the University of Arizona for providing several high brightness VECSELs. Finally, I would also like to give special thanks to my colleagues at the Air Force Research Laboratory, Dr. Angel Flores, Dr. Iyad Dajani, Dr. Craig Robin, Dr. Clint Zeringue, and all who have helped me throughout my research.

Dedication

I dedicate this dissertation to my parents, my wife Akiko, and my daughter Hana.

BEAM COMBINING OF FIBER LASERS AND VERTICAL EXTERNAL CAVITY SURFACE EMITTING LASERS USING VOLUME BRAGG GRATINGS

by Chunte Andrew Lu

Abstract

Advances in high brightness laser sources with near diffraction limited beam quality outputs have enabled wide range of applications. However, physical constraints such as material heating and nonlinear effects limit the maximum achievable power of these laser sources. In order to obtain higher power level, beam combining techniques such as coherent beam combining and spectral beam combining are employed to enhance the power and brightness of a single output beam. In this thesis, we investigate various beam combining approaches using a holographic gratings based beam combiner, volume Bragg gratings, for combining the high brightness lasers sources. First, we theoretically study the performance of the beam combiners using the coupled wave equations. Then we conduct beam combining experimental demonstrations of high brightness fiber lasers in both active and passive coherent beam combining schemes using the proposed combiners. Lastly, we explore beam combining methods suitable for high brightness semiconductor lasers with the volume Bragg gratings beam combiners.

Table of Contents

List of Tables

List of Figures

Chapter 1 : Introduction

High-brightness laser sources have continued to develop and evolve ever since the first laser demonstration in 1960s [1]. In terms of lasers, "brightness" is directly related to the power and beam quality of the laser and is synonymous with radiance, which is defined as the total power over the product of unit area and unit solid angle. From material processing and medical surgery to remote sensing and missile defense for military, high-brightness lasers have exhibited a wide range of applications. Current commercially available high-brightness lasers are power limited due to several physical constraints, such as material heating, optical damage, and nonlinear effects. For example, in most optically pumped lasers, the energy difference between the pump and the laser photons causes quantum defect heating in the gain media [2]. Nonlinear effects in the fiber lasers such as stimulated Brillouin scattering [3] [4] [5] [6], stimulated Raman scattering [3] [5] [6], and four-waves mixing [7] also set fundamental limitations to prevent further power scaling. Therefore, in order to further enhance the power and brightness of existing laser systems, one of the recommended methods is to introduce beam combining techniques to spatially overlap multiple laser outputs.

Generally speaking, there are two types of beam combining techniques: coherent beam combining and incoherent beam combining. Coherent beam combining requires mutual coherence between the lasers and it is often categorized into active phasing and passive phasing techniques depending on the scheme used for phase control. While scalability of passive phasing technique appears limited due to brightness gain saturation when array size is greater than ten [8], active coherent beam combining has shown

efficient beam combining with 64 fiber laser arrays [9] and even larger number of channels in diode laser arrays [10]. On the other hand, incoherent beam combining does not rely on mutual coherence and phase locking to achieve beam combining effect. One of the frequently used incoherent beam combining techniques, spectral beam combining, utilizes wavelength-sensitive optical element to spatially overlap lasers with dissimilar emission spectra [11] [12]. Far-field overlapping is also an incoherent beam combining technique and it involves directing the laser array in the same direction [13]; however the technique only increases output power without enhancing its brightness.

The focus of this dissertation is to introduce volume Bragg gratings (VBGs) as beam combiners to explore various beam combining schemes for high-brightness laser sources. VBGs are thick holographic gratings inscribed in a photosensitivity glass typically using the interference pattern generated by an ultraviolet (UV) laser source. All the VBGs and multiplexed VBGs (MVBGs) described in this thesis are provided by OptiGrate Inc. and recorded in photo-thermal-refractive (PTR) glass [14]. The chemical formula for the PTR glass is Na_2O-ZnO-Al_2O_3-SiO_3 with silver, cerium, and fluorine as dopants. After UV exposure and thermal annealing process, the refractive index change in the PTR glass becomes permanent which makes the specialty glass an excellent candidate for recording holographic gratings. Recent advances have shown greater than 95% diffraction efficiency for the VBGs recorded in the PTR glass [15]. Furthermore, because the PTR glass exhibits high laser damage threshold and wide transparency window [16], it is suitable for high-brightness laser applications as well.

Chapter 2 describes various type of beam combining techniques in detail, including incoherent beam combining techniques: spectral beam combining and far-field

overlapping, and coherent beam combining techniques: active coherent beam combining and passive coherent beam combining. Chapter 3 presents the theory of VBGs and the theoretical modeling and simulation of the transmissive and reflective MVBGs. Beam combining experimental demonstration starts in Chapter 4 using fiber lasers [17] [18] and Chapter 5 using vertical cavity external cavity surface emitting lasers (VECSELs) [19]. Both fiber lasers and VECSELs are optically pumped lasers capable of producing high-brightness output with excellent beam quality. And finally, Chapter 6 concludes this dissertation with the path forward to obtain higher brightness laser sources based on the VBGs beam combining study.

Chapter 2 : Overview of Beam Combining Techniques

As mentioned in the previous chapter, laser beam combining techniques can be divided into two classes: incoherent beam combining and coherent beam combining. While incoherent beam combining offers simplicity and flexibility in system configuration and implementation, coherently beam combined outputs produce the highest quality in both brightness and spectral radiance. This chapter provides the background of commonly used beam combining techniques and their current state of capabilities.

2.1 Incoherent Beam Combining

Incoherent beam combining is particularly useful when combining laser sources with different laser characteristics. Generally, incoherent beam combining techniques are divided into spectral beam combining and far-field overlapping. While spectral beam combining utilizes optics to obtain co-linearly combined output, far-field overlapping relies on beam steering and far-field diffraction to merge the laser outputs into one spot. In the laser community, far-field overlapping is often not described as a beam combining technique because the combined output brightness is not greater than the brightness of a single laser element. However, for military applications, far-field overlapping is frequently adopted to increase the power on a target over long distance.

2.1.1 Spectral Beam Combining

The concept of spectral beam combining, also known as wavelength beam combining, is to spatially overlap multiple dissimilar wavelength lasers with color sensitive optical elements, such as prisms, diffractive gratings, dichroic mirrors, and volume Bragg gratings (VBGs). Prisms and diffractive gratings can alter lasers propagation direction so the incoming lasers with different wavelengths become co-linear to each other as shown

in Fig 2.1, where $\lambda_1 > \lambda_2$ in both cases. Due to the dispersive nature of the optics, the beam quality on the dispersive axis usually degrades when using broad spectral linewidth lasers. For combing lasers with broader spectral linewidth, an alternative approach of spectral beam combining using two gratings in a grating rhomb configuration has shown excellent combined output beam quality using multiple high power fiber lasers [20]. In terms of the highest total combined power, greater than 8kW of combined output has been reported using four fiber laser amplifiers with a polarization-independent dielectric reflective diffraction grating [21]. A more sophisticated beam combining design involving diffractive gratings in a cavity has also yield successful beam combining of 1400 single diode emitters [22].

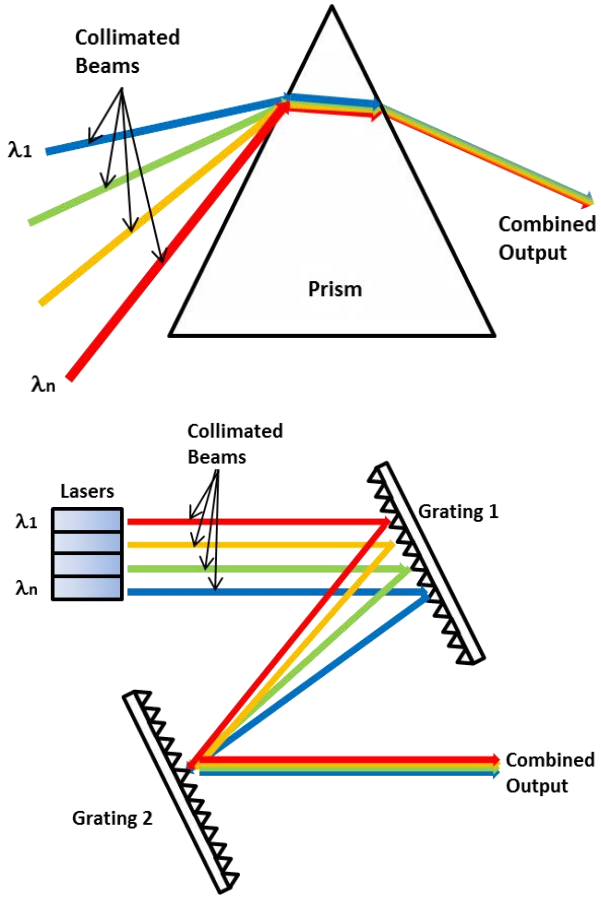

Fig 2.1 Spectral beam combining using a prism and diffractive gratings

Dichroic mirrors and VBGs are optics with specific transmission and reflection windows and multiplexing is usually required in order to combine multiple laser sources as shown in Fig 2.2. Dichroic mirrors have broad transmission and reflection windows ranging from 30 nm to 0.5 μm and VBGs are generally used for narrow linewidth applications and have narrow bandwidth typically around 0.5 nm. Dichroic mirrors are dielectric mirrors based on thin-film interference principal and the primarily usage is to overlap multiple lasers with significantly different optical spectrum. Several applications such as laser alignment, multispectral imaging, and laser damage threshold testing, use dichroic mirrors to produce a single laser output with both infrared and visible spectrum [23]. On the other hand, VBGs are thick holographic gratings functioning according to the Bragg's law. Because the low contrast in refractive index modulation leads to extended diffraction length, VBGs have much narrower bandwidth compare to the dichroic mirrors and are often incorporated in laser cavities to spectrally narrow the output of the lasers [24]. Recently, VBGs and multiplexed VBGs (MVBGs) have shown excellent results for spectral beam combining of high power fiber lasers [25] [26]. MVBGs are photosensitive glass recorded with multiple sets of holographic gratings on top of each other. Since the VBGs and MVBGs are the essential beam combining elements used in this thesis, the detailed theory and operation principal of the VBGs and MVBGs will be discussed in Chapter 3. Furthermore, a new method of spectral narrowing and combining multiple semiconductor lasers using MVBGs is described in Chapter 5.

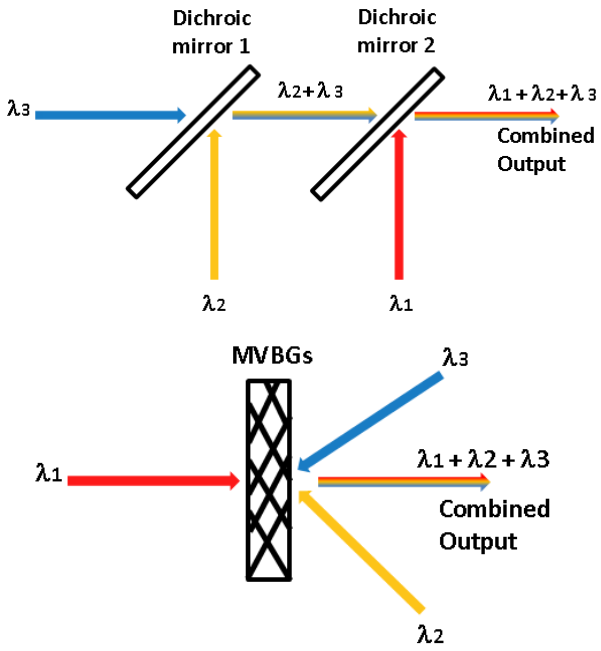

Fig 2.2 Spectral beam combining using dichroic mirrors and MVBGs

2.1.2 Far-field Overlapping

Ancient Greek scientist Archimedes constructed a directed energy weapon "heat ray" to destroy enemy ships in the sea. More recently, the US Navy conducted a laser turret test to take down an unmanned aerial vehicle in the sky. Both of these two military events utilized far-field overlapping techniques to combine multiple light sources at a destination some distance away as shown in Fig 2.3. Far-field overlapping is usually accomplished using a set of beam steering optics such as turning mirrors or beam directing telescopes. It is simplicity in design and without stringent requirements for the laser sources. Multi-kW combining power has been achieved using four high power fiber laser amplifiers with the far-field overlapping technique [13]. However there is one caveat to the far-field overlapping technique, while the total power on the far-field target is increased through overlapping the lasers, the radiance of the combined beam does not increase according to the radiance theorem [27].

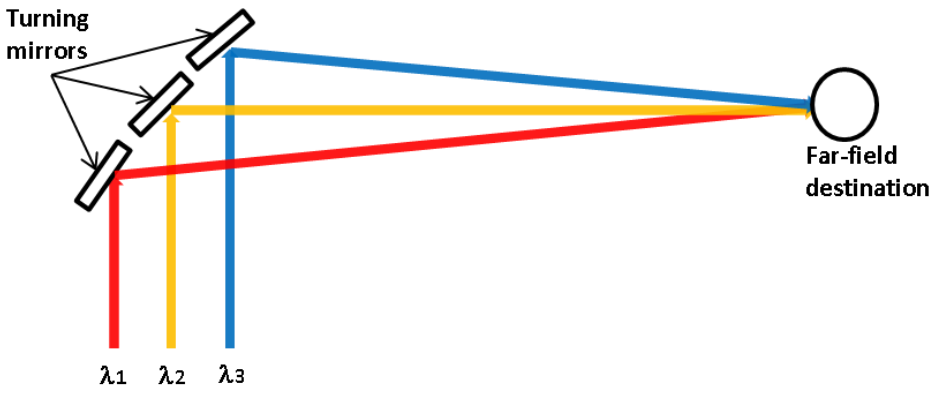

Fig 2.3 Far-field overlapping incoherent beam combining using multiple lasers

2.2 Coherent Beam Combining

Coherent beam combining (CBC) requires mutual coherence between all the combining laser sources. In other words, each individual laser needs to have the same frequency and polarization, in addition, a proper phase locking scheme to maintain the phase of the lasers is essential to achieve efficient beam combining. The CBC schemes can be divided into active CBC and passive CBC depending on the methods used for phase locking.

2.2.1 Active Coherent Beam Combining

Active CBC employs electronic feedback to control and adjust the optical phase of the individual laser sources so the combined output brightness increases. The phase adjustment is often accomplished by introducing optical delay through optics such as optical stretcher, electro-optic modulator (EOM), and acousto-optic modulator (AOM). While optical stretcher only shifts the phase of the incoming light, EOM and AOM can be used to change the phase, frequency, amplitude, or polarization property of the light. Recent high power fiber laser active CBC experiments use commercially available fiber-coupled EOMs containing Lithium niobate ($LiNbO_3$) nonlinear crystal to control both

polarization and phase of each individual laser. The choice of phase adjustor also depends on the modulation frequency requirement of the application.

There are three main classes of active phase control loops for active CBC: optical heterodyne detection (OHD), synchronous multi-dither, and hill climbing algorithm. Both OHD and synchronous multi-dither use radio frequency (RF) electronics to generate heterodyne beats (also called error signal) needed for phase adjustment. Furthermore, OHD method also requires a frequency shifted reference laser and a photo-detector for each of the combining lasers as shown in Fig 2.4. On the other hand, synchronous multi-dither methods such as Locking of Optical Coherence by Single-detector Electronic-frequency Tagging technique (LOCSET) can operate without an additional reference laser and only one detector is required for phase locking multiple lasers as shown in Fig 2.5. In a LOCSET phasing system, each laser channel is "tagged" with a slightly different RF frequency for phase dithering. When applying demodulation, the system can identify the channels based on the unique frequencies and perform phase adjustments. The LOCSET phasing system has two operational modes: self-referenced and self-synchronous phase locking modes [28] [29]. The detailed theory of LOCSET and its modes of operation are described in Appendix A.

Hill climbing algorithm offers the simplest and low cost method to actively phase lock an array of lasers. Basically, it is an algorithm to simultaneously change the phase of the entire laser array by a small amount until achieving the maximum output power. The most frequently used hill climbing algorithm is stochastic parallel gradient decent technique (SPGD) [30]. With the exception of the electronic phase control loops, the SPGD CBC setup is similar to the multi-dither technique operated under self-

synchronous mode as shown in Fig. 5. While SPGD does not require the use of RF electronics, the scalability is limited by the inverse relationship between the control loop bandwidth and the number of combining channels [31]. Nonetheless, active CBC incorporated with SPGD technique has shown high efficient beam combining result using eight high power fiber laser amplifiers at 4 kW combined output power [32].

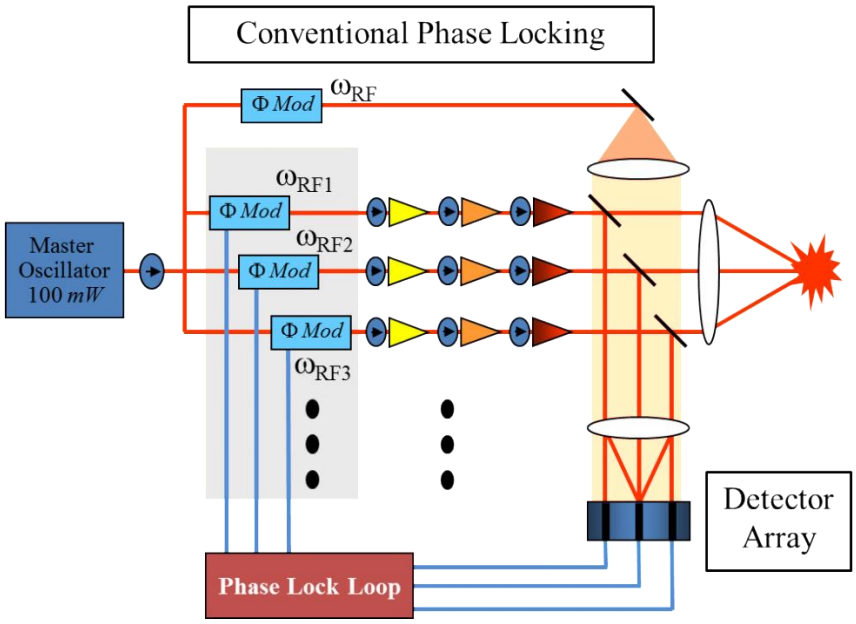

Fig 2.4 Conventional OHD method for combining an array of lasers

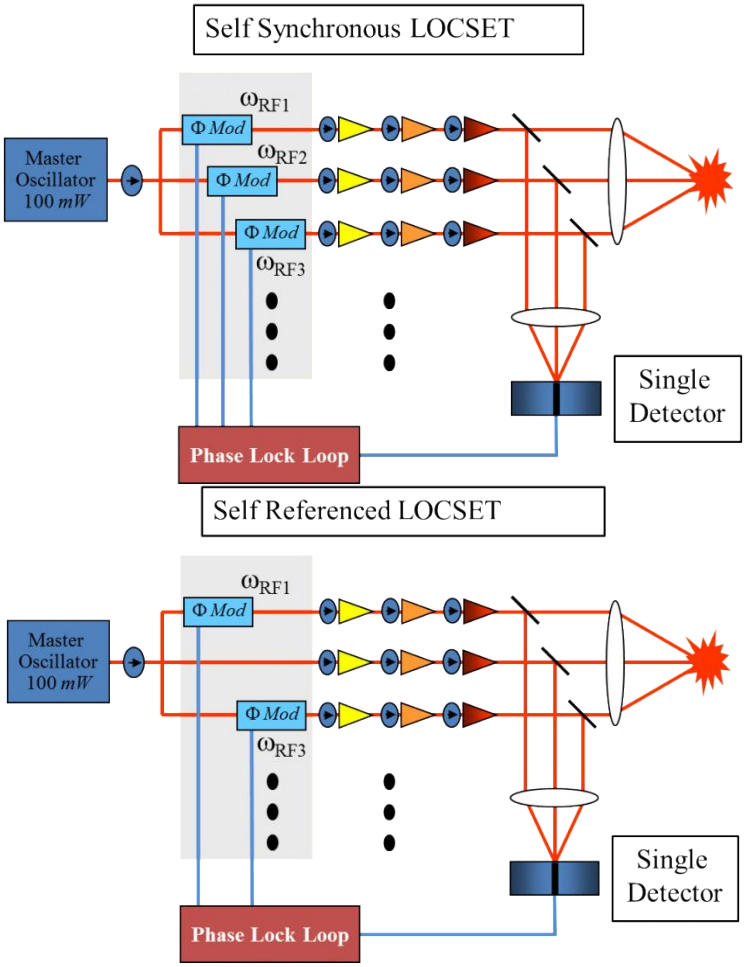

Fig 2.5 LOCSET synchronous multi-dither technique for active coherent combining operated under self-synchronous mode and self-referenced mode

Besides the ability to control and stabilize the phase of the laser array, the output beams still need to be spatially overlapped. In principal, there are two types of geometric beam combining architectures: tiled aperture beam combining and filled aperture beam combining. For tiled aperture beam combining, the lasers are arranged side by side in the near field with the outputs point in the same direction so they overlap and interfere in the far field as shown in Fig 2.4 and Fig 2.5. The advantages of the tiled aperture systems include distributed thermal load on the exit optics, N^2 irradiance scaling potential (N is the number of the channels) [33], fine electronic beam steering [34], and atmospheric turbulence compensation [35]. However, the non-uniform fill factors limit the maximum

combining power in the far-field central lobe in the tiled aperture systems. The fill factor is determined by both the near-field beam profile of the individual laser and the arrangement of the entire array. For beam combining lasers with Gaussian beam profiles in a close-packed hexagon arrangement, the maximum obtainable power in the far-field central lobe is approximately 75% of the total combining power [33]. Nonetheless, progress in high power fiber laser tiled aperture CBC has reached kW combined output using SPGD [32] and LOCSET [36].

On the other hand, filled aperture beam combining does not suffer from the fill factor limitation due to the lasers are superimposed in the near field as shown in Fig 2.6. This is often accomplished by using optical beam splitting elements in reverse. For active CBC with non-polarizing beam splitting optics, the power of the bright output port increases through constructive interference when the lasers are under proper phase relationship. Examples of the non-polarizing splitting optics include beam splitting cubes/mirrors, fiber couplers, diffractive optical elements (DOE) [37], and multiplexed volume Bragg gratings (MVBGs). Beam splitting cubes/mirrors and fiber couplers usually have dual input/output ports and require cascading to combine more laser elements. DOE and MVBGs are multiport beam splitters/combiners that are capable of combining larger array of lasers. Previously, both one-dimensional and two-dimensional DOE active CBC schemes have been demonstrated using high power fiber laser amplifiers [38] [39]. In this thesis, we have successfully demonstrated MVBGs active CBC using five high power fiber laser amplifiers and LOCSET phase locking scheme [17] [18]. The details of the combining scheme and results will be discussed in Chapter 4.

In the case of active CBC using polarizing beam splitting optics, the two orthogonal linearly polarized beams are phase adjusted to form a single linearly polarized output after the first polarizer. Then the polarization of the combined output is rotated via a half-wave plate before combining with the third laser element using the second polarizer. To combine more elements, more wave plate and polarizer pair is added to the beam combining system [40]. An alternative approach for combining 32 laser elements with five pairs of polarizers and high reflective mirrors has been proposed [41].

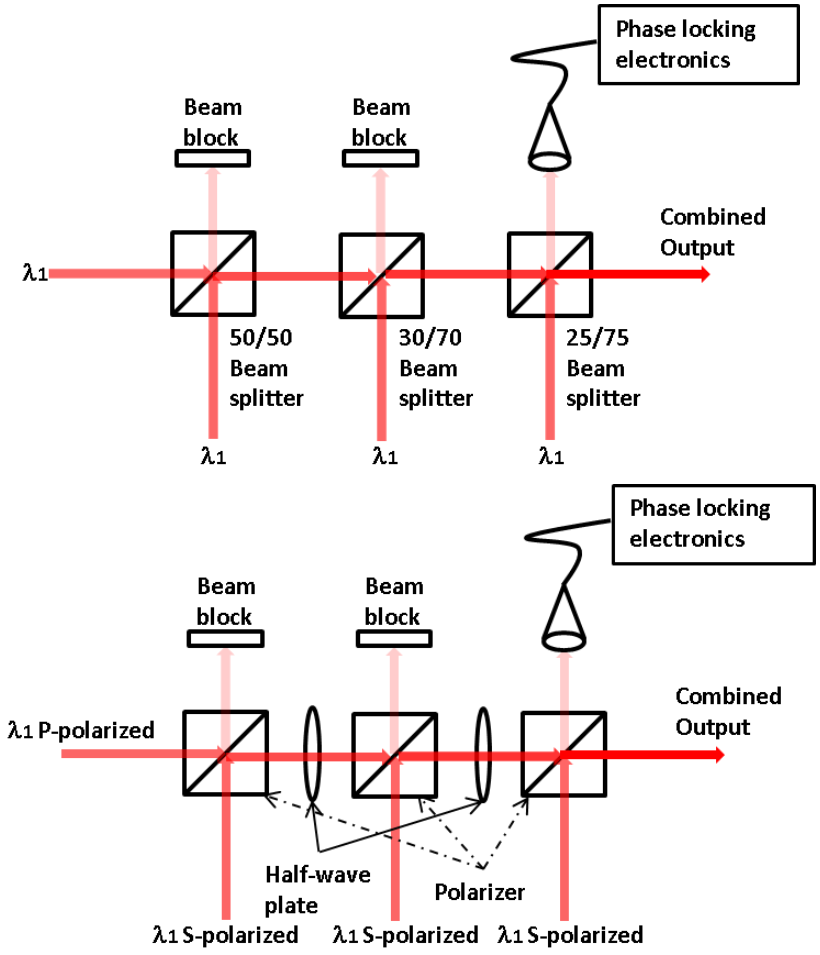

Fig 2.6 Examples of active filled aperture CBC schemes with non-polarizing beam splitting optics and polarizing beam splitting optics

2.2.2 Passive Coherent Beam Combining

Passive CBC techniques achieve mutual coherence between the laser arrays without the necessity of active feedback loops and the electronic phase controllers. This self-phasing mechanism is usually accomplished by forming a common cavity between all the laser elements. Similar to active CBC, passive CBC techniques are also categorized into tiled aperture and filled aperture arrangements. The commonly used tiled aperture schemes include Talbot cavity, self-Fourier cavity, and spatial filtering cavity.

Talbot cavity exercises the self-replicating property of the Talbot effect to obtain coupling between the neighboring laser elements. Talbot effect is a Fresnel diffraction phenomena first observed in 1836 [42]. Basically, the effect periodically reproduces the image of the laser fields after a Talbot distance. For a one-dimensional Talbot array as shown in Fig 2.7, the Talbot distance is calculated as $Z_T = \frac{2d^2}{\lambda}$, where d is the distance between the laser elements and λ is the operating wavelength in free space. To form the Talbot cavity for combining multiple lasers, the output coupling mirror is placed at the $\frac{Z_T}{2}$ distance from the laser arrays to take account for the round trip propagation distance. This approach has been demonstrated using one-dimensional diode laser arrays [43] and two-dimensional multi-core fiber structure [44].

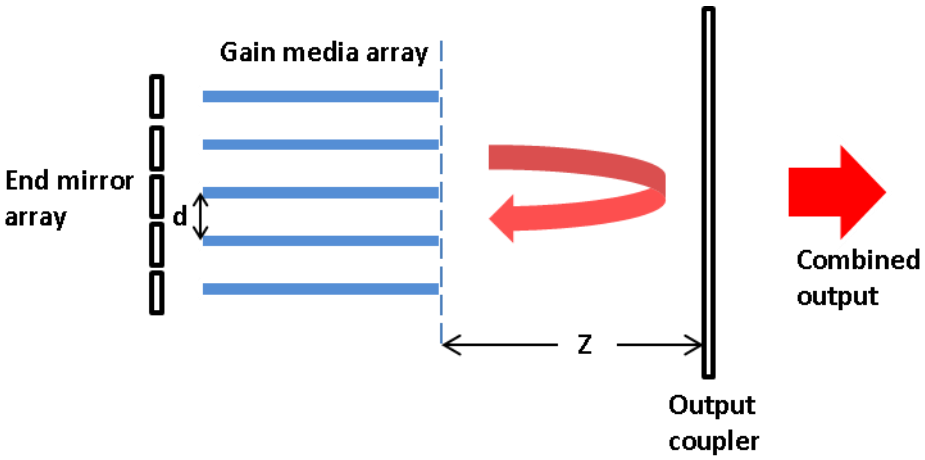

Fig 2.7 Passive coherent beam combining schemes tiled aperture Talbot cavity

Self-Fourier cavity is another approach that reimages the laser fields to stabilize the phases of a laser array. It utilizes the self-Fourier functions such as the Dirac comb function and the Gaussian function to arrange the laser elements so the laser field amplitude distribution is the same as its own spatial Fourier transform as shown in Fig 2.8. Unlike the adjacent couplings in the Talbot cavity, all the laser elements couple strongly toward the central region of the laser array in the self-Fourier cavity. This is because the self-Fourier function of an array of Gaussian laser fields has a Gaussian envelop when the array is sufficiently large. This method has been experimentally demonstrated using seven fiber lasers with a total combined output of 0.4 W [45].

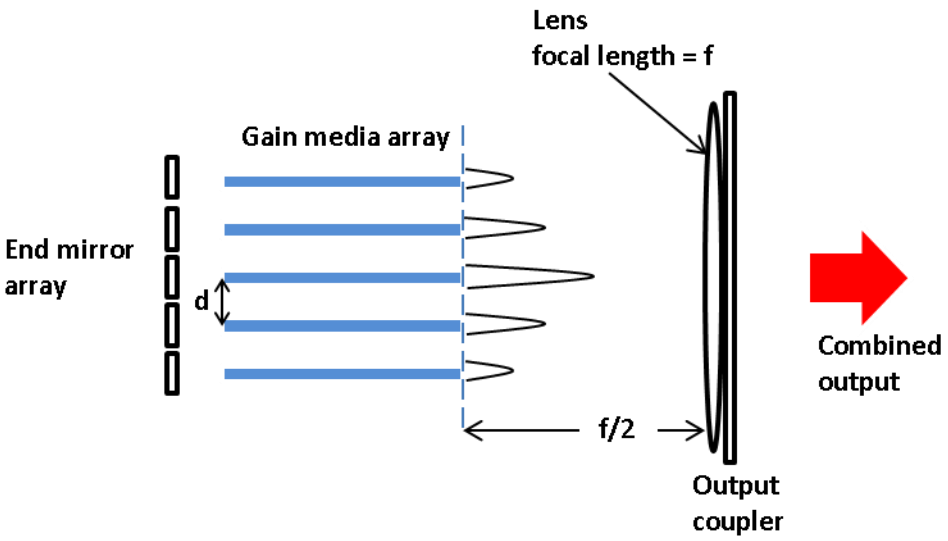

Fig 2.8 Passive coherent beam combining schemes tiled aperture self-Fourier cavity

Spatial filtering passive CBC technique applies the concept of Fourier optics to mitigate the higher order modes in the laser cavity. The spatial filtering is often achieved by inserting a spatial filter such as pinhole or grating at the focal plane of a Fourier transform lens in the beam combining cavity as shown in Fig 2.9. At the focal plane of the lens, the electric field distribution of the collimated laser array is transformed into the spatial frequency domain. The spot near the center of the domain corresponds to the fundamental mode of the cavity. When all the lasers have the identical phase, the combined wavefront appears to come from a larger single aperture and a smaller spot can be observed at the focal plane. Therefore, by placing a small aperture at the focal plane of the lens can achieve phase locking between the laser elements. The spatial filtering method has been demonstrated at high power using four fiber lasers in a two-dimensional ring cavity arrangement to produce combined output of 0.7 kW [46].

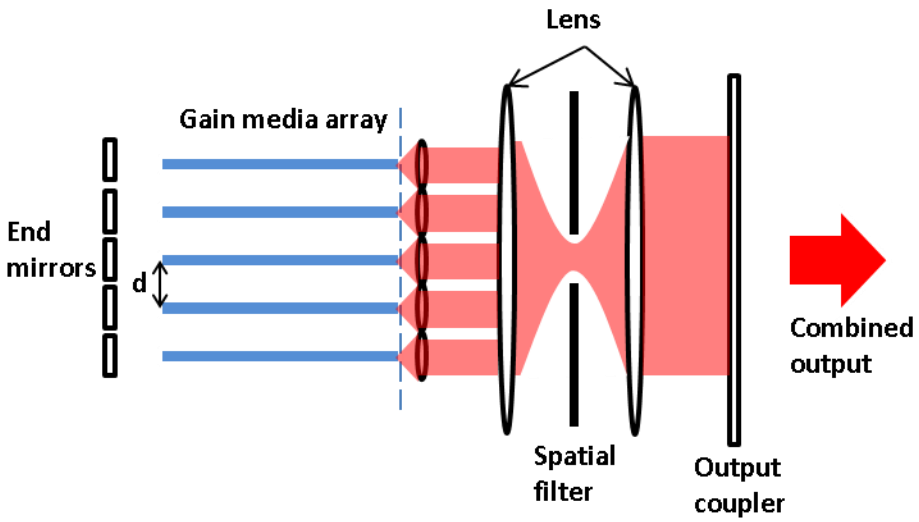

Fig 2.9 Passive coherent beam combining schemes tiled aperture spatial filtering cavity

Similar to the filled aperture active CBC, the filled aperture passive CBC also depends on the beam splitting/combining optics to spatially overlap multiple lasers in the near field. Examples of the filled aperture passive CBC schemes include beam splitter array cavity and multiport beam splitter cavity as shown in Fig 2.10 and Fig 2.11, respectively. Beam splitter array cavity is often implemented using splitting cubes/mirrors or fiber couplers. As previously mentioned, these combiners only have two input/output ports and an array of combiners is required to combine numerous laser elements. In contrast, diffractive optical elements (DOE) and multiplexed volume Bragg gratings (MVBGs) are multiport beam splitters that utilize diffraction to split an input beam into multiple beams at different output angles. The phase stabilization between the laser elements is achieved by providing sufficient feedback from the combined port for all above filled aperture passive CBC schemes. Efficient beam combining results have been shown in beam splitter array cavities using fiber couplers [47] [48] and in multiport beam splitter cavity architectures using DOE [49] and MVBGs [50].

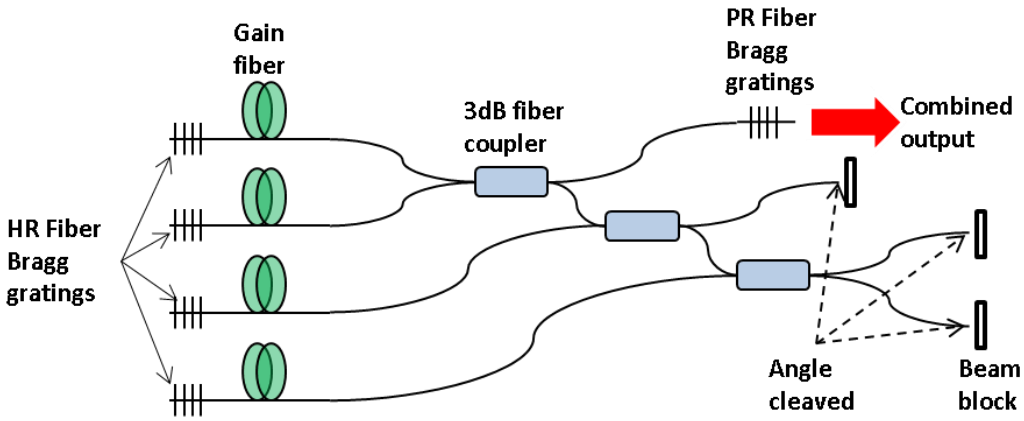

Fig 2.10 Passive coherent beam combining schemes filled aperture beam splitter array cavity

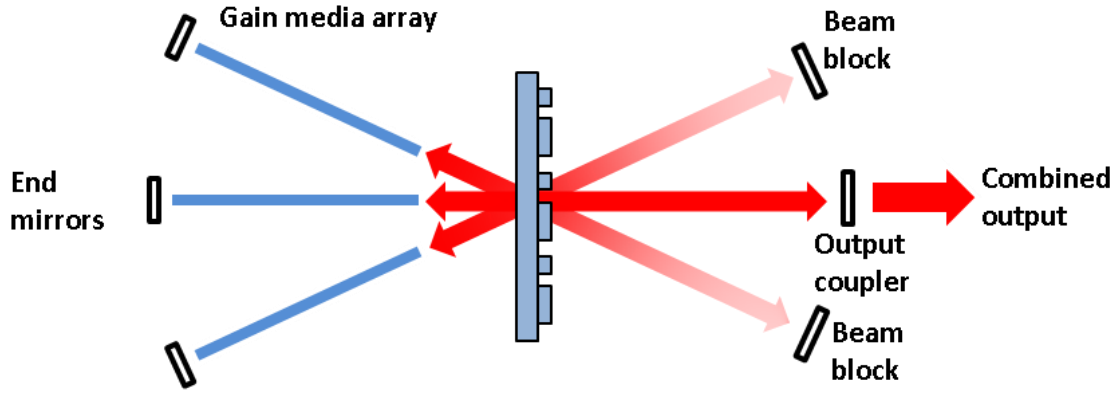

Fig 2.11 Passive coherent beam combining schemes filled aperture multiport beam splitter cavity

2.3 Summary

Overall, the choice of beam combining method not only depends on the type of the laser sources but also the requirement of the applications. While incoherent beam combining techniques offer system simplicity, the output of the coherently combined system can deliver high spectral brightness. A brief summary of the various beam combining techniques are shown in Table 2.1. The combined power column shows the highest reported combining power using fiber lasers; however the beam combining techniques

are not limited to only fiber lasers. Furthermore, the combined power loss due to individual laser failure is higher for coherent beam combing than for incoherent beam combining as illustrated in Fig 2.12. The effect of power loss should also be taken into consideration when designing beam combining system for specific power level requirement.

Table 2.1 Summary of beam combining techniques

Beam Combining Techniques	Advantages	Disadvantages	Combined Power Reported Using Fiber Lasers
Active Coherent Beam Combining (tiled aperture)	• Atmospheric compensation possible • Fine electronic beam steering • Potential N^2 irradiance scaling • Capable of combing large laser array	• Complex active phase control required • High loss in the case of laser source failure (filled aperture) • Sensitive to surrounding environment – added phase noise may decrease combining efficiency	• 1.4 kW with 16 elements, single frequency (AFRL)[36] • 4 kW with eight elements, 10 GHz (MIT-LL)[32]
Active Coherent Beam Combining (filled aperture)	• Excellent beam quality • Capable of combining large laser array		• 2 kW with five elements, 10 GHz linewidth (MIT-LL)[38]
Passive Coherent Beam Combining (tiled aperture)	• No active phase control required • Excellent beam quality (filled aperture arrangement)	• Intracavity power built up prevents high power operation • Limited channel scalability	• 50 W with two elements using fiber couplers (Vytran)[48]
Passive Coherent Beam Combining (filled aperture)			• 0.7 kW with four elements (Lockheed-Aculight)[46]
Spectral Beam Combining (incoherent beam combining)	• No active phase control required • Excellent beam quality	• Channel scalability influenced by laser gain bandwidth	• 8 kW with four elements (Friedrich-Schiller University)[21]

Far-field Overlapping (incoherent beam combining)	• Simplicity in design • No active phase control required • No stringent requirements on laser specifications • No physical limit to prevent channel scaling	• Steering optics required for each laser source • Brightness of the combined output is not greater than the individual laser element	• 3 kW with four elements at ~1 km propagation distance (NRL)[13]

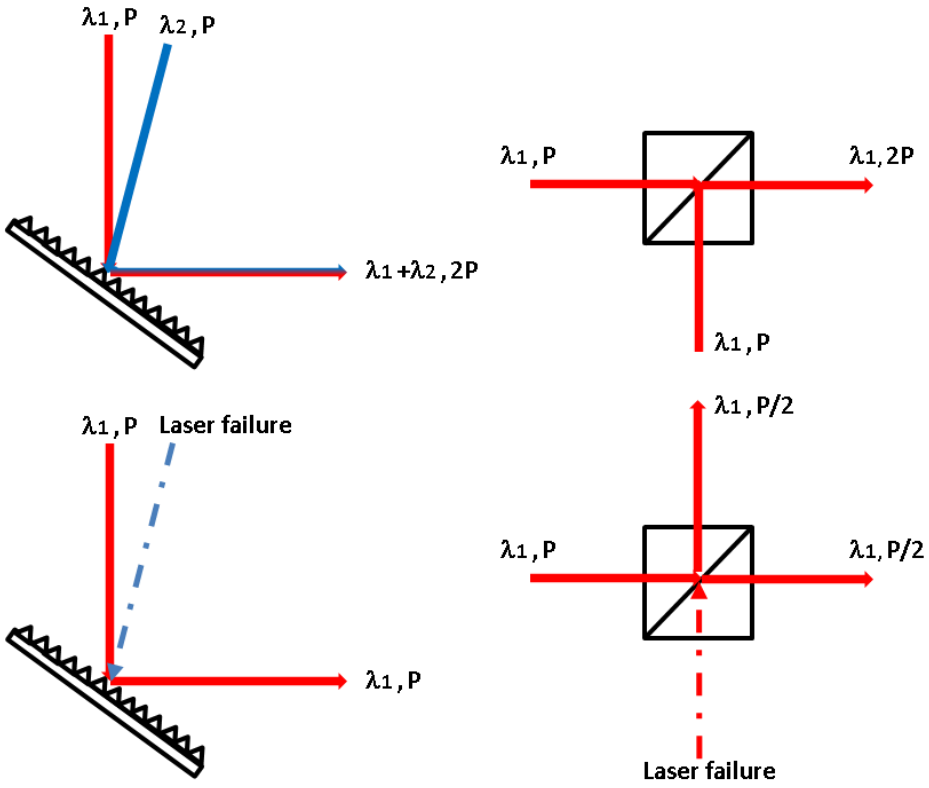

Fig 2.12 The effect of power loss due to single laser failure in the two channels beam combining systems: incoherent beam combining versus coherent beam combining

Chapter 3 : Theoretical Modeling and Analysis of Beam Combining Effect Using Volume Bragg Gratings

In this chapter, we will first describe the fundamental theory of the volume Bragg gratings (VBGs), the beam combiner used throughout this dissertation. The discussion is followed by the theoretical modeling and simulation of the transmissive and reflective multiplexed volume Bragg gratings (T-MVBGs and R-MVBGs) using coupled wave theory. Finally, we will conclude this chapter with a summary.

3.1 Theory of Volume Bragg Gratings

As mentioned earlier, the volume Bragg gratings used in this thesis are written in photo-thermo-refractive (PTR) glass [14] using interferometry of ultraviolet (UV) light source. The PTR glass is a photosensitive silicate glass (Na_2O-ZnO-Al_2O_3-SiO_3) doped with silver, cerium, and fluorine and permanent change of refractive index as high as 10^{-3} (1000 ppm) can be achieved after exposure to UV radiation followed by thermal annealing process. While being photosensitive in the UV, PTR glass offers high transmittance in the near-infrared and visible parts of spectrum (350-2700 nm) with absorption in the near-infrared region ~10^{-4} cm^{-1}. Here are some of the PTR glass material properties:

Thermal expansion coefficient: 8.5×10^{-6} K^{-1};

Thermal conductivity: 0.01 $Wcm^{-1}K^{-1}$;

Change of refractive index with respect to temperature: $dn/dT = 5x10^{-7}$ K^{-1};

Laser damage threshold: 10 J/cm^2 for 10 ns pulses, and ~10 kW/cm^2 for CW laser in the near-infrared;

Thermal stability of holograms: up to 400 °C.

In addition to the excellent optical and thermal-mechanical properties of the PTR glass, the ability to control refractive index change in PTR glass and fabricate high efficiency VBGs makes the VBGs inscribed in PTR glass a practical technology for high power laser beam combining.

The concept of Bragg diffraction was first proposed by William L. Bragg and William H. Bragg in 1913 [51] while discovering the crystalline solids produced intense peaks of reflected X-rays at specific wavelengths and incident angles. Basically, this phenomenon occurs when electromagnetic wave such as laser light incidents on a periodic structure with the spacing in the order of the laser wavelength. The scattered light experiences constructive interference at the angle where the phase shift is a multiple of 2π. This Bragg law is expressed as:

$$m\lambda = 2d \sin\theta \qquad (3\text{-}1)$$

where m is diffraction order, λ is the wavelength of the incident light, d is the spacing of the periodic structure, and θ, also known as the Bragg angle, is the angle between the incident light and the plane of the periodic structure. For thick holographic gratings such as the VBGs, the diffraction happens inside the medium and only at a certain angle (i.e. $m = 1$). Thus the Bragg condition for the VBGs is given by:

$$\lambda_0 = 2dn\,|\cos\theta_m| \qquad (3\text{-}2)$$

here n is the refractive index of the PTR glass, λ_0 is the wavelength of the incident light in vacuum, and θ_m is the incident angle in the medium. Furthermore, the derivative of the Bragg condition shown as (3-3) provides the relation between the angular sensitivity and the wavelength sensitivity of the VBGs. This relationship indicates the acceptance angle

is wider for the incident laser with broader linewidth; however it does not address the characteristics of the diffracted light.

$$d\theta_m = \frac{d\lambda_0}{2dn\sin\theta_m} \qquad (3\text{-}3)$$

Various mathematical methods have been investigated in the past to predict the diffraction characteristics of the thick holographic gratings. Among all, the coupled wave theory developed by Kogelnik in 1969 [52] is the most adopted for analyzing such diffractive device. The derivation of the coupled wave theory begins from the scalar form of the wave equation and assumes the monochromatic light incident on the holographic gratings at or near the Bragg angle. The scalar form of the wave equation is obtained from the time harmonic Maxwell's equations in differential forms assuming no presence of charges and currents:

$$\nabla \cdot E = 0 \qquad (3\text{-}4)$$

$$\nabla \cdot B = 0 \qquad (3\text{-}5)$$

$$\nabla \text{ x } E = i\omega B \qquad (3\text{-}6)$$

$$\nabla \text{ x } B = -i\omega\mu\varepsilon E \qquad (3\text{-}7)$$

where E is the electric field, B is the magnet field, ω is the angular frequency of the incident light, and ε and μ are the permittivity and permeability of the medium, respectively. By taking the curl (∇ x) of (3-6) and using the vector identity $\nabla \text{ x } (\nabla \text{ x A}) = \nabla(\nabla \cdot \text{A}) - \nabla^2\text{A}$, we arrive at the scalar wave equation:

$$\nabla^2 E + \omega^2\mu\varepsilon E = 0 \qquad (3\text{-}8)$$

Now we consider a sinusoidal index grating (i.e. VBGs) in an isotropic medium as shown in Fig 3.1. The refractive index and dielectric constant modulation as a function of space are given by:

$$n(z) = n_0 + n_1 \cos Kz \qquad (3\text{-}9)$$

$$\Delta\varepsilon(z) = 2\varepsilon_0 n_0 n_1 \cos Kz \qquad (3\text{-}10)$$

where K is the grating vector ($|K| = \frac{2\pi}{\Lambda}$, Λ is the grating spacing), n_0 is the average refractive index of the medium, and n_1 is the depth of index modulation.

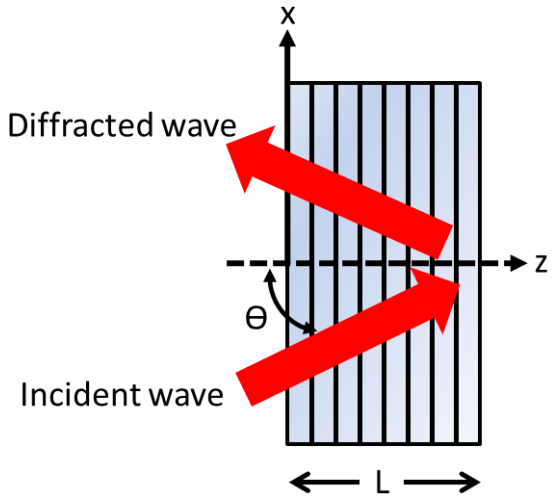

Fig 3.1 Schematic of light interaction inside the VBGs. θ is angle between the incident light and z-axis

After taking the refractive index modulation into account, the revised wave equation is now:

$$(\nabla^2 + \omega^2\mu\varepsilon + \omega^2\mu\Delta\varepsilon)E=0 \qquad (3\text{-}11)$$

Next, we write the electric fields of the incident light and the diffracted light as:

$$E(x,y,z,t) = A_1(z)E_1(x,y)e^{i(\omega t-\beta_1 z)} + A_2(z)E_2(x,y)e^{i(\omega t-\beta_2 z)} \qquad (3\text{-}12)$$

where $A_1(z)$ and $A_2(z)$ are the field amplitude of the incident and diffracted light, respectively; β_1 and β_2 are the propagation constants for the incident and diffracted light in the z direction. The wavefunctions $E_1(x,y)$ and $E_2(x,y)$ satisfy the normal mode wave equations:

$$\left[\frac{\partial^2}{\partial x^2}+\frac{\partial^2}{\partial y^2}+\omega^2\mu\varepsilon_0-{\beta_m}^2\right]E_m=0, \qquad \text{m=1, 2} \qquad (3\text{-}13)$$

Substitution of (3-12) for E in (3-11) and using (3-13) leads to:

$$\sum_{n=1,2}\left(\frac{\partial^2 A_n(z)}{\partial z^2}-2i\beta_n\frac{\partial A_n(z)}{\partial z}\right)E_n(x,y)e^{i(\omega t-\beta_n z)}=$$

$$-\omega^2\mu\sum_{p=1,2}\Delta\varepsilon(z)\,A_p(z)E_p(x,y)e^{i(\omega t-\beta_p z)} \qquad (3\text{-}14)$$

Since the index modulation n_1 is very small (i.e. $n_1 \ll n_0$), the second-order derivatives are neglected in the slowly varying envelope approximation (SVEA). For the VBGs in study, the nominal ratio of n_1 and n_0 is approximately 10^{-4} [16]. After applying SVEA, (3-14) now becomes:

$$\sum_{n=1,2}\left(-2i\beta_n\frac{\partial A_n(z)}{\partial z}\right)E_n(x,y)e^{(-i\beta_n z)}=$$

$$-\omega^2\mu\sum_{p=1,2}\Delta\varepsilon\,(z)A_p(z)E_p(x,y)e^{(-i\beta_p z)} \quad (3\text{-}15)$$

By taking the scalar product of (3-15) with ${E_{k=1,2}}^*(x,y)$ and integrate over x and y, we obtain the following:

$$\int {E_k}^*\cdot E_k dxdy\frac{\partial A_k(z)}{\partial z}=$$

$$\frac{\omega^2\mu}{2i\beta_k}\sum_{p=1,2}\int {E_k}^*\cdot\Delta\varepsilon(z)\,E_p dxdy\,A_p(z)e^{i(\beta_k-\beta_p)z} \quad (3\text{-}16)$$

where the integral on the left hand side is further reduced using the orthogonality relation:

$$\int {E_k}^*\cdot E_k dxdy=\frac{2\omega\mu}{|\beta_k|} \qquad (3\text{-}17)$$

Using (3-10) for substitution of $\Delta\varepsilon(z)$ and (3-17), the final forms of the coupled equations are now:

$$\frac{\partial A_1(z)}{\partial z}=-i\frac{\beta_1}{|\beta_1|}\kappa_{12}A_2(z)e^{i(\Delta\beta z)} \qquad (3\text{-}18)$$

$$\frac{\partial A_2(z)}{\partial z}=-i\frac{\beta_2}{|\beta_2|}{\kappa_{12}}^*A_1(z)e^{-i(\Delta\beta z)} \qquad (3\text{-}19)$$

here $\Delta\beta = \beta_1 - \beta_2 - \frac{2\pi}{\Lambda}$, and κ_{12} is the coupling coefficient defined as:

$$\kappa_{12} = \frac{\omega}{4} \int {E_1}^*(x,y) \cdot \Delta\varepsilon(z)\, E_2(x,y) dxdy =$$

$$\begin{cases} \frac{\omega^2 \mu \varepsilon_0 n_0 n_1}{2\sqrt{|\beta_1 \beta_2|}}, & \text{for TE incident light} \\ \frac{\omega^2 \mu \varepsilon_0 n_0 n_1}{2\sqrt{|\beta_1 \beta_2|}} \cos 2\theta, & \text{for TM incident light} \end{cases} \qquad (3\text{-}20)$$

The types of VBGs are divided into transmissive and reflective VBGs depending on the gratings geometry as shown in Fig 3.2.

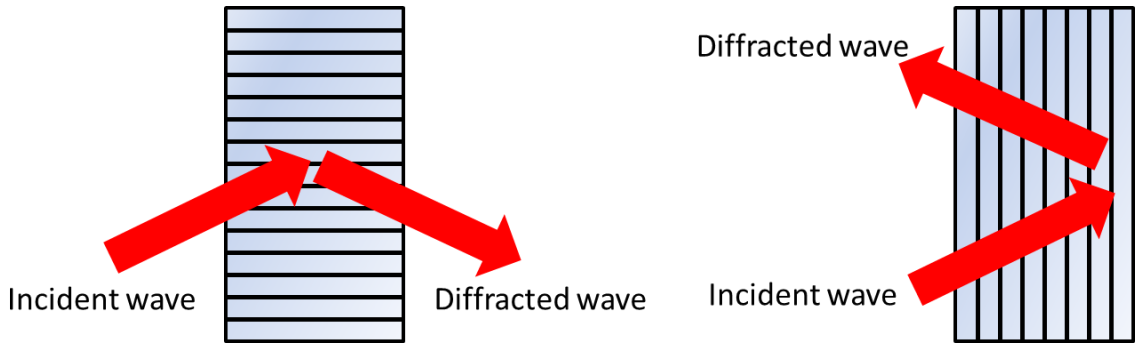

Fig 3.2 Two types of VBGs geometry: transmissive VBGs (left) and reflective VBGs (right)

For the transmissive VBGs, the incident and diffracted light are co-propagating (i.e. $\beta_1\beta_2 > 0$) and (3-18) and (3-19) become:

$$\frac{\partial A_1(z)}{\partial z} = -i\kappa_{12} A_2(z) e^{i(\Delta\beta z)} \qquad (3\text{-}21)$$

$$\frac{\partial A_2(z)}{\partial z} = -i{\kappa_{12}}^* A_1(z) e^{-i(\Delta\beta z)} \qquad (3\text{-}22)$$

We first consider the case of the perfect phase matching condition. The perfect phase matching condition occurs when $\Delta\beta = \beta_1 - \beta_2 - \frac{2\pi}{\Lambda} = 0$. Under this condition, the coupled equations have simpler forms:

$$\frac{dA_1(z)}{dz} = -i\kappa_{12} A_2(z) \qquad (3\text{-}23)$$

$$\frac{dA_2(z)}{dz} = -i{\kappa_{12}}^* A_1(z) \qquad (3\text{-}24)$$

Solutions to the above equations assuming a single incident wave are:

$$A_1(z) = A_1(0)\cos(|\kappa_{12}|z) \qquad (3\text{-}25)$$

$$A_2(z) = -i\frac{\kappa_{12}{}^*}{|\kappa_{12}|}A_1(0)\sin(|\kappa_{12}|z) \qquad (3\text{-}26)$$

where $A_1(0)$ is the field amplitude of the incident light at z = 0. The coupling efficiency is then defined as:

$$\eta = \left|\frac{A_2(L)}{A_1(0)}\right|^2 = \sin^2(|\kappa_{12}|L) \qquad (3\text{-}27)$$

For the case when $\Delta\beta \neq 0$, the solutions to (3-24) and (3-25) become:

$$A_1(z) = e^{i\left(\frac{\Delta\beta}{2}\right)z}\left(\cos sz - \frac{i\Delta\beta}{2}\frac{\sin sz}{s}\right)A_1(0) \qquad (3\text{-}28)$$

$$A_2(z) = e^{-i\left(\frac{\Delta\beta}{2}\right)z}\left(-i\kappa_{12}{}^*\frac{\sin sz}{s}\right)A_1(0) \qquad (3\text{-}29)$$

where $A_1(0)$ is the amplitude of the incident light at z = 0, and

$$s^2 = \kappa_{12}{}^*\kappa_{12} + \left(\frac{\Delta\beta}{2}\right)^2 \qquad (3\text{-}30)$$

The coupling efficiency is then:

$$\eta = \left|\frac{A_2(L)}{A_1(0)}\right|^2 = |\kappa_{12}|^2\frac{\sin^2 sL}{s^2} \qquad (3\text{-}31)$$

For the reflective VBGs, the incident and diffracted light are counter-propagating (i.e. $\beta_1\beta_2 < 0$) and the set of the coupled equations and coupling coefficient become:

$$\frac{\partial A_1(z)}{\partial z} = -i\kappa_{12}A_2(z)e^{i(\Delta\beta z)} \qquad (3\text{-}32)$$

$$\frac{\partial A_2(z)}{\partial z} = i\kappa_{12}{}^*A_1(z)e^{-i(\Delta\beta z)} \qquad (3\text{-}33)$$

Under perfect phase matching condition ($\Delta\beta = 0$), the solutions of the coupled equations are:

$$A_1(z) = \frac{\cosh|\kappa_{12}|(L-z)}{\cosh|\kappa_{12}|L}A_1(0) \qquad (3\text{-}34)$$

$$A_2(z) = -i\frac{\kappa_{12}^*}{|\kappa_{12}|}\frac{\sinh|\kappa_{12}|(L-z)}{\cosh|\kappa_{12}|L}A_1(0) \quad (3\text{-}35)$$

where $A_1(0)$ is the amplitude of the incident light at z = 0 and the coupling efficiency is:

$$\eta = \left|\frac{A_2(L)}{A_1(0)}\right|^2 = \tanh^2|\kappa_{12}|L \qquad (3\text{-}36)$$

For the case when $\Delta\beta \neq 0$, the solutions to (3-31) and (3-32) become:

$$A_1(z) = e^{i\left(\frac{\Delta\beta}{2}\right)z}\frac{s\cos s(L-z)+\frac{i\Delta\beta}{2}\sinh s(L-z)}{s\cos sL+\frac{i\Delta\beta}{2}\sinh sL}A_1(0) \qquad (3\text{-}37)$$

$$A_2(z) = e^{-i\left(\frac{\Delta\beta}{2}\right)z}\frac{-i\kappa_{12}^*\sinh s(L-z)}{s\cos sL+\frac{i\Delta\beta}{2}\sinh sL}A_1(0) \qquad (3\text{-}38)$$

where $A_1(0)$ is the amplitude of the incident light at z = 0, and

$$s^2 = \kappa_{12}^*\kappa_{12} - \left(\frac{\Delta\beta}{2}\right)^2 \qquad (3\text{-}39)$$

The coupling efficiency is then:

$$\eta = \left|\frac{A_2(L)}{A_1(0)}\right|^2 = \frac{|\kappa_{12}|^2\sinh^2 sL}{s^2\cosh^2 sL+\left(\frac{\Delta\beta}{2}\right)^2\sinh^2 sL} \qquad (3\text{-}40)$$

The coupling efficiencies for both transmissive and reflective VBGs with respect to the phase mismatching condition are shown as Fig 3.3. The phase mismatching can occur when the incident angle and/or the wavelength of the laser drift. The simulation assumes 1 μm wavelength TE polarized incident light at normal incident angle. Typical VBGs index modulation n_1 is around 250 ppm. Under these conditions, the calculated grating thickness for near perfect coupling efficiencies are L = 6.28 mm for the transmissive VBGs and L = 3.82 mm for the reflective VBGs. We use Mathematica computer software for all the modeling and simulation throughout this dissertation.

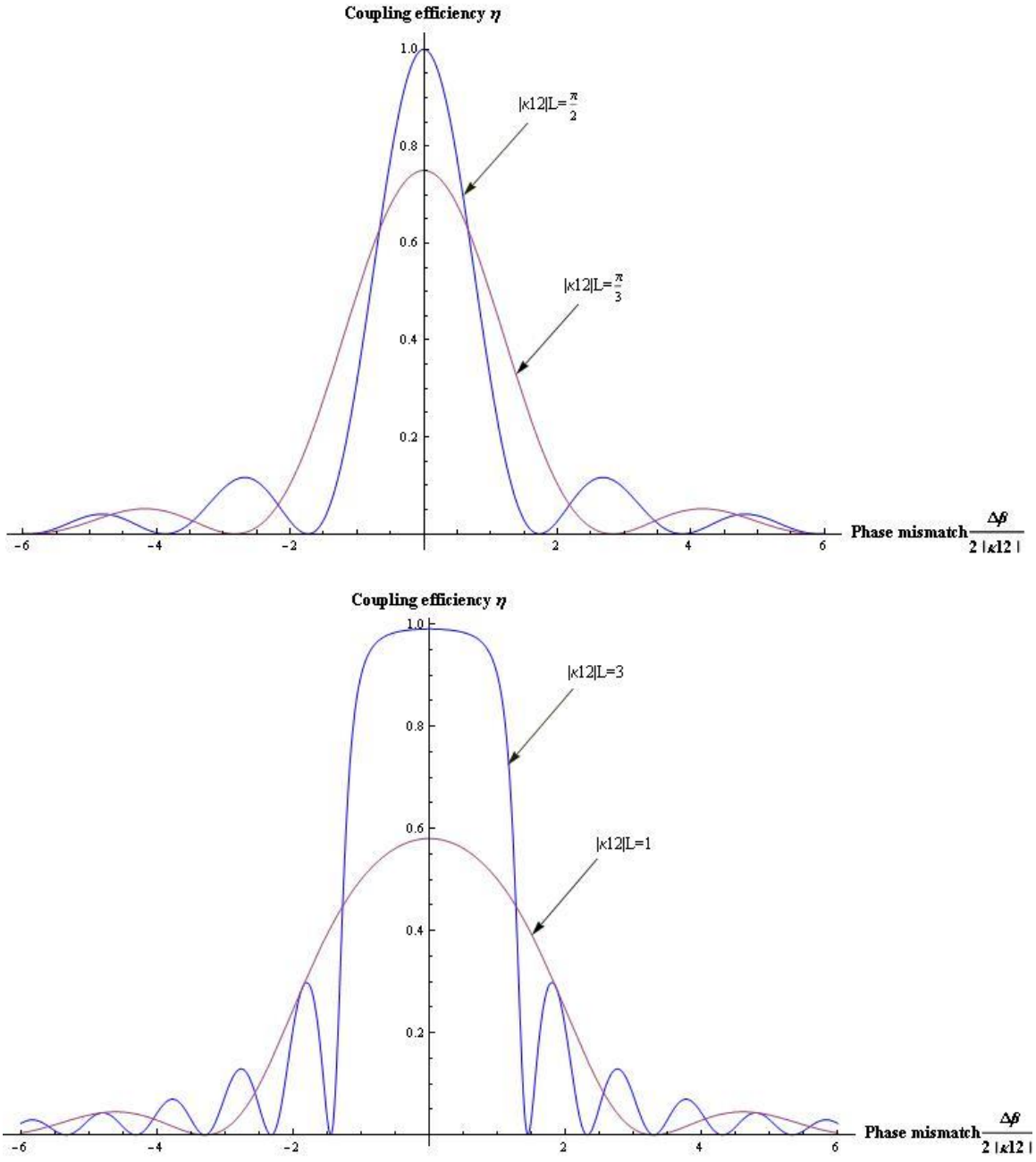

Fig 3.3 Coupling efficiency simulation of transmissive VBGs (top) and reflective VBGs (bottom)

3.2 Theoretical Modeling of Multiplexed Volume Bragg Gratings

We also study the beam combining mechanism of multiplexed volume Bragg gratings (MVBGs) through the coupled wave theory. MVBGs are multiple holographic gratings written on top of each other in the same PTR glass as shown in Fig 3.4. The diffraction efficiency of each individual output is controlled by the tilt angle and thickness of the gratings. In this section, we first study the beam combining effect of the transmissive MVBGs followed by the study of the reflective MVBGs.

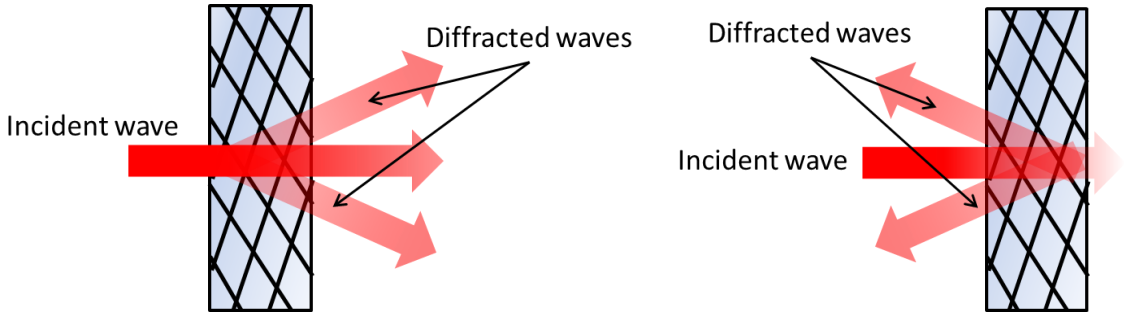

Fig 3.4 Transmissive (left) and reflective (right) MVBGs beam splitters

3.2.1 Beam Combining Simulation of Transmissive Multiplexed Volume Bragg Gratings

As described in the previous section, we can analyze the interaction of input laser and the VBGs through coupled wave equations. Now we will apply the same theory to simulate beam combining effect of multiple lasers using the transmissive MVBGs. Assuming material loss through the transmissive MVBGs is negligible, a system of coupled wave equations using slowly varying envelope approximation (SVEA) under the perfect phase matching condition ($\overrightarrow{\beta_{incident}} - \overrightarrow{\beta_{diffracted}} = \vec{K}$, where $\vec{K}$ represents grating vector) can be expressed as:

$$\frac{dE_j(z)}{dz} = -i\kappa_o E_o(z),\ \frac{dE_o(z)}{dz} = -i\sum_{j=1}^{j=N}\kappa_j E_j(z),\ j = 1,2,\dots N \qquad (41)$$

where N represents the total number of the combining channels, $E_j(z)$ are input laser fields, and $E_o(z)$ is the combined output field. The complex coupling coefficients κ_j and κ_o are defined by both index modulation of the MVBGs and the propagation angle and polarization orientation of the incident lasers and combined output. After applying boundary conditions for the given MVBGs with thickness L, input fields $E_j(0)$, and $E_o(0) = 0$, solutions to the characteristic efficiency can be represented as:

$$\eta = \frac{|\sum_{j=1}^{j=N} E_j(0)\kappa_j|^2 \, |Sinh^2(-\mathrm{KL})|}{\mathrm{K}^2 \sum_{j=1}^{j=N} |E_j(0)|^2}, \quad \mathrm{K}^2 = \sum_{j=1}^{j=N} {\kappa_j}^2, \qquad \kappa_{j,o} = \frac{\pi}{\lambda_0} n_1 \qquad (42)$$

where n_1 is the depth of the index modulation. Here we assume all input lasers have the same TE polarizations and the incident angles are near normal. The transmissive MVBGs provided by OptiGrate Inc. is capable of combing five laser channels at 1064 nm wavelength, thus we model the beam combining effect base on the similar situation. Fig 3.5, Fig 3.6, and Fig 3.7 show the simulation results for five input lasers at 1 μm wavelength and n_1 of 250 ppm. Fig 3.5 and Fig 3.6 show the combining efficiency is highly sensitive to the thickness of the MVBGs; however it has good tolerance for mismatched input power ratios. According to the simulation, it is still possible to obtain greater than 80% combining efficiency when four of the input lasers lose 60% of their optimal power. This is particularly important for high power applications as the input laser powers may not be at the same level. Fig 3.7 shows the power transfer relationship between the input lasers and combined output at different MVBGs thickness. We can see noticeable power transfer between the input lasers at certain thickness when the combined output is low.

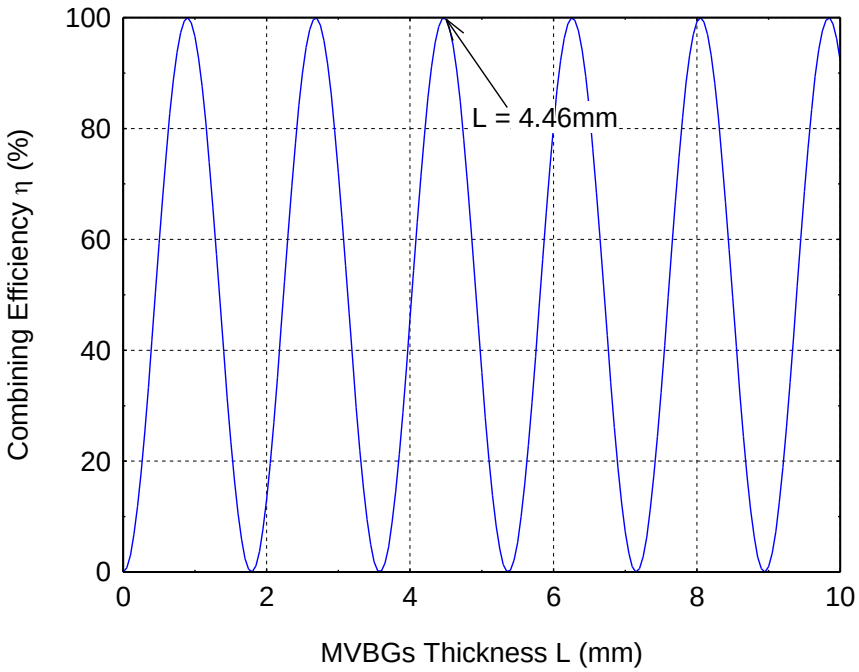

Fig 3.5 Combining efficiency as a function of the transmissive MVBGs thickness assuming all five input lasers have the same power level

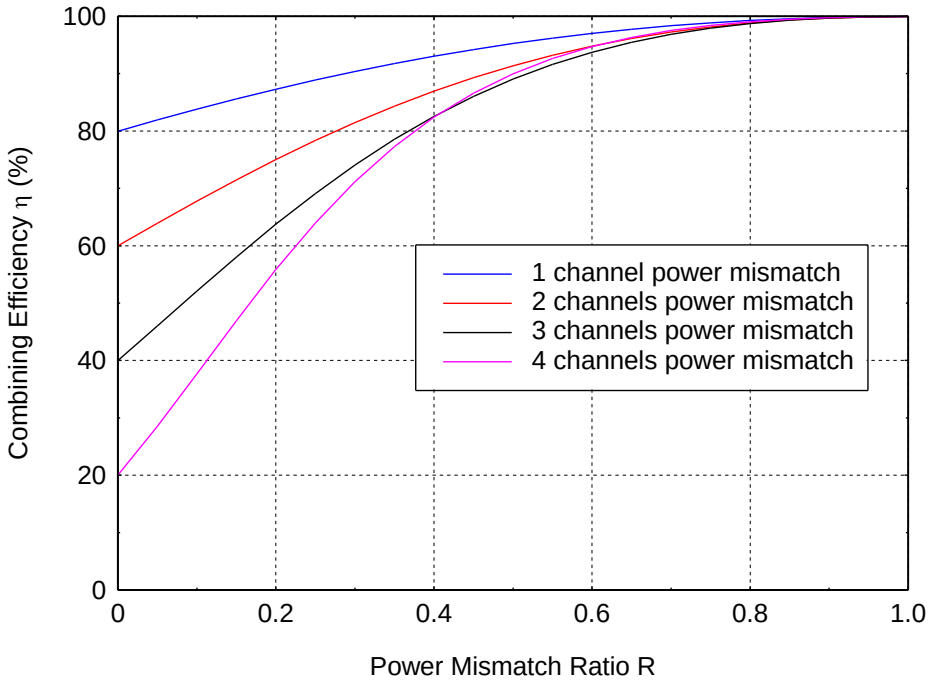

Fig 3.6 Combining efficiency with mismatched input powers using the 4.46 mm thickness transmissive MVBGS

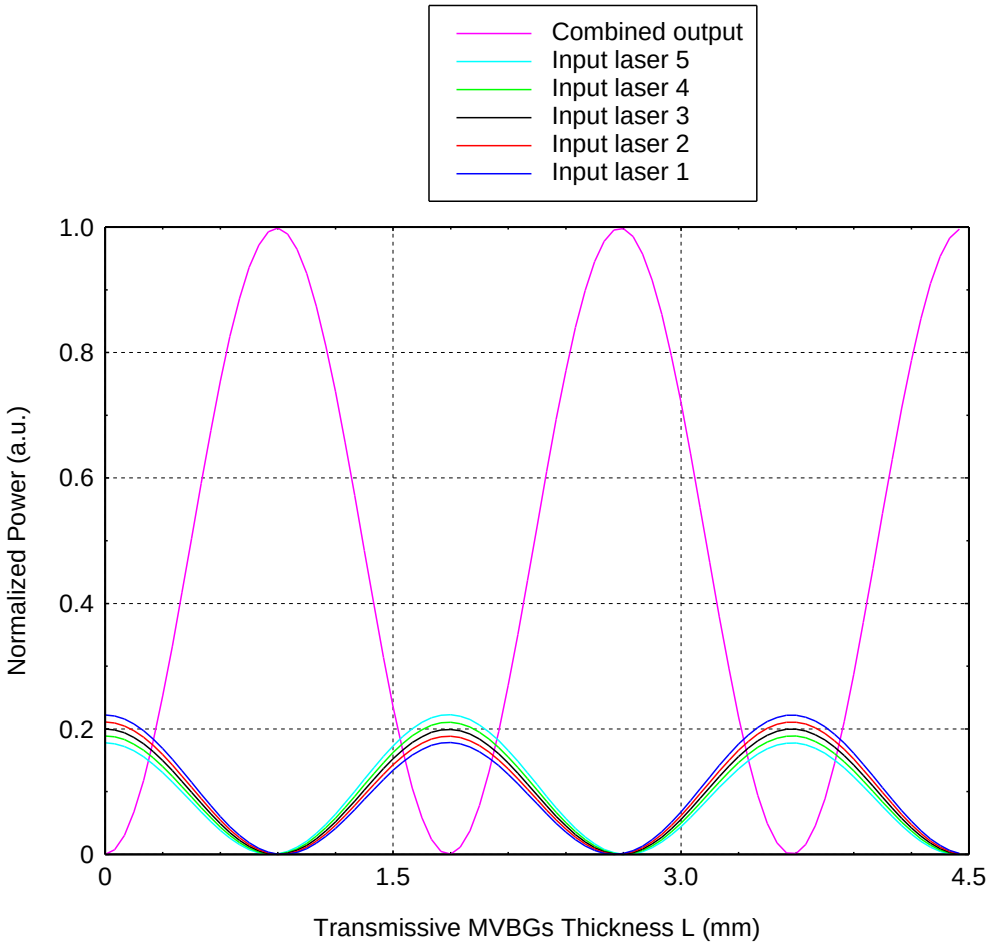

Fig 3.7 Power transfer inside the transmissive MVBGs, input lasers have 5% power difference between each other

3.2.1 Beam Combining Simulation of Reflective Multiplexed Volume Bragg Gratings

Similar to the transmissive MVBGs, we also analyze the interaction of input and output beams inside the reflective MVBGs through coupled wave theory. Fig 3.8 shows the MVBGs in the beam combiner scheme for combining two laser fields, where E1 and E2 are the input beams and Eo represents the combined output, and L is the thickness of the MVBGs. A set of coupled wave equation using slowly varying envelope approximation (SVEA) in the optimal Bragg matching conditions can be formulated as:

$$\frac{dEj(z)}{dz} = i\kappa_o E_o(z),\ \frac{dEo(z)}{dz} = -i\sum_{j=1}^{2}\kappa_j E_j(z); \qquad j = 1,2 \qquad (43)$$

where $E_j(z)$ are input laser fields and $E_o(z)$ is the combined output field. κ_j and κ_o are the complex coupling coefficients defined by material property of the MVBGs and propagation angle and polarization orientation of the incident lasers and combined output. Here we also assume all input lasers have the same TE polarizations and the incident angles are near normal.

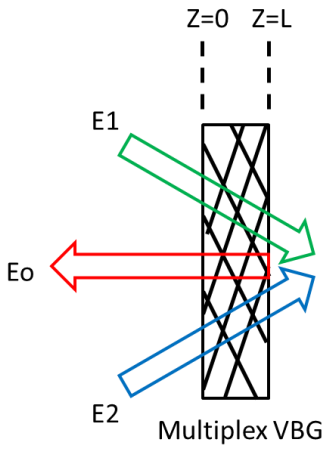

Fig 3.8 Waves E1, E2, Eo, interacting in the reflective MVBGs

After applying boundary condition where the incident fields $E_1[z]$ and $E_1[z]$ at z = 0 are A and B, respectively, and output field $E_o[z]$ is equaled to 0 at z = L, the solutions of the SVEA system equations then become:

$$E_1[z] = \frac{\kappa 2(-B\kappa 1 + A\kappa 2) + \kappa 1(A\kappa 1 + B\kappa 2)\mathrm{Cosh}[(L-z)K]\mathrm{Sech}[LK]}{K^2} \qquad (45)$$

$$E_2[z] = \frac{\kappa 1(B\kappa 1 - A\kappa 2) + \kappa 2(A\kappa 1 + B\kappa 2)\mathrm{Cosh}[(L-z)K]\mathrm{Sech}[LK]}{K^2} \qquad (46)$$

$$E_o[z] = -\frac{i(A\kappa 1 + B\kappa 2)\mathrm{Sech}[LK]\mathrm{Sinh}[(L-z)K]}{K},\ K = \sqrt{{\kappa_1}^2 + {\kappa_2}^2} \qquad (47)$$

And the combining efficiency is represented as:

$$\eta = \frac{|E_o[0]^2|}{|E_1[0]^2| + |E_2[0]^2|} = \frac{|\sum_{j=1}^{j=2} E_j(0)\kappa_j|^2\ |Tanh^2(\mathrm{KL})|}{\mathrm{K}^2 \sum_{j=1}^{j=2} |E_j(0)|^2},$$

$$K^2 = {\kappa_1}^2 + {\kappa_2}^2, \kappa_1 = \kappa_2 = \kappa_o = \frac{\pi}{\lambda_0} n_1 \quad (48)$$

where n_1 is the depth of the index modulation. Fig 3.9, Fig 3.10, and Fig 3.11 show the simulation results for combining two lasers using the reflective MVBGs. Fig 3.9 shows the combining efficiency at different grating thickness L when the two input powers are identical. The simulation result also shows 99.97% combining efficiency is achievable at L = 4 mm. Fig 3.10 and Fig 3.11 show the case where the input powers are not identical. As the ratio of the input powers decreases (i.e. the power difference between the two lasers increases), the low interference visibility causes the combining efficiency to drop. However, near 90% combining efficiency can still be achieved even if one of the input power drops down to half of its optimal power. This shows the combining efficiency of the reflective MVBG is rather stable even when the power difference between the two lasers increases to 50% given the two lasers are still perfectly phase matched. In Fig 3.11, blue and green curves represent the input lasers and red curve shows the combined output inside the 4 mm thickness reflective MVBGs. The simulation assumes the two lasers have 20% power difference between each other.

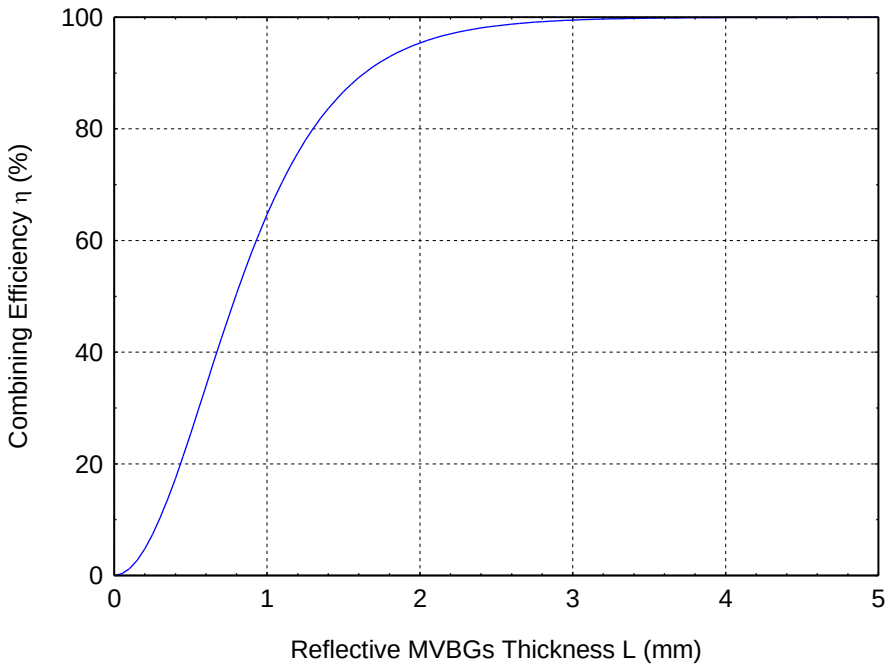

Fig 3.9 Combining efficiency as a funciton of reflective MVBGs thickness

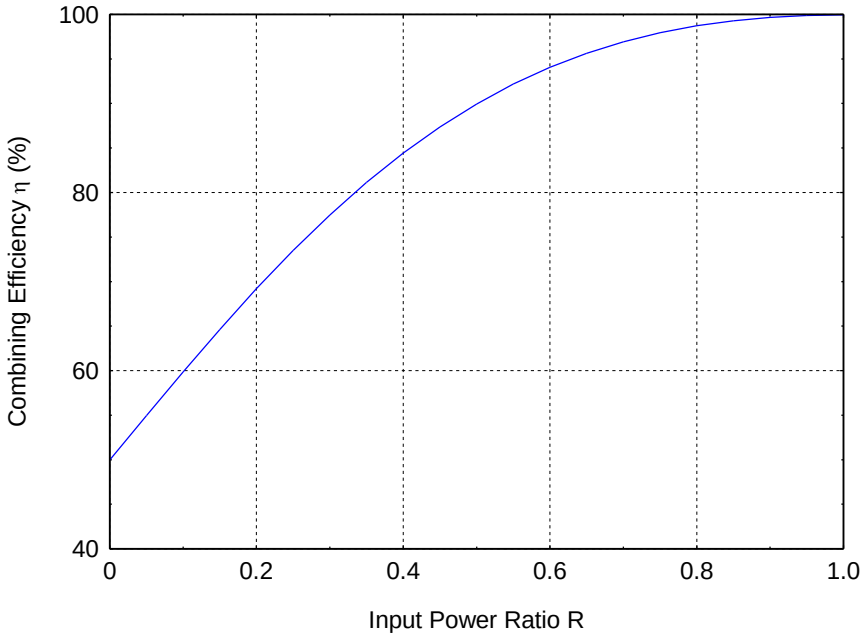

Fig 3.10 Change of combining efficiency with respect to the power ratio of the two input lasers using the 4 mm thickness reflective MVBGs

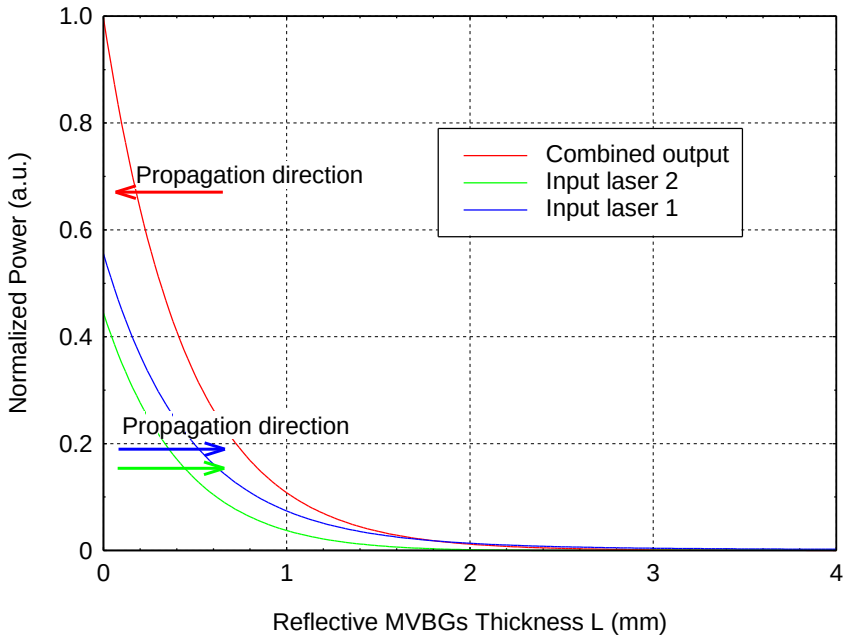

Fig 3.11 Wave interactions within the reflective MVBGs

Lastly, we verify if the solutions satisfy the convervation of energy. Fig 3.11 shows the input and output characteristics inside the reflective MVBGs. On the left hand side, the normalized input powers are 0.556 and 0.444 and the output power is approximately 0.99635 from the simulation. On the right hand side, we have 0.00313 and 0.00052 of "loss" power coming from the two input lasers at 4 mm of MVBGs thickness. Assuming perfect phase matching condition, the loss power can either come from the unequal input powers and/or suboptimal MVBGs thickness. Nevertheless, the total input power is verified to be equaled to output power plus the loss power, thus the solutions of the coupled wave equations satisfy energy conservation.

3.3 Summary

Holographic volume Bragg gratings (VBGs) recorded inside the specially formulated photo-thermal-refractive glass provides a way to manipulate the propagation direction of the incoming lasers. The interaction of the waves inside the VBGs and multiplexed VBGs

(MVBGs) can be realized through the coupled wave theory. MVBGs are multiple gratings embedded in a single optical element capable of splitting and combining incident waves. In this chapter, we simulated the characteristics of transmissive and reflective MVBGs beam combiners based on the coupled wave theory. While it is possible to obtain excellent beam combining efficiency for the transmissive MVBGs under perfectly phase matched condition, the performance is strongly impacted by the thickness of the combining element. On the other hand, the reflective MVBGs can deliver good combining efficiency without the restriction of the thickness. However, the combined output from the reflective MVBGs is directed back towards the incoming lasers. It is sometimes inconvenient and problematic to have the high power combined output propagating towards the laser sources. Therefore, from the beam combining perspective, the choice of MVBGs depends on not only the type of the laser platform also the power level of each individual laser source.

In the next two chapters, we will conduct experimental study of MVBGs beam combining using high brightness lasers. In chapter 4, we will first describe the study of active coherent beam combining for five high power fiber lasers using transmissive MVBGs and LOCSET phase locking scheme, followed by two passive coherent beam combining arrangements using reflective MVBGs for combining two fiber laser amplifiers at low power levels. Chapter 5 comprises the VBGs beam combining study for vertical cavity surface emitting lasers (VECSELs). VECSELs are semiconductor lasers capable of producing high brightness output and all the VECSELs used in this thesis are in optically injected configurations. For beam combining VECSELs, first we will conduct the coherent addition study using VBGs in a two chips z-cavity experimental setup. Then

we will outline the experimental setup and results of a wavelength beam combining scheme for combining two VECSELs using the reflective MVBGs.

Chapter 4 : Experiment on Coherent Beam Combining of Fiber Lasers Using Multiplexed Volume Bragg Gratings

4.1 Introduction of Fiber Laser and Fiber Lasers Beam Combining

Beam combining techniques using gratings for high power fiber laser arrays have shown advancement in both coherent and incoherent beam combining schemes. Coherently, diffractive optical elements (DOE), complex surface gratings, have demonstrated the capability in scalability in quantity and power handling [38, 39]. On the other hand, incoherent beam combining has achieved near 10 kW combined output using the multilayer dielectric gratings [53]. As the individual fiber laser element reaches higher output power, the requirements for beam combining scheme and/or gratings element become more stringent. Gratings design criteria such as angle and power of diffraction, absorption, and bandwidth are the primary contribution to the combining efficiency. Furthermore, a stable phase locking scheme is required for coherent beam combining techniques. Common phase locking scheme such as stochastic parallel gradient descent algorithm (SPGD) [54] or locking of optical coherence by single-detector electronic frequency tagging (LOCSET) [29] is widely used and both schemes have shown significant successes on phase locking for coherent beam combination of high power fiber lasers [36, 38].

To exploit alternative approach for coherent beam combination, we proposed to conduct a study using multiplexed volume Bragg gratings (MVBGs) [4]. In principle, there are two differences between surface gratings and holographic volume gratings when it comes to coherent beam combination. First difference is the order of diffractions, for surface gratings, the diffraction efficiency for the higher order diffraction increases as more laser channels are added to the beam combining system. The volume gratings use

the first order diffraction for each input beam and it is necessary to inscribe a new set of gratings in the same photosensitive glass for combining an additional channel. The other difference is apparent: surface versus volume. The sophisticated gratings are etched on the surface for the surface gratings to split equally between the diffraction orders either on transmission or reflection. In order to reduce the loss through the combiner, reflective scheme for high power beam combining is often implemented [39]. However, in the scheme of passive coherent beam combining, it is sometimes more convenient to use the transmissive Dammann surface gratings [49]. As for the holographic volume gratings, the inscriptions can be orientated to produce both transmissive and reflective gratings as described in the previous chapter, however since the gratings are imbedded inside the volume of photosensitive glass, there exists intrinsic absorption through the glass regardless of the beam combining geometry. Nevertheless, both spectral beam combining and passive coherent coupling of fiber lasers have been demonstrated with high-efficiency MVBGs beam combiners [26, 50].

Hereby, we intend to first validate the active coherent beam combining scheme for five fiber lasers based on the transmissive MVBGs with self-referenced LOCSET active phase locking technique. With a single detector, LOCSET measures the phase of individual lasers, each with a unique modulation frequency and provides phase error signals to each phase modulator for phase correction. The coherence between the lasers is achieved when all phase error signals reach zero. A more detailed description of the LOCSET theory is referenced in Appendix A. In addition to the phase locking mechanism, we introduce the beam combining element MVBGs to spatially overlap the input laser beams. For combining five fiber lasers, four sets of holographic gratings are

multiplexed in a single PTR wafer such that at near normal incident angle, the beam splits equally into five beams under optimal Bragg condition. When using such MVBGs as a combiner, it provides efficient superposition of the five input lasers in both the near and far fields.

Besides the active coherent beam combining, we have also conducted passive coherent beam combining of two fiber laser amplifiers using the reflective MVBGs. We implemented two laser cavity geometries: standing wave cavity and seeded unidirectional ring cavity. The results showed limited power scalability for the standing wave cavity due the gain pulsation effect at high pump power. On the other hand, the seeded unidirectional ring cavity did not exhibit the high peak power pulsation and we were able to obtain > 90% combining efficiency at 5 W combined output with excellent beam quality. Before we start with the beam combining discussion, we will first briefly introduce the fiber laser amplifiers used in the experiments.

4.1.1 Introduction of Fiber Laser Amplifier

Rare earth elements such as Erbium (Er) and Ytterbium (Yb) are commonly used dopants in the double-clad optical active gain fibers as they exhibit small quantum defect when excited with proper pump wavelength. Fig 4.1 shows the schematic of a double-clad gain fiber structure designed specifically for cladding pumping, where the refractive index relationship is n1 > n2 > n3. Commercial telecommunication systems utilize Er-doped fibers for their low noise and eye-safe feature to enhance the transmitted signals. Yb-doped fibers are often used in high power solid state lasers or amplifiers due to their high absorption efficiency. Typically, Er-doped fiber amplifiers are pumped at either 980 nm or 1480 nm wavelength for amplifying 1550 nm light, depending on the absorption and

noise requirements of the system. Yb-doped fiber amplifiers are generally pumped at 980 nm wavelength and amplifying 1064 nm light. Basically, an optical fiber amplifier acts as a brightness converter which transfers energy from the multimode pump light into the single mode seed source. In this thesis, we use Yb-doped fibers as the amplifier gain medium to achieve the highest possible gain for the 1064 nm master oscillator laser source.

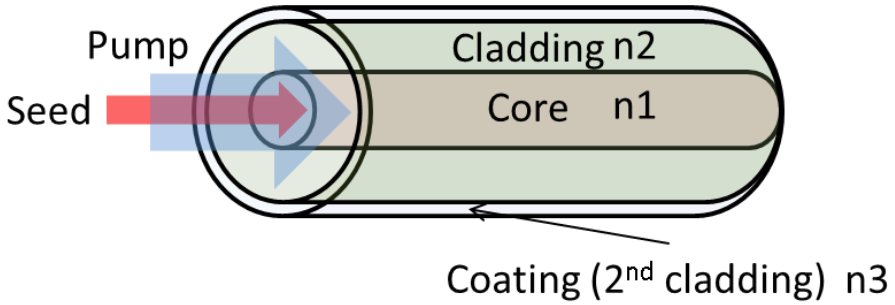

Fig 4.1 Seed and pump light propagation in double-clad gain fibers

In terms of fiber amplifier configurations, there are generally three types of pumping classes: co-pumping, counter-pumping, and bidirectional-pumping. The primary purpose of counter-pumping and bidirectional-pumping is to introduce a natural temperature gradient in the active fiber for mitigating the nonlinear stimulated Brillouin scattering during the amplification process [55]. Because both the counter-pumping and bidirectional-pump schemes increase the risks of damaging the amplifiers and the nonlinear effect is outside the scope of the proposed research, we implement all of the fiber amplifiers using the co-pumping method. The setup of the co-pumping configured three-stage fiber amplifiers is shown in Fig 4.2. Using tapered fiber bundles as the coupling mechanism for guiding the pump light into the cladding of the gain fibers and optical fiber isolators to prevent backward propagating light from later stages.

The multi-stage amplification is necessary as the master oscillator alone does not have sufficient power to achieve optical transparency at seed wavelength in the last amplification stage. In the high power fiber laser beam combining experiment, we constructed three-stage co-pumped amplifiers using the 1064 nm narrow linewidth master oscillator laser as the seed source and 976 nm semiconductor laser diodes as pump source.

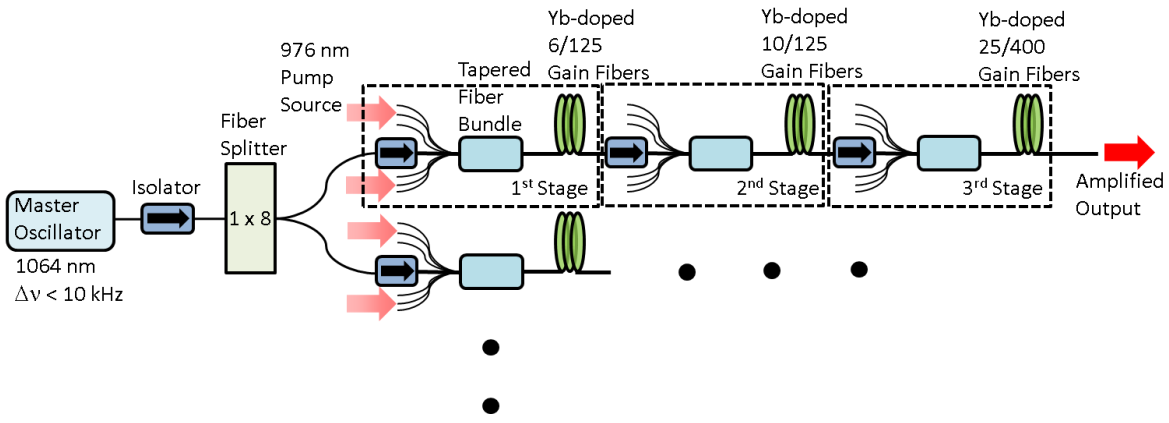

Fig 4.2 Three-stage fiber amplifier array with co-pumping scheme

We also use other fiber optics components such as tapered fiber bundles and fiber pigtailed optical isolators for the construction of fiber laser amplifiers. Tapered fiber bundle merges all of the pump light together into the cladding of the gain fibers while maintain the light from the master oscillator in the core. Because of the close-packed geometry, the fiber arrangement generally forms a hexagonal shape in the fiber bundle. Optical fiber isolators are critical components in the fiber amplifiers as they prevent light propagating backward to damage the front end of the amplifiers and cause catastrophic failure. As shown in Fig 4.3, conventional optical isolator consists of three parts: an entrance polarizer orientated to transmit the linearly polarized input, a Faraday rotator to rotate the polarization angle of the incoming light by 45°, and an exit polarizer orientated

to transmit the rotated 45° linearly polarized light. When the light is reflected or scattered backward, assuming unpolarized light, half of the backward propagating light is blocked by the exit polarizer and after the Faraday rotator, the other half is blocked by the entrance polarizer. This is due to the nonreciprocal Faraday rotation causing the polarization of the backward propagating light to be perpendicular to the input light.

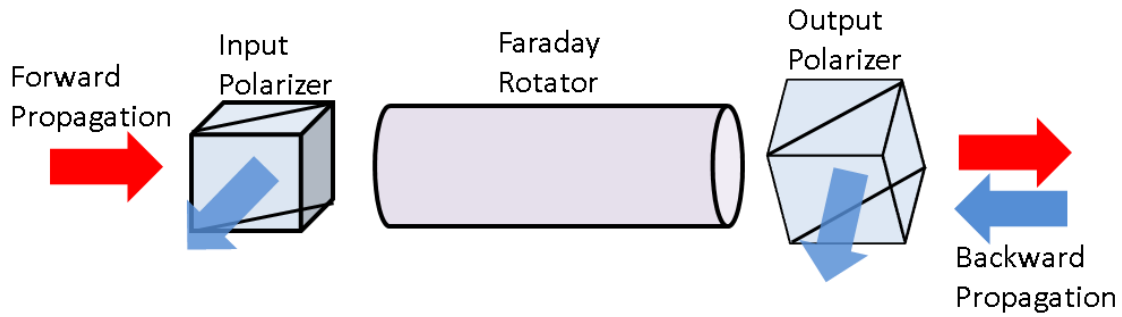

Fig 4.3 Isolation mechanism for conventional optical isolators

In our three-stage amplifications, the fiber geometry of the first stage is 6/125 (6 μm core diameter/125 μm cladding diameter), 10/125 for the second stage, and 25/400 for the last amplification stage. The increase in core diameter serves two primary purposes. First, to increase the damage threshold at the output and second, to reduce the active fiber length required for amplification. Furthermore, all the fibers used in the amplifier system are polarization maintaining (PM) fibers as shown in Fig 4.4. PM fibers have stress rods which induce high birefringence in the fibers so if the linearly polarized input light is aligned with the fibers axis, the PM fibers will maintain its polarization state during the propagation inside the fibers. With the use of PM fibers and optical isolators, we are not only able to obtain the highest transmission through the multi-stage amplifications but also ensure any backward traveling light caused by either a reflection or scattering will not travel backward to disturb the earlier stage amplifications and damage the amplifier system.

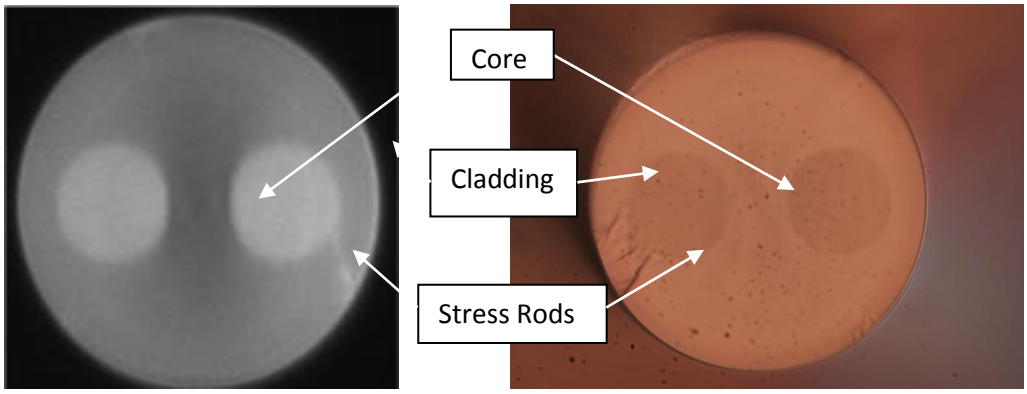

Fig 4.4 Cross section images of the PM single mode fibers.

4.1.2 Basic Fiber Laser Amplifier Modeling and Simulation

Yb-doped fibers, in the basic sense, have quasi-three level or four-level energy transition behaviors depending on the absorption and emission wavelengths as shown in Fig 4.5 [56]. The energy diagram consists of two manifolds, the ground manifold ($^2F_{7/2}$) with four Stark levels, and the higher excited manifold ($^2F_{5/2}$) with three Stark levels. Energies in wave-numbers are indicated on the left side. When the emission wavelength is less than 1080 nm, the lower transmission state is close to the ground state which is similar to a quasi-three level system. Because there is significant population in this level at thermal equilibrium, the reabsorption of the emission photons occurs and the system exhibits higher lasing threshold. The laser displays four-level energy transition behavior when operating beyond 1080 nm emission wavelength. In this regime, the population inversion is easily achieved due to the larger energy gap between the ground state and lasing state.

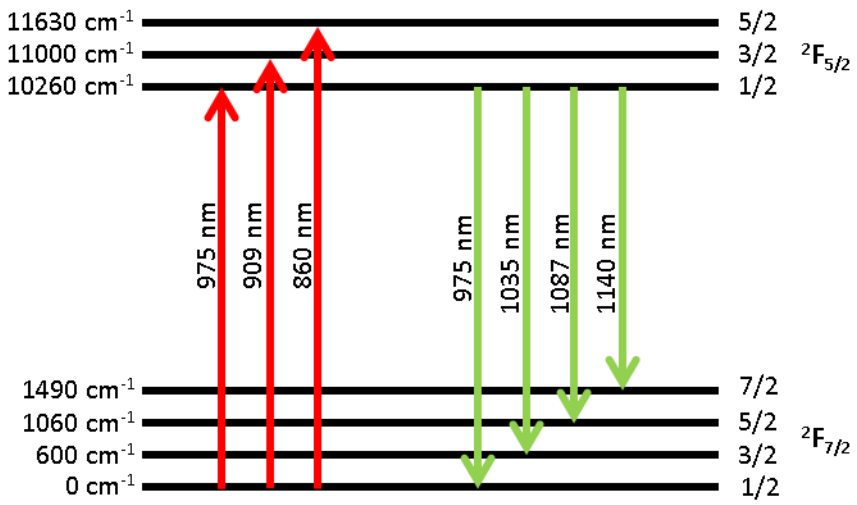

Fig 4.5 Yb3+ energy level structure

We start with the quasi-three level system for modeling the amplification process of the 1064 nm wavelength seed source in the Yb-doped fiber amplifier. When the non-radiative relaxations to ground state are extremely rapid, the system can be reduced to two-level as shown in Fig 4.6 [57]. Here we use 976 nm wavelength pump source and assuming amplified spontaneous emission (ASE) and nonlinear effects in the fibers are negligible.

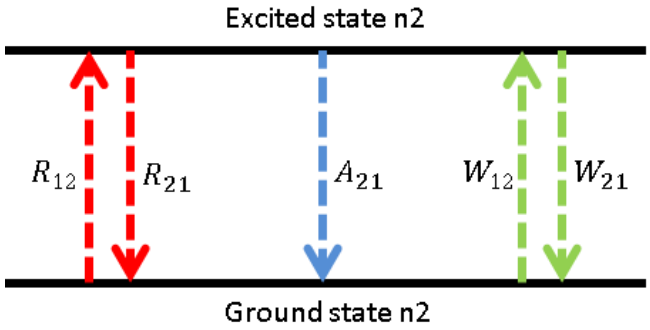

Fig 4.6 Energy level diagram for two-level system

The Yb upper (n_2) and lower (n_1) levels populations are represented by the rate equations:

$$\frac{dn_2}{dt} = (R_{12} + W_{12})n_1 - (R_{21} + W_{21} + A_{21})n_2 \qquad (4\text{-}1)$$

$$\frac{dn_1}{dt} = -(R_{12} + W_{12})n_1 + (R_{21} + W_{21} + A_{21})n_2 \qquad (4\text{-}2)$$

where R_{12} and R_{21} are the pump excitation and relaxation rates, W_{12} and W_{21} are the absorption and emission rates of the seed source, respectively, and A_{21} is the spontaneous emission rate. These transition rates can be written in terms of respective cross sections and intensities:

$$R_{12} = \frac{I_p(z)\sigma_{pa}}{h\nu_p}, \qquad R_{21} = \frac{I_p(z)\sigma_{pe}}{h\nu_p} \qquad (4\text{-}3)$$

$$W_{12} = \frac{I_s(z)\sigma_{sa}}{h\nu_s},\ W_{21} = \frac{I_s(z)\sigma_{se}}{h\nu_s} \qquad (4\text{-}4)$$

$$A_{21} = \frac{1}{\tau} \qquad (4\text{-}5)$$

where σ_{pa}/σ_{pe} and σ_{sa}/σ_{se} are the pump and seed absorption/emission cross sections, respectively. I_p and I_s are the pump and seed intensities. τ is the radiative lifetime between the two energy levels. ν_p and ν_s are the transition frequencies for the pump and seed sources. In our simulation, we obtain the information of cross sections for Yb-doped fibers using Fig 4.7.

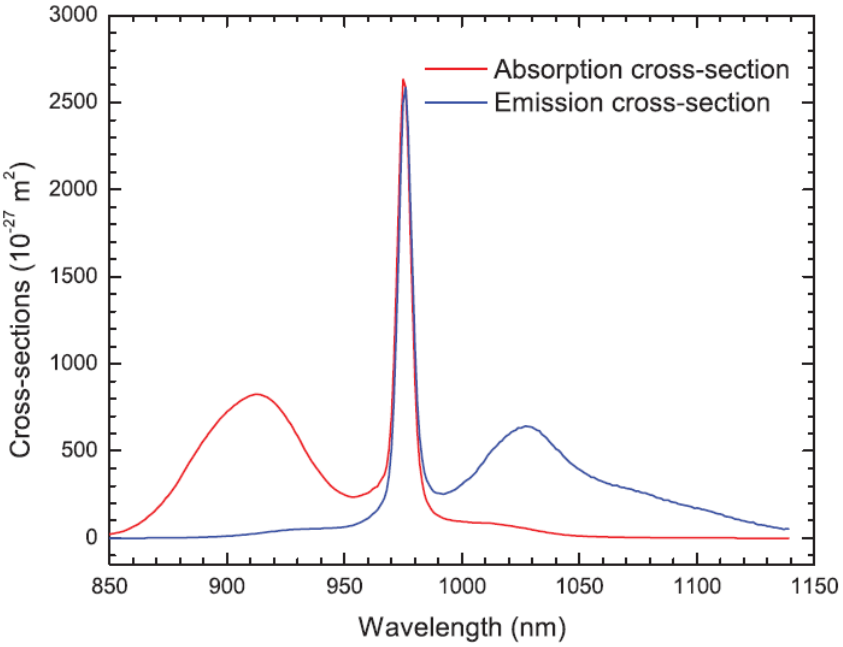

Fig 4.7 Absorption and emission cross-sections of Yb in germanosilicate glass

By setting $\frac{dn_2}{dt} = \frac{dn_1}{dt} = 0$ and $n_1 + n_2 = N_o$ with N_o representing the total ion population density, we obtain the steady state solutions:

$$n_1(z) = \frac{N_o\tau\{h\nu_s\sigma_{pa}\, I_p(z)+h\nu_p\sigma_{sa}\, I_s(z)\}}{h\nu_s(\sigma_{pa}+\sigma_{pe})\tau\, I_p(z)+h\nu_p\{h\nu_s+(\sigma_{sa}+\sigma_{se})\tau\ \ I_s(z)\}} \qquad (4\text{-}6)$$

$$n_2(z) = \frac{N_o\{h\nu_s\sigma_{pe}\tau\, I_p(z)+h\nu_p(h\nu_s+\sigma_{se}\tau\, I_s(z))\}}{h\nu_s(\sigma_{pa}+\sigma_{pe})\tau\, I_p(z)+h\nu_p\{h\nu_s+(\sigma_{sa}+\sigma_{se})\tau\ \ I_s(z)\}} \qquad (4\text{-}7)$$

The population is known for each level as a function of the total population with the gain and loss for the pump and signal at a given position z along the fiber. Therefore, the coupled rate equations for the pump $I_p(z)$ and the seed $I_s(z)$ intensities of the system can be expressed as:

$$\frac{dI_p(z)}{dz} = \eta_p\left(\sigma_{pe}n_2(z) - \sigma_{pa}n_1(z)\right)N_oI_p(z) \qquad (4\text{-}8)$$

$$\frac{dI_s(z)}{dz} = \eta_s(\sigma_{se}n_2(z) - \sigma_{sa}n_1(z))N_oI_s(z) \qquad (4\text{-}9)$$

where η_p and η_s are the overlap factor for the pump and seed, respectively. Assuming the multimode pump has intensity that is constant over the cross section of the fibers, the overlap factor of the pump η_p can be approximated as the ratio squared of the core diameter and cladding diameter. For the single mode fibers, we presume the seed source has a Gaussian shape beam profile and the overlap factor of the seed η_s can be obtained using the Marcuse's Formula [58]:

$$\frac{1}{\eta_s} = 0.65 + \frac{1.619}{V^{3/2}} + \frac{2.879}{V^6} \qquad (4\text{-}10)$$

where V represents the V number of the optical fibers. Marcuse's Formula gives the optimum width of the fundamental Gaussian mode profile that best approximates the actual field distribution of a step-index fiber for the V number values up to 2.405. The V number is a normalized frequency parameter for determining the number of optical modes in the step-index fibers and it can be expressed as:

$$V_{number} = \frac{2\pi}{\lambda} a[NA] = \frac{2\pi}{\lambda} a\sqrt{{n_{core}}^2 - {n_{clad}}^2} \qquad (4\text{-}11)$$

where NA represents the numerical aperture defined by the divergence angle of a fiber, a is the core radius of the fiber, and λ is the seed source wavelength in vacuum. n_{core} and n_{clad} are the refractive index of the core and cladding, respectively.

The coupled differential equations (4-9) and (4-10) were solved using the NDSolve command in Mathematica with the specified Runge-Kutta method. The initial conditions considering a co-propagating pumped amplifier are the following:

$$I_p(0) = \frac{Pump\ Power}{Cladding\ Area} \qquad (4\text{-}12)$$

$$I_s(0) = \frac{Seed\ Power}{Core\ Area} \qquad (4\text{-}13)$$

To find the small signal gain along the fiber length, we substitute the solutions from the above coupled differential equations into the population equations (4-6) and (4-7). The gain equation can then be described as:

$$Gain(z) = \eta_s(\sigma_{se}n_2 - \sigma_{sa}n_1) \qquad (4\text{-}14)$$

Fig 4.8 and Fig 4.9 show the simulation results for the last stage amplification in our co-pumping scheme amplifier chain. The simulation is based on the parameters of the actual amplifier with the total Yb^{3+} ion population density of 2×10^{16} m^{-3} and 4 meters of the 25 μm core/400 μm cladding Yb-doped gain fibers. We provide the amplifier with 3 W of 1064 nm wavelength seed power and a total of 150 W of 976 nm wavelength pump power. The results show near complete absorption of the pump power at the chosen length of the gain fibers and the amplifier exhibits approximately 95% slope efficiency. However, this model only provides the basic prediction without considering quantum defect heating, ASE, and nonlinear effects which can dramatically reduce the slope efficiency of the amplifier. Next, we will compare the simulation with the experimental result.

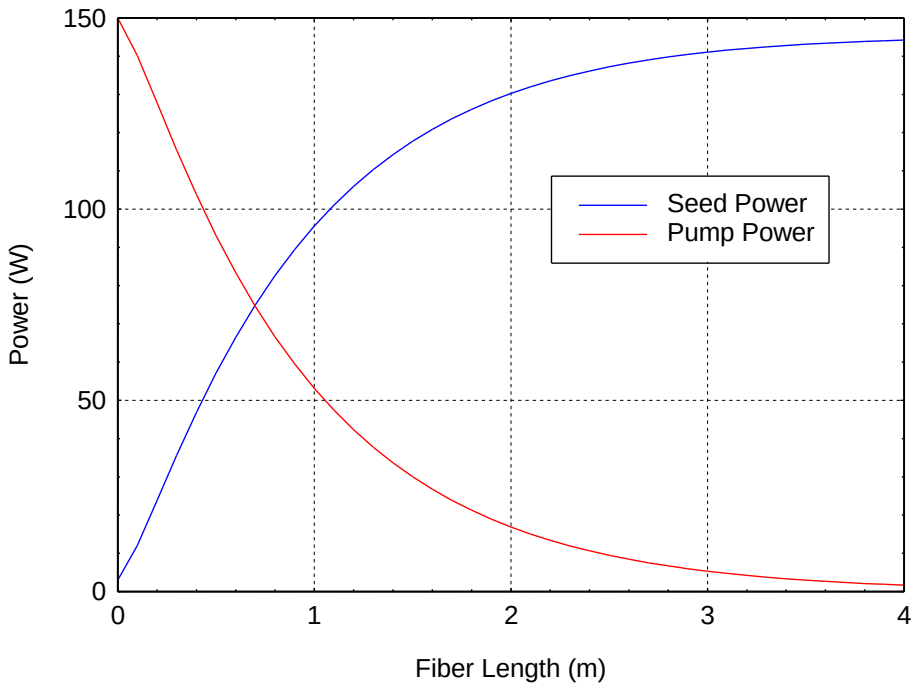

Fig 4.8 Simulation of energy transfer between the pump and seed powers along the 4 meters gain fibers

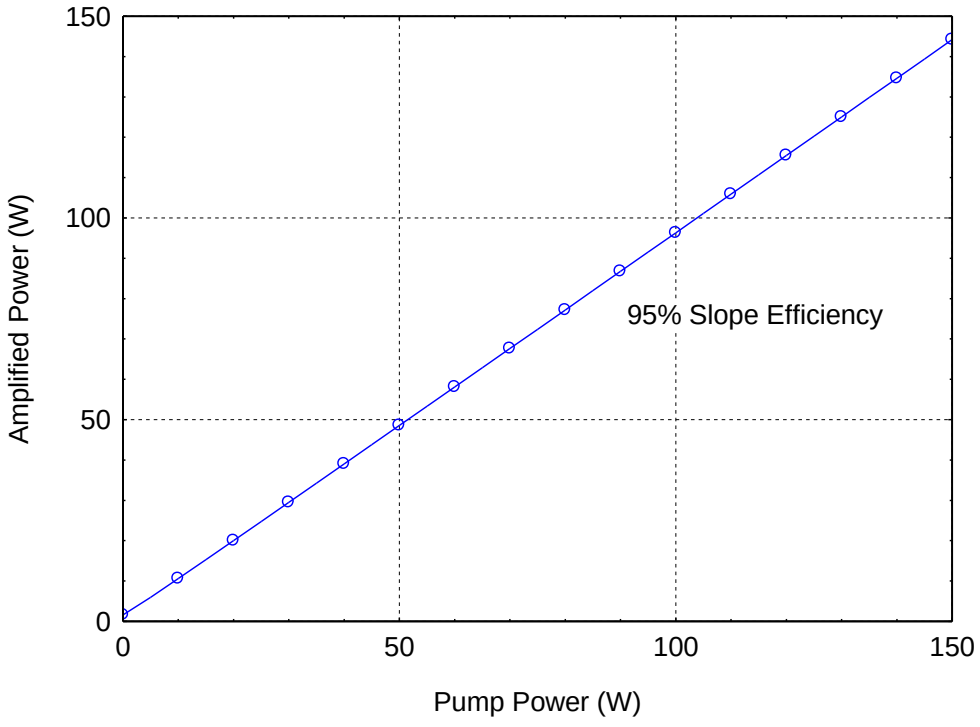

Fig 4.9 Simulation result of the amplified output for the fiber amplifier with 4 meters of gain fibers

4.1.3 Fiber Laser Amplifier Implementation and Experiment

The basic experimental setup is shown in Fig 4.10 using a narrow linewidth 1064 nm laser as seed source for the three-stage amplifier. The seed laser is a solid-state non-planar ring oscillator (NPRO) manufactured by JDS Uniphase with lasing wavelength centered at 1064 nm and spectral linewidth less than 10 kHz. The laser is adjusted to produce approximately 20 mW power input into the first stage amplifier. Fiber pigtailed optical isolators are placed in between each amplifier stage and after the seed source to prevent backward traveling light from damaging the laser amplifier system. We configured the tapered fiber bundle in the co-pumping scheme for coupling pump light into the double clad Yb-doped gain fibers. The specifications of the three fiber amplifier stages are summarized in Table 4.1.

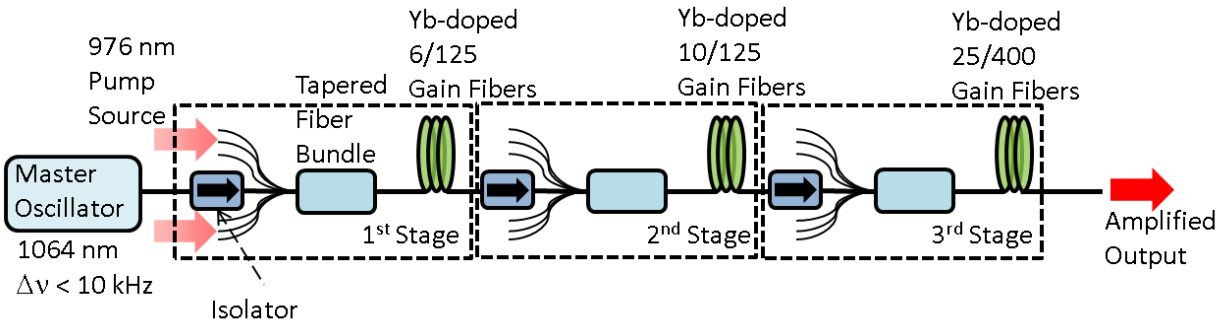

Fig 4.10 Three-stage fiber amplifiers with co-pumping configuration

Table 4.1 Specifications of three fiber amplifier stages

	First Stage Amplifier	Second Stage Amplifier	Third Stage Amplifier
Gain Fiber Core Diameter	6 μm	10 μm	25 μm
Gain Fiber Cladding Diameter	125 μm	125 μm	400 μm
Gain Fiber Length	7.5 m	4 m	4 m
Minimum Input Power After Isolator	0.01 W	0.15 W	3 W
Maximum Output Power	0.5 W	10 W	200 W

In addition, near the end of the gain fibers in each amplifier stage, there is a 5 cm long section of the fibers coated with high index material for removing the unabsorbed pump light in the fibers. So the output of the amplifier only contains purely amplified emission. The performance of the five fiber amplifiers used in the beam combining experiment is shown in Fig 4.11. Except for Laser 2, the average slope efficiency of the lasers is around 85%, which is 10% less than the simulation. This is expected, as not all the loss such as ASE and the nonlinear effects are not included in the modeling. Furthermore, the pump laser diode sources experience wavelength redshift and linewidth broadening at high power is another factor not considered in the simulation which causes reduced slope efficiency.

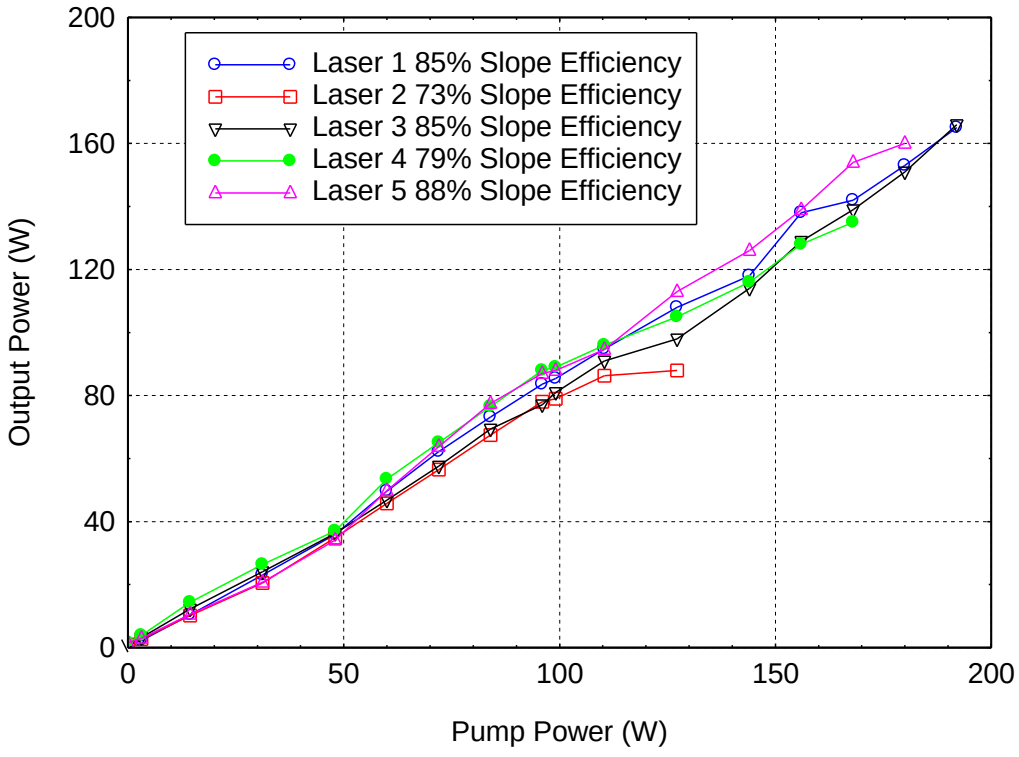

Fig 4.11 Output characteristics of the five fiber amplifiers used in the active coherent beam combining experiment

We captured the output and pump spectra of one of the fiber amplifier using the ANDO optical spectrum analyzer (OSA) as shown in Fig 4.12. The measured center wavelengths for the output and pump are 1064.25 nm and 974.7 nm, respectively. Although the OSA shows resolution limited spectrum for the amplified output, a few nm wide linewidth measured for the pump spectrum is without instrumental limitation.

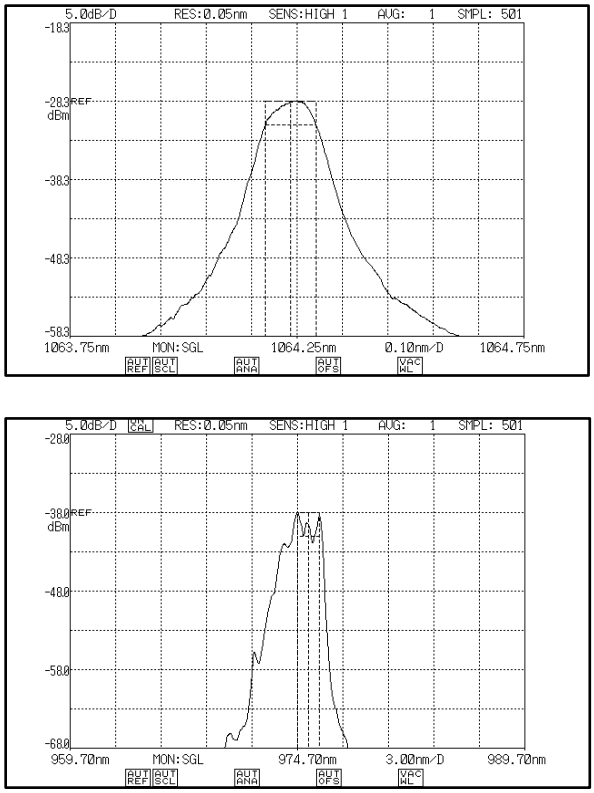

Fig 4.12 Spectral profiles of the amplified output (top) and pump light (bottom)

Above all, we have shown the basic simulation and construction of the Yb-doped fiber amplifier used in the beam combining schemes. The result of the simulation provides a good estimate of a fiber amplifier given the property and dimension of the gain medium. Next we will discuss the beam combining experimental setups and results.

4.2 Active Coherent Beam Combining Using Transmissive Multiplexed Volume Bragg Gratings

In this section, we will discuss the experimental study of active coherent beam combining using the transmissive MVBGs and the LOCSET phase locking scheme.

4.2.1 Experimental Setup

We conduct the experimental beam combining study of a 4.11 mm thick transmissive MVBGs using five fiber lasers at wavelength of 1064 nm. The experimental setup is show in Fig 4.13, where we use the LOCSET active phase control scheme to achieve optimal coherence between the five input lasers. The operation theory of the LOCSET is described in Appendix A. The Yb-doped fiber laser amplifiers are arranged in master oscillator power amplifier (MOPA) configuration with 10 kHz narrow linewidth non-planar ring oscillator (NPRO) as the common seed source for all the amplifiers at wavelength of 1064 nm. Each fiber amplifier is designed to have three-stage amplification, where the first stage amplifies the 10 mW from the NPRO to 200 mW, the second stage provides amplification to 5 W, and the third stage amplification outputs approximately 150 W of power. P1-P5 represent 5 input beams from the fiber MOPA laser array, P1 is the reference beam for the self-referenced LOCSET used to minimize the phase error between P2-P4 and P1, loss ports are blocked after the MVBGs. As shown in Fig 4.11, except for Laser 2 and 4, the other three fiber amplifiers meet the designed specification. Since coherent beam combining requires each of the input beams to have the same polarization, the linearly polarized light from the NPRO is polarization maintained using the polarization maintaining (PM) fibers throughout the entire fiber amplifier system. As previously mentioned, to mitigate any backward amplification such

as reflection from the output facet or nonlinear effect stimulated Brillouin scattering (SBS), each amplification stage is implemented with fiber pigtailed optical isolator to prevent catastrophic damage to the amplifier system. An external high power free space isolator is in place at the output of each fiber amplifier to prevent scattering light from entering the amplifier.

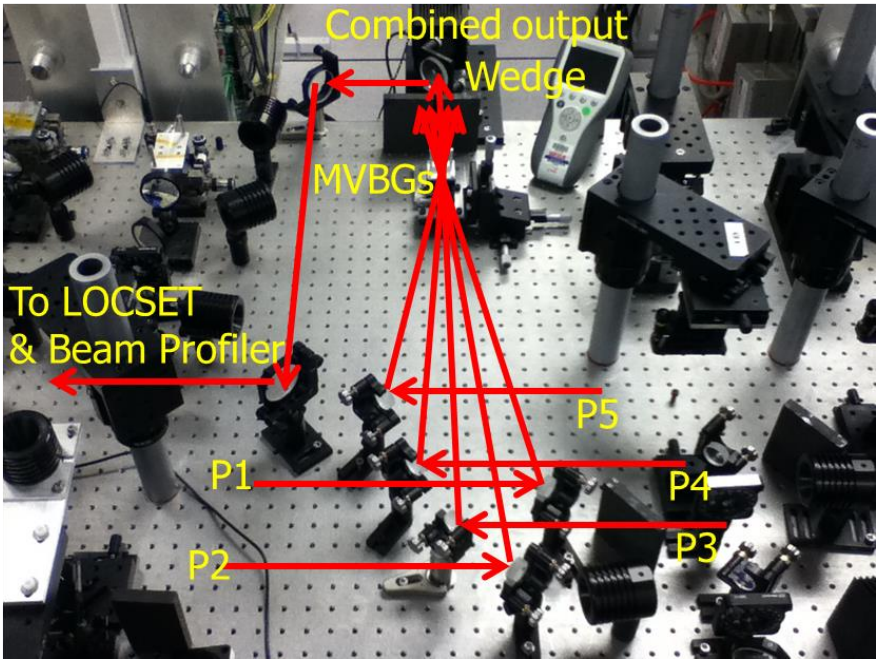

Fig 4.13 Transmissive MVBGs active coherent beam combining experimental setup

For combining five lasers using MVBGs, four sets of holographic Bragg gratings are inscribed in a single PTR glass such that at near normal incident the input splits equally into five outputs under optimal Bragg condition. In the beam combining scenario, the MVBGs overlaps five input beams at different input angles in both near and far field and the combining takes effect when coherence is enforced on the selected output. OptiGrate Inc. fabricated the holographic element using their advanced gratings recording technique involves interferometry and UV lasers. The parameters for the transmissive MVBGs used in the experiments are shown in Table 4.2. The MVBGs is

designed for combining five 1064 nm wavelength lasers at 0°, ±5°, and ±10° incident angles. Fig 4.14 shows the beam profiles of the split beams with input beam incident near normal to the MVBGs. The split beams shows no degradation in beam quality at low input power. The beam splitting efficiencies range from 16.8% to 23%, measured with only P3 on and the power of each diffracted beam is monitored. The diffraction angles are ~±5° and ~±10° with respect to the direction of transmitted incident beam.

Table 4.2 Transmissive MVBGs specifications

Grating	I	II	III	IV
Wavelength (nm)	1064	1064	1064	1064
Grating period (um)	6.35	6.36	12.61	12.67
Tilt (deg)	3.24	-3.19	1.63	-1.58
Input angle (deg)	0.03	0.03	0.03	0.03
Output angle (deg)	9.65	-9.57	4.85	-4.76
Measured diffraction efficiency at 1064 nm and 0.03 deg input angle (%)	18.8	16.8	20.7	20
Transmission at 0.03 deg input angle (%)	23.3			
Thickness (mm)	4.3			
Material loss (%)	0.5			
Reflectivity per surface at 1064 nm (%)	<0.3			
Flatness at 633 nm	0.14λ:0.13λ			
Grating dimensions (mm)	22 x 22			

Each input beam is aligned to the MVBGs with a pair of turning mirrors. The optical alignment starts with P3 incident on the MVBGs at near normal angle and the MVBGs is adjusted so the split beams have near equal powers. The center split beam is passed through the beam blocks and sampled at the wedge for alignment with the

Spiricon beam profiler and the LOCSET photo-detector. Approximately 92% of the total power passes through the wedge and is measured with the power meter. The rest of the laser beams are aligned to P3 on the beam profiler in both near and far field to ensure spatial overlap. Each laser is polarization controlled using a set of half-wave plates and a polarizer to achieve the same linear polarization in the beam combining system. Phase adjustment is controlled using the lithium niobate ($LiNbO_3$) phase modulator at modulation frequency of 100 MHz for the first modulated channel. The modulation frequencies are separated by 3 MHz for the other phase modulated channels in the beam combining system. At 150 W of output power, each fiber amplifier is enhanced with SBS mitigation technique involving linewidth broadening. The enhancement technique is outside the scope of this article and will not be part of the discussion.

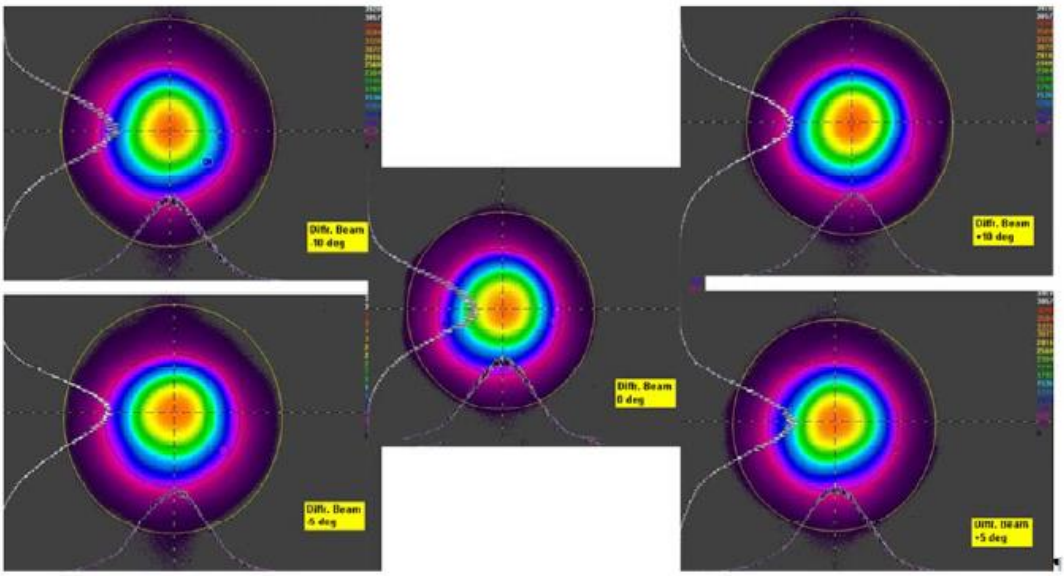

Fig 4.14 Output beam profiles of the split beams with input laser incidents near normal to the transmissive MVBGs

4.2.2 Experimental Results

For minimal temperature effect, we conducted a low power experiment to study the combining efficiency of the MVBGs. The result shows 89% combining efficiency at 1.05 W of total input power. The input powers of the fiber lasers were not all equal. Two of the laser channels produced ~40% less power than the others. Therefore we expected ~10% degradation in the combining efficiency according to the simulation. Next, the total input power was increased to 7 W and 81 W resulting in 5 W and 67 W combined power, respectively. In both cases, we obtained the combining efficiencies of 82% and the results were not influenced by the mismatched power levels. During the experiment, we observed the heating of the MVBGs using the FLIR T250 thermal camera. However the beam quality did not degrade at these two power levels with measured M^2 of 1.2 as shown in Fig 4.16. A careful material study revealed that the source of the heating was from the interface between the PTR glass and the anti-reflective (AR) coating. At even higher input powers, the heating of the MVBG strongly affected the combining efficiency. For input power of 305.6 W, the temperature of the MVBGs increased to over 41 °C as shown in Fig 4.15 and the efficiency decreased to 67% with measured M^2 of 1.8. The degradation of the combined output beam quality was caused by reduced beam quality of one of the fiber laser when operating at high power. Improvements in material quality and coating properties showed mitigation of the heating effects.

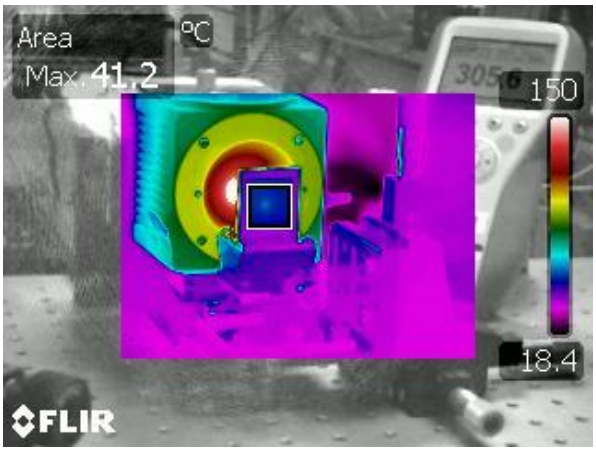

Fig 4.15 MVBGs heating at input power of 305.6 W, left corner shows the maximum temperature of 41.2 °C measured within the MVBGs aperture

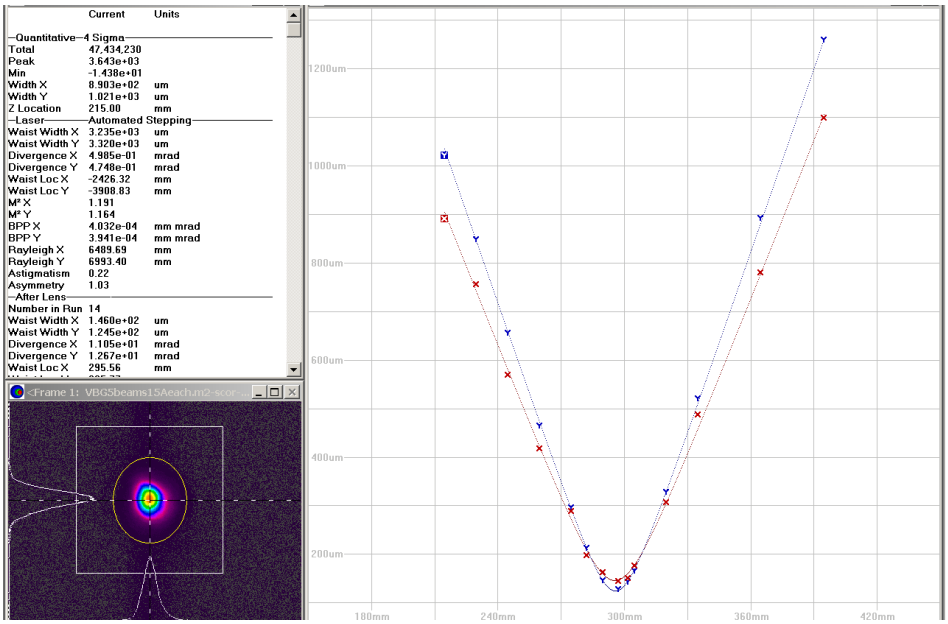

Fig 4.16 Beam quality of the combined output at 67 W, the measurement indicates the combined output is near diffraction limited with M^2 of 1.2

Fig 4.17 shows the active coherent beam combining results for five fiber laser amplifiers using the AR recoated transmissive MVBGs. The result shows greater than 80% combining efficiency achieved with total input power less than 400 W and 70% combining efficiency with 670 W of total input power. Measured beam quality M^2 is 1.3 for input power less than 400 W and 1.6 at 670 W input. Fig 4.18 shows the beam quality

measurement at ~500 W of total input power. Again, the reduced beam quality is mainly due to one of the fiber laser amplifier produces slightly worse beam quality when operating at high power. The slight declination in combining efficiency for optical input power greater than 400 W is caused by heating in the MVBGs as previously described. Fig 4.19 shows a thermal image of the MVBGs with 0.6 kW of incident power with beam diameter of ~3 mm, where the maximum temperature of 44.3 °C is detected within the MVBGs aperture. At 400 W input, the MVBGs stayed below 30°C, which means if the beam diameters were expanded to 1 cm, the MVBGs could handle up to approximately 5.6 kW input power before degradation of the beam combining efficiency.

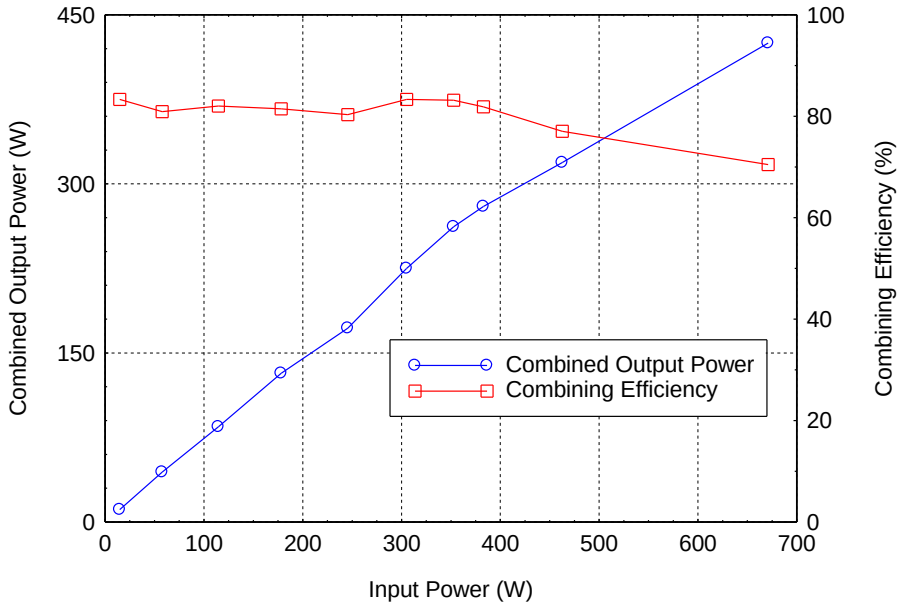

Fig 4.17 Combining efficiency versus total input power with the recoated MVBGs, the combining efficiency remains stable up to 400W of input power

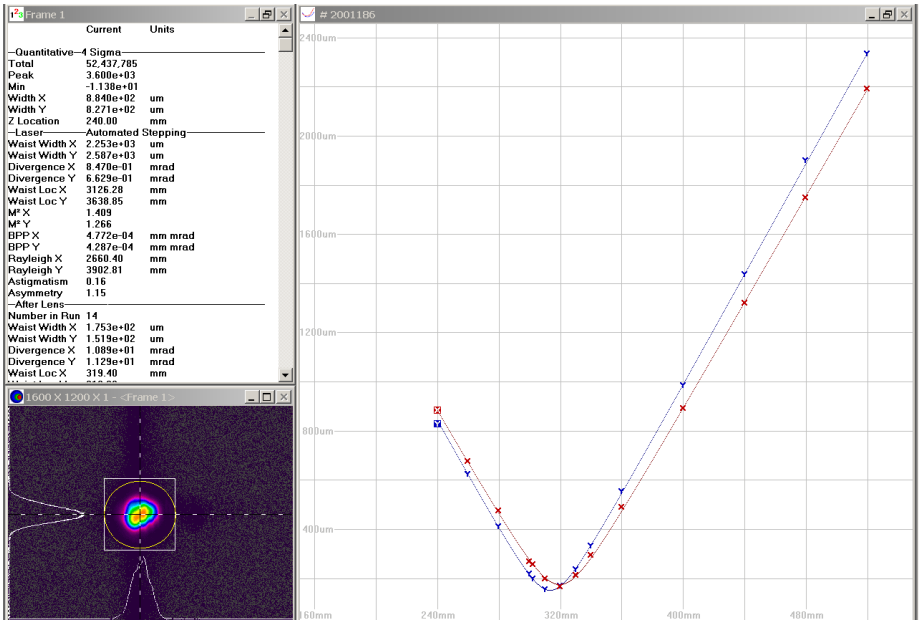

Fig 4.18 Beam quality of the combined output at ~500 W of input power, the combined output has beam quality M^2 of 1.4

Fig 4.19 MVBGs heating at high input power of 0.6 kW, left corner shows the maximum temperature of 44.3 °C measured within the MVBGs aperture

Theoretically, greater than 90% combining efficiency is achievable with the designed transmissive MVBGs; however, degradation factors such as heating of the MVBGs, spatial overlapping on the MVBGs, collimation, polarization, and uneven power between input beams introduce inefficiency for most if not all of the high power coherent beam combining techniques.

4.3 Passive Coherent Beam Combining Using Reflective Multiplexed Volume Bragg Gratings

The second part of the fiber laser beam combining study involves the reflective MVBGs in two passive coherent beam combining schemes. We first implemented the standing wave cavity and experienced high peak power pulsation damaging the fibers at only 500 mW output power. Then we constructed the seeded unidirectional ring cavity and the results showed greater than 90% combining efficiency at 5 W combined output without the pulsation effect. The experimental setups and results are discussed in this section.

4.3.1 Experimental Setup

We report the experimental demonstration of passive coherent beam combination using Yb-doped fiber lasers and the reflective MVBGs. Two beam combining approaches were investigated: standing wave laser cavity and the seeded unidirectional ring cavity. The experimental setups for both designs are shown in Fig 4.20. In both cases, the fiber lasers were implemented using 3 meters of Nufern 10 μm core diameters and 125 μm cladding diameters Yb-doped polarization maintaining gain fibers. In addition, the lasers were optically pumped using the IPG fiber coupled diode lasers with center wavelength ~976 nm. For the standing wave laser cavity setup, one end of the cavity was formed by the broadband fiber Bragg gratings with the center wavelength of 1064 nm and bandwidth of 0.5 nm. The other end of the cavity was formed with a 30% reflectivity output coupler positioned at the common output port of the MVBGs for beam combining purpose. The polarization of each laser was controlled via a set of half-wave plate (HWP) and polarizer.

The experimental setup for the seeded unidirectional ring cavity was similar to the standing wave cavity except each laser was seeded with a narrow linewidth reference laser. The reference laser provided ~10 mW of seed power centered at 1064 nm wavelength with ~10 kHz linewidth for the individual laser. The unidirectional propagation was controlled using an optical isolator (ISO) in each laser. To have the capability of optimizing the output power, we implemented the tunable output coupler using a set of HWP and polarizer positioned at the common output port of the MVBGs.

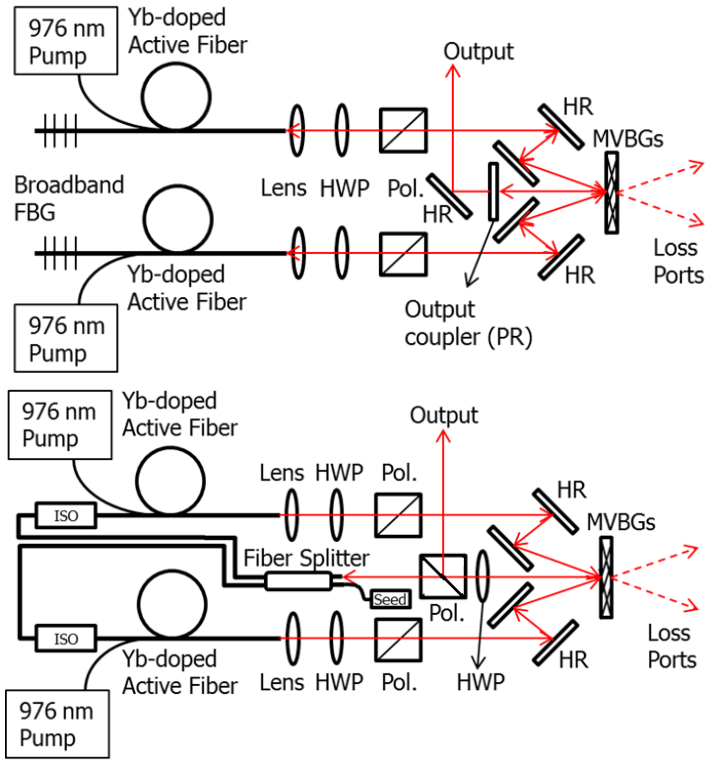

Fig 4.20 Schematics of the standing wave laser cavity and the seeded unidirectional ring cavity

4.3.2 Experimental Results

The spectral characteristic of the reflective MVBGs provided by OptiGrate Inc. is shown in Fig 4.21. For the standing wave cavity, we obtained ~500 mW combined output with good beam quality, M^2 of 1.2. However, the power scalability was limited due to high

gain induced self-pulsation in the active fiber. Reducing the length of the gain fibers could help alleviate the pulsation effect, nevertheless it would also reduce the overall optical to optical efficiency and limit further power scaling. This pulsation effect is rather common in high power fiber laser amplifiers and several methods have been investigated in the past to reduce or eliminate the pulses [59, 60]. Here, in order to mitigate the pulsation effect and concurrently maintain good optical to optical efficiency, we introduced a seed laser and reconfigured the standing wave cavity into a seeded unidirectional ring cavity. Part of the combined output was feedbacked to the second port of the fiber splitter to achieve the coherence between the two fiber laser amplifiers. The beam combining results of the ring cavity is shown in Fig 4.22. We obtained near 90% combining efficiency at 5W combined output calculated using $\eta = \frac{P_{out}}{P_{laser1}+P_{laser2}+P_{loss\ ports}}$. The increased slope efficiency in combined output indicates the coherent addition is taking place. The measured output beam quality is shown in Fig 4.23 with M^2 of ~1.2. The result is limited by the power handling capability of the fiber optical isolators and the fiber splitter in the front end of the beam combining system.

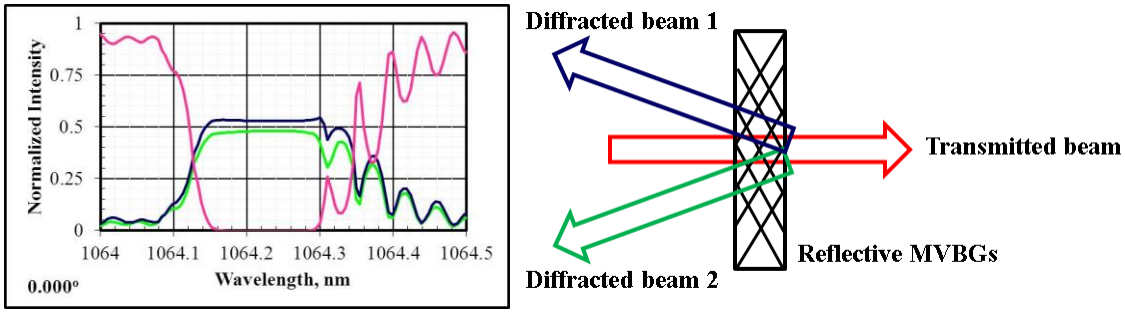

Fig 4.21 Spectral characteristic of the reflective MVBGs

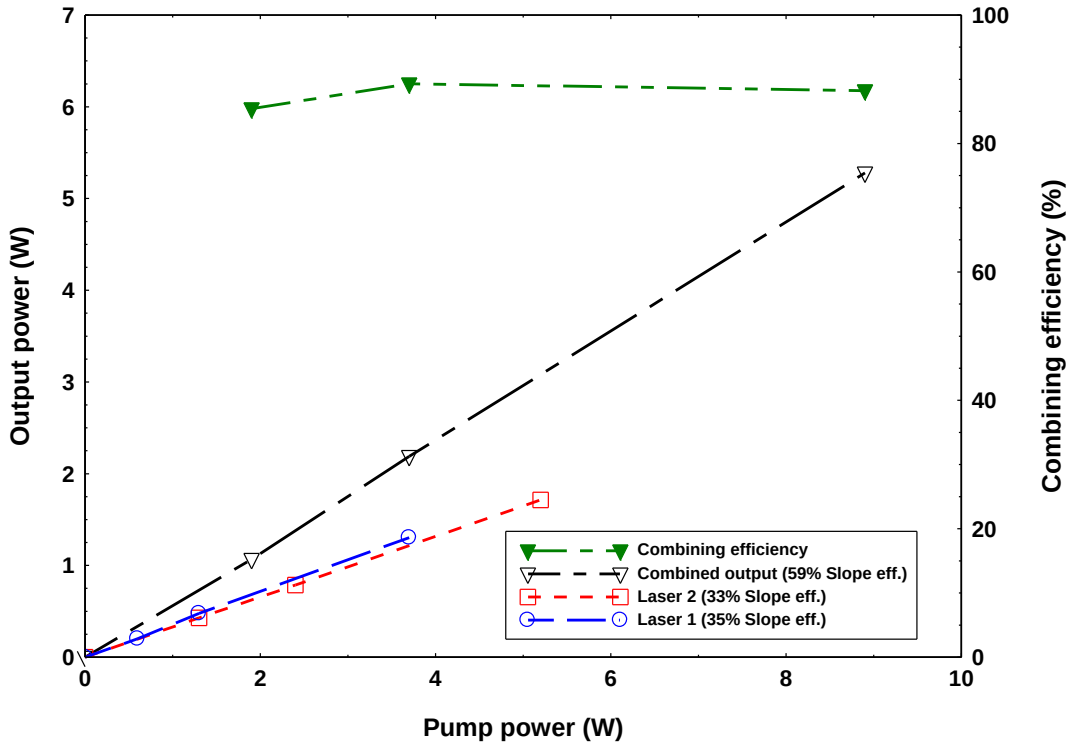

Fig 4.22 Results of coherent beam combining fiber lasers using the seeded unidirectional ring configuration

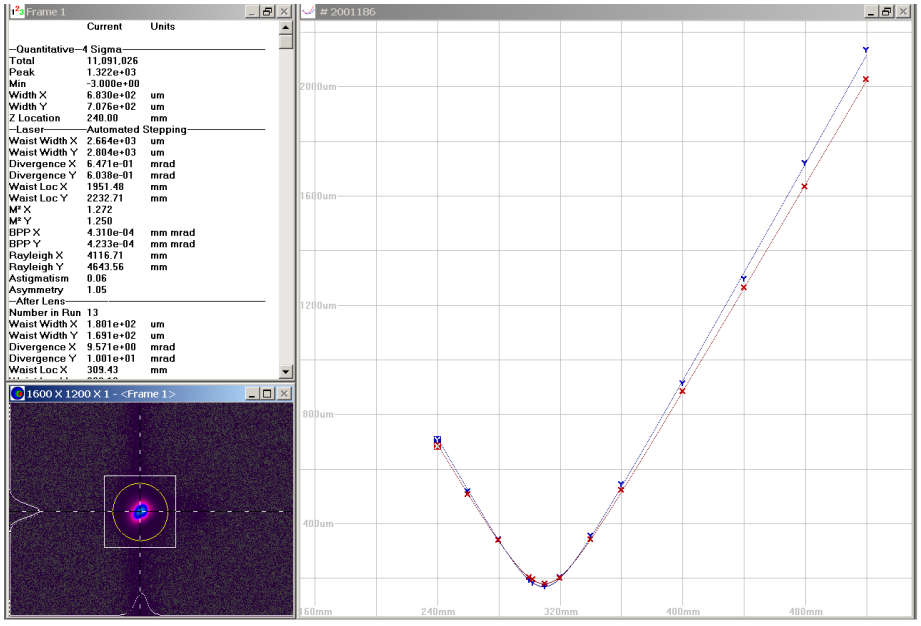

Fig 4.23 Beam quality measurement of the combined output for the seeded unidirectional ring cavity showing M^2 of ~1.2

4.4 Summary

In this chapter, we showed experimental demonstration of fiber laser beam combining using the MVBGs. First we demonstrated the active coherent beam combining of five high power fiber lasers with the transmissive MVBGs. Initially, we were only able to achieve ~70% combining efficiency at input power of ~300 W due to the heating of the MVBGs at the interface of the AR coating and the PTR glass. After reapplying improved AR coating, we achieved ~80% combining efficiency at total input power of 400 W and less. For input power greater than 400 W, we still observed heating of the MVBGs and degradation in beam combining efficiency. Second part of the experimental demonstration of fiber laser beam combining involved the reflective MVBGs in the passive coherent beam combining schemes. In the standing wave cavity setup, we were only able to obtain 500 mW combined output before the fiber amplifiers experienced catastrophic failure due to the self-pulsation effect. In the case of seeded unidirectional ring cavity setup, we achieved ~5 W combined output with ~90% combining efficiency. The combined output also showed good beam quality with M^2 of ~1.2. The scalability of the seeded unidirectional ring cavity design can be increased with fiber components capable of handling higher power. Above all, we have shown the possibilities of high power fiber laser beam combining using both the transmissive and reflective MVBGs. In the next chapter, we will discuss the MVBGs beam combining schemes with high brightness vertical external cavity surface emitting lasers.

Chapter 5 : Experiment on Beam Combining of Vertical External Cavity Surface Emitting Lasers (VECSELs) Using Volume Bragg Gratings

5.1 Introduction to VECSELs and VECSELs Beam Combining

In the past few years, semiconductor vertical external cavity surface emitting lasers (VECSELs) have shown significant improvement in both output power and narrow linewidth wavelength tuning range. Especially in the near infrared wavelength region, the output power from a single gain chip has reached more than 100W of optical power [61]. For narrow linewidth operation, greater than 50nm wavelength tuning range has been demonstrated using a birefringent filter [62]. However, the output power is greatly reduced when applying the linewidth narrowing mechanism. In order to reach higher power with narrow spectral linewidth output, it is necessary to conduct beam combination/power scaling using multiple devices.

Several beam combining/power scaling techniques have been investigated in the past to achieve high power narrow linewidth output. In the case of coherent power addition, it has been demonstrated using two VECSELs in a W-shaped cavity [63]. In a different scenario, spectral beam combination using the volume Bragg gratings (VBGs) as an external combining element has also shown efficient beam combining result [64]. Besides spectral beam combination, another method to incoherently overlap two VECSELs outputs has been demonstrated using a polarizer inside a T-shaped cavity [65]. All above beam combining/power scaling scheme used a birefringent filter placed inside the laser cavity to achieve tunable narrow linewidth output. To the best of our knowledge, there has not been any reported study for beam combining/power scaling multiple VECSELs using VBGs as intracavity element.

Therefore, here we propose to conduct beam combination study using the holographic VBGs arranged inside the VECSELs cavity to achieve both spectral narrowing and beam combining effects. The VBGs are holographic gratings inscribed in a photo-thermal-refractive (PTR) glass using an ultraviolet laser source. Depending on the gratings design, it can be a partial reflector or a high reflector for spectral filtering. It has been shown the VBGs are capable of combining multiple lasers both coherently and incoherently [66]. More recently, we have also conducted experimental study to actively coherent combined five high power fiber laser amplifiers using transmissive multiplexed VBGs (MVBGs) as shown in the previous chapter.

In this chapter, we present two VECSELs beam combination techniques using the VBGs. First, we will show the coherent addition scheme using the VBGs in a Z-shaped cavity. Then we will describe the experimental setup and results of a wavelength beam combining approach using the reflective MVBGs as the combiner in a compound cavity scheme. Before the beam combining discussion, we will first describe the characterization results of the VECSELs used for the beam combining.

5.1.1 Basic VECSELs Setup and Characterization

Since the VECSELs do not have the waveguide structure like the fiber lasers, to beam combine multiple VECSELs requires more elaborated cavity designs. The laser cavity not only has to satisfy the stability criteria, it also needs to match the pump spot size and the cavity mode size on the VECSELs gain chip. In addition, comparing to the fiber lasers, the VECSELs have relatively small laser gain volume and require high reflectivity output coupler to achieve lasing. Thus the MVBGs cavity designs from the previous section are

not suitable for VECSELs as the lasers will not be able to reach lasing threshold for beam combination. Therefore, to demonstrate VECSELs beam combination using VBG, it is important to start with laser cavity analysis and implement beam combining methods base on the stability criteria of the analysis.

Using the standard ABCD ray tracing matrices and the Gaussian beam optics, we simulated on-chip mode sizes and stability regions for two cavity geometries with a range of cavity lengths. The simulation results for the wavelength of 1020 nm are shown in Fig 5.1. Left graph shows the VECSEL cavity analysis for concave output coupler cavity, right graph shows VECSEL cavity analysis with a positive lens (f = 20cm) inside the cavity for three L2 lengths (19cm, 30cm, 40cm). In the experiments, the 808 nm DILAS fiber coupled pump lasers have 400 μm output spot sizes and after reimaging, the pump spot sizes are approximately 280 μm on the VECSELs. In order to obtain the best optical to optical efficiency and good output beam quality, we need to adjust the cavity mode size to match the pump spot size or vice versa. According to the simulation result, for the cavity geometry with concave output coupler (radius of curvature R = 25 cm), there are only two cavity lengths (L ~ 2 cm & 22.5 cm) matched the pump spot size within the stable region. On the other hand, there are several cavity design options available for the lens inserted cavity geometry as shown in the simulation. This cavity is analogous to the coherent addition cavity demonstrated by L. Fan et al. [63], where the lens is replaced by a spherical folding mirror.

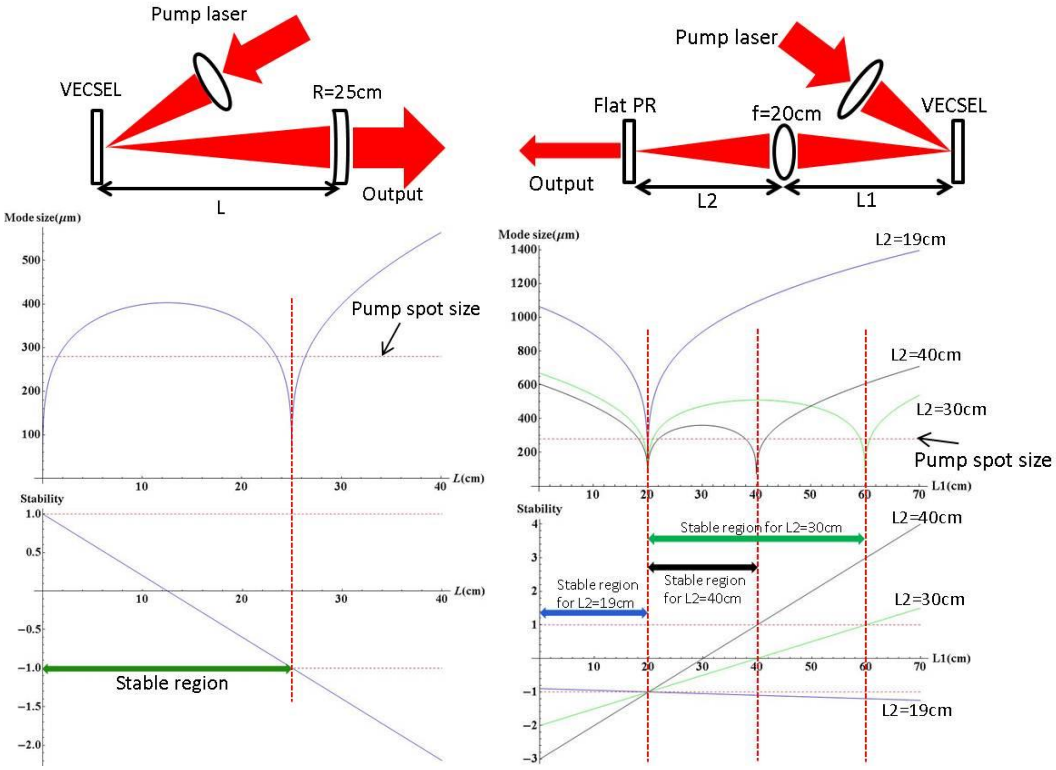

Fig 5.1 Two conventional VECSEL cavity geometries

We tested both cavity geometries to verify suitable range of cavity lengths for the beam combining experiments. The VECSELs used in the experiments consist of a multi-quantum well active region with 12 InGaAs wells and a 25 pair AlAs/GaAs DBRs for operating at near 1020nm wavelength [67]. The VECSELs were water cooled at 10°C using a unique water jet cooling design as shown in Fig 5.2. All characterizing experiment was conducted using 95% reflectivity output coupler. The experimental results with calculated cavity mode sizes are shown in Fig 5.3. Top plot shows the output for concave output coupler cavity and bottom plot shows the output for the lens inserted cavity. In the case of the cavity with concave output coupler (R = 25 cm), greater than 4W output reached with ~20% slope efficiency for cavity lengths greater than 22cm. The cavity either does not lase or with low slope efficiency for cavity lengths between 4.5cm

and 22cm. As shown in the simulation, the cavity mode size starts to match pump spot size again for cavity lengths less than 4.5cm.

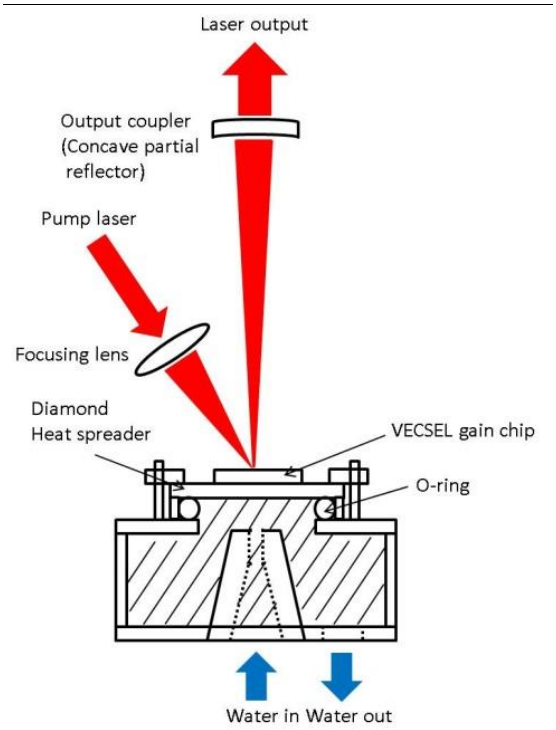

Fig 5.2 VECSELs water jet cooling block diagram and common laser cavity setup

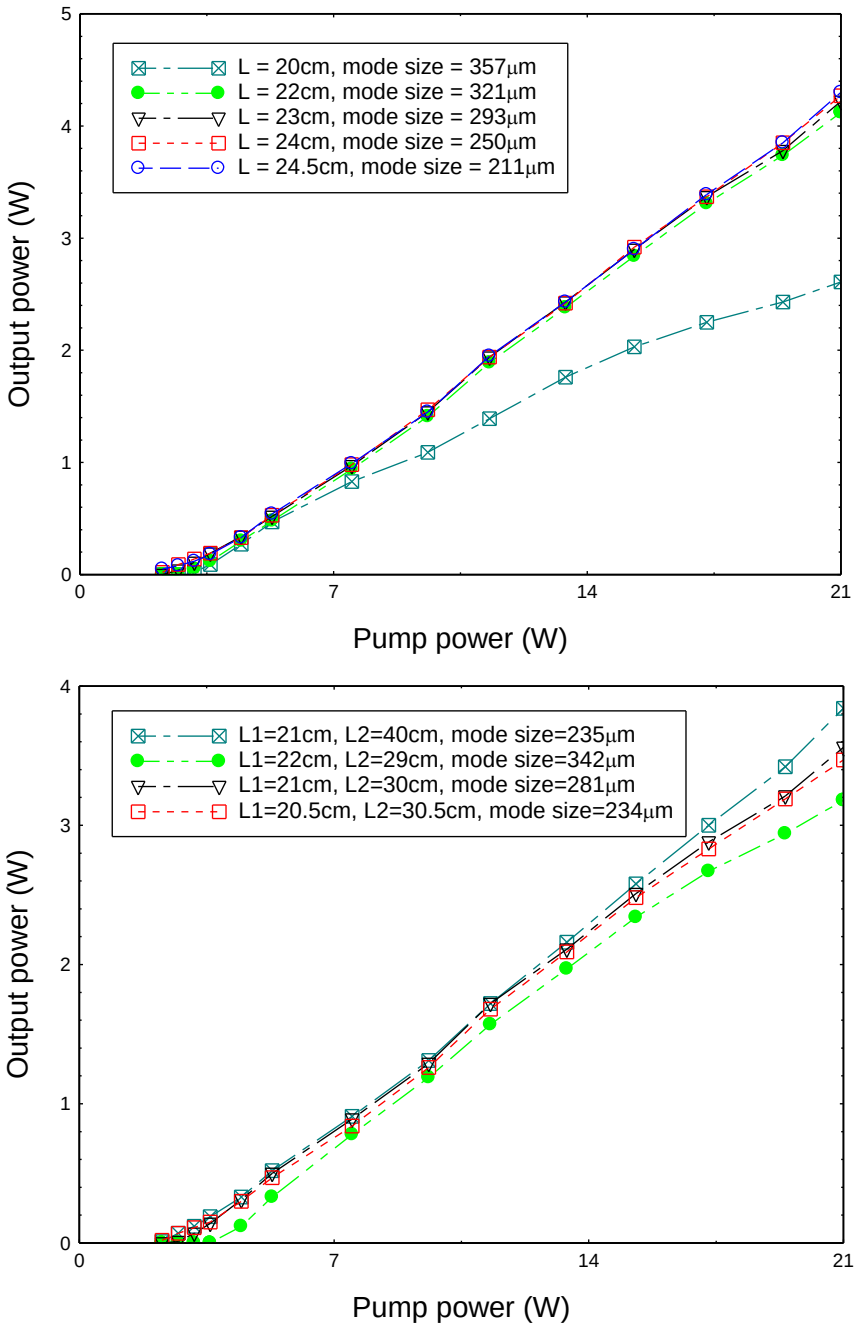

Fig 5.3 Experimental data of single VECSEL output with two different cavity geometries

For the lens inserted cavity, we have obtained ~17% slope efficiency with an average of 3.5W output at 21W of pump power. As expected, there is a slight decrease in slope efficiency due to the intra-cavity lens absorption. We also observed the lens heating up to 50°C with a FLIR thermal camera when applied 21W of pump power. The heating

effect can be mitigated by either replacing the lens with a spherical folding mirror or using a low reflectivity output coupler to reduce intra-cavity power. On the other hand, since the data indicates the lens heating has not caused the output power to rollover at 20 W of pump power, we will continue with lens inserted beam combining cavity without replacing the optics for proof of concept demonstration.

5.2 Coherent Addition Using Volume Bragg Gratings

5.2.1 Experimental Setup

Based on the VECSEL characterization and cavity analysis, we constructed both single VECSEL V-shaped cavity and two VECSELs Z-shaped cavity with either a near 100% high reflectivity mirror (HR) or a VBG at one end of the cavity and a flat 95% reflectivity partial reflector at the output end as shown in Fig 5.4. In order to achieve coherent addition with the Z-shaped cavity, it is critical to adjust the cavity lengths so the mode sizes on both VECSELs are similar to the pump spot sizes. From the lens inserted cavity simulation shown in Fig 5.1, for a positive lens with focal length of 20 cm, both the stability criteria and the mode matching condition are met only when L1 and L2 are slightly less than 40 cm. In terms of the Z-shaped cavity shown below, it translates to both the total cavity length on the left side of the lens (L1 + L3) and the total cavity length on the right side of the lens (L2 + L4) need to be slightly less than 40cm. Furthermore, L3 and L4 will have to be less than 4.5cm to ensure on-chip mode matching. From the discussion above and the physical constraint in the Z-shaped cavity experimental setup, the measured cavity parameters are L1 = 35.7 cm, L2 = 35.1 cm, L3 = 4.2 cm, and L4 = 4.3 cm. We also used the similar cavity parameters (L1 = 35 cm, L2 = 40.5 cm, L3 = 4 cm) for the single VECSEL V-shaped cavity for the purpose of

comparison. The calculated cavity mode sizes on the VECSELs are all around 330μm for both cavity geometries.

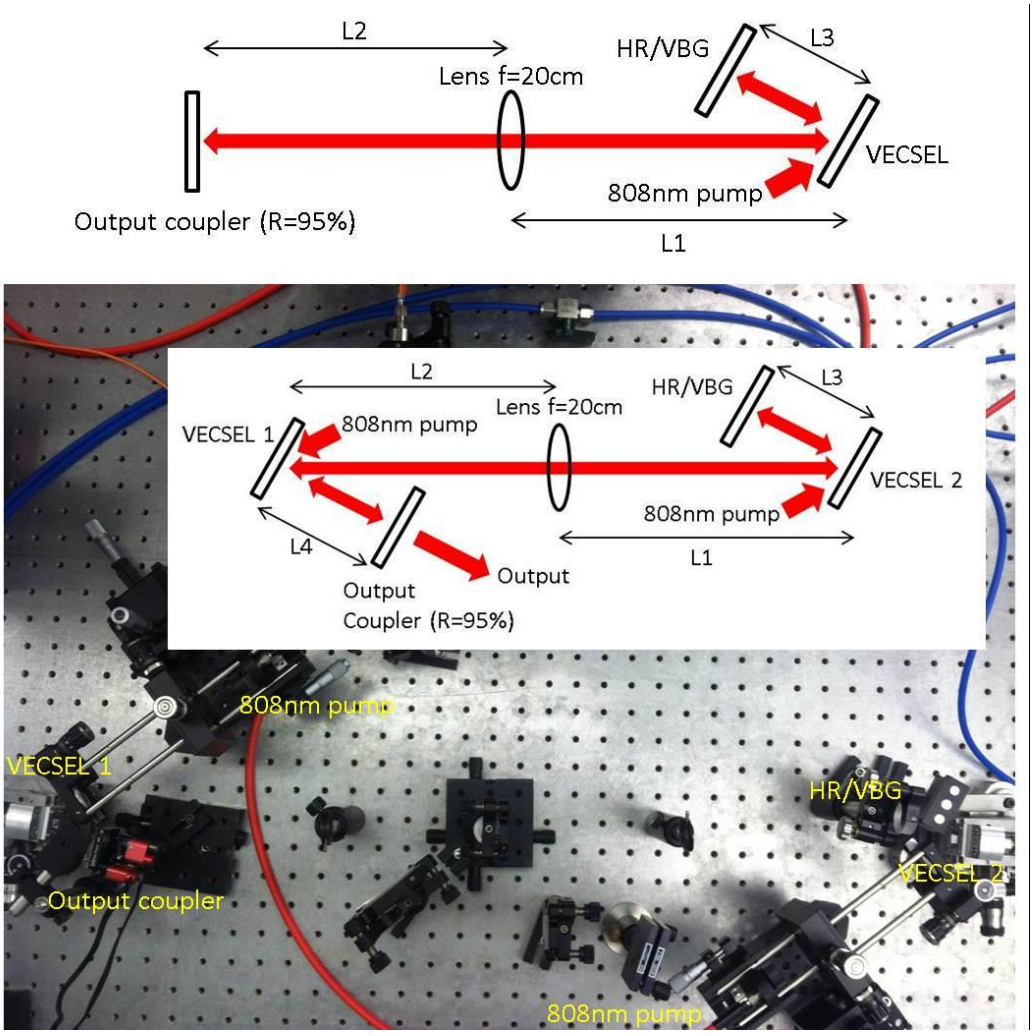

Fig 5.4 Schematic of the single VECSEL V-shaped cavity and the two VECSELs Z-shaped cavity coherent addition experimental setup

5.1.2 Experimental Results

The experimental results for the single chip V-shaped cavity and the two chips coherent addition Z-shaped cavity are shown in Fig 5.5. For the single chip, we obtained 3.23 W output with 15% slope efficiency with the broadband HR and 2.32 W output with 11% slope efficiency with the 1021.7 nm resonated VBG. In the case of the two chips cavity, we obtained 5.03 W output with 11% slope efficiency with the HR and 3.48 W output

with 8% slope efficiency with the VBGs. The decreased slope efficiency from the V-shaped cavity to the Z-shaped cavity is due to the additional cavity loss introduced by the second VECSEL. The slope efficiency decreases further more when replacing the HR with the spectral narrowing VBGs. However, the degradation in slope efficiency is expected as the coherently addition output has much higher stabilized spectral density in the VBGs cavity.

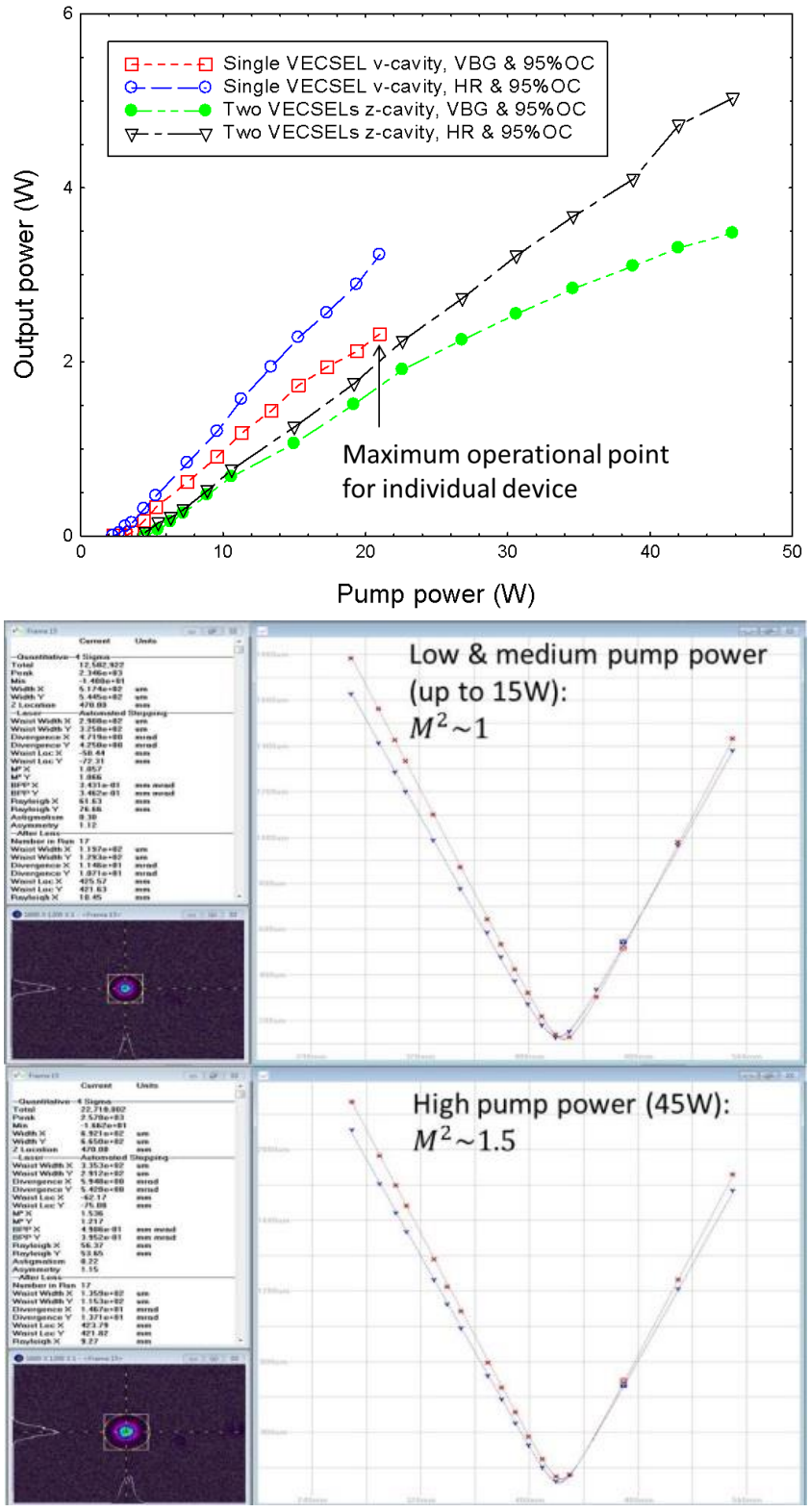

Fig 5.5 Coherent addition experimental results and measured beam quality in the two VECSELs Z-shaped cavity with the VBGs

The measured combined output beam quality is also shown in Fig 5.5. At low and medium pump power, we obtained excellent beam quality of $M^2 \sim 1$; however, the beam quality is slightly degraded ($M^2 \sim 1.5$) due to heating induced higher order mode excitation in the VECSELs at high pump power. The output beam qualities are similar for all the cavity geometries used in the experiment. For the effect of coherent addition, we obtained greater than 70% coherent scaling efficiency for both HR and VBG cavities. The coherent scaling efficiency is calculated using $\eta = \frac{P_{out}(z-cavity)}{2*P_{out}(v-cavity)}$, as both VECSELs have the same output characteristics. The output spectra for the cavities with the broadband HR and the VBGs at different pump powers are shown in Fig 5.6. Left plot shows output spectra for the cavity with the broadband HR and right plot shows spectral narrowed and stabilized output using the VBGs. With the broadband HR, the spectrum is red shifted and broaden at higher pump power. It is also well known that the spectral broadening is due to the conduction band overfilling so multiple frequencies lase simultaneously and the red shifting is caused by the heating on the semiconductor gain materials. The effect of spectral broadening and shifting is mitigated in the case with the 1021.7nm resonated VBG as shown in the plot below.

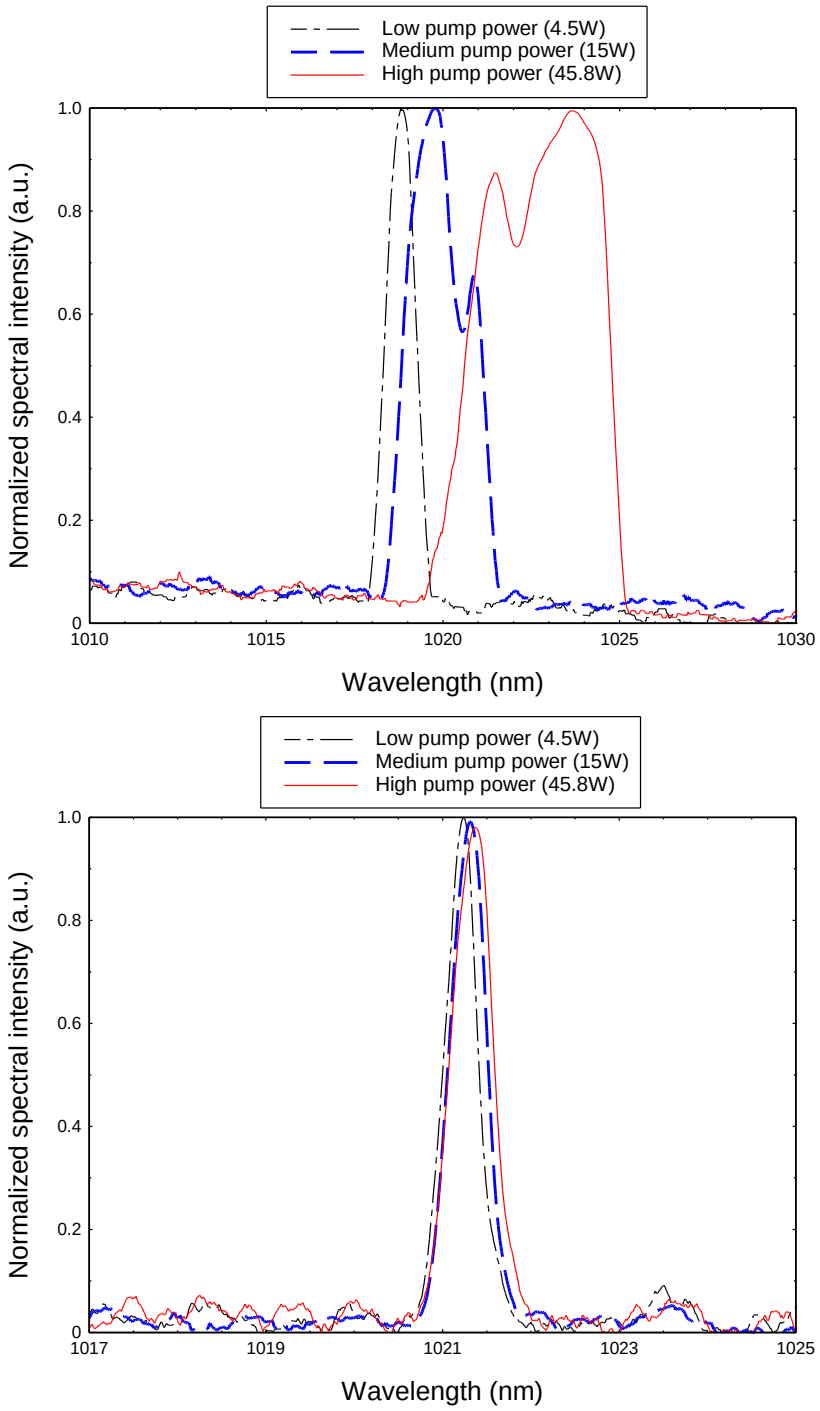

Fig 5.6 Z-shaped cavity combined output spectra at various pump power

Although the output power in the two chips VBGs cavity starts to show signs of rollover at near 30 W of pump power, the output spectrum is still stabilized and frequency locked to the VBGs. To further increase the output in the VBGs cavity, one

can either design the VECSELs to match the resonate frequency of the VBGs at the desired pump power or vice versa and design the VBGs to work more efficiently with the frequency shifted VECSELs. The coherent addition cavity with the HR has not shown power rollover at 45 W of pump power and is capable of producing higher output power without the spectral constraint.

5.2 Spectral Beam Combining Using Multiplexed Volume Bragg Gratings

5.2.1 Experimental Setup

The MVBGs are multiple holographic gratings inscribed in a PTR glass. With proper design and fabrication, the MVBGs can be used to split a single laser beam or combine multiple laser sources at the resonant wavelength. Initially, we intended to coherently combine multiple VECSELs using the reflective MVBGs. However, due to the small gain volume, the VECSELs cavity would not reach lasing threshold with the MVBGs placed inside the cavity. Thus we evolved the coherent beam combining scheme into a more effective wavelength beam combining scheme as shown in Fig 5.7. The reflective MVBGs diffraction characteristics are shown on the top of the graph. By utilizing the short cavities with the concave OC (OC1), we constructed a compound cavity for combining two VECSELs with the reflective MVBGs. The OC1 for the short cavities have radius of curvature of 25 cm and 95% broadband reflectivity. In order to satisfy the stability criteria, the cavity parameters L1 and L2 were adjusted to 4 cm. And the collimating lens were placed outside the short VECSEL cavities with the cavity parameters L3 = L4 ~ 20 cm. The diffraction wavelength for the MVBGs is centered at 1020.9 nm with the angles of diffraction of ±6°.

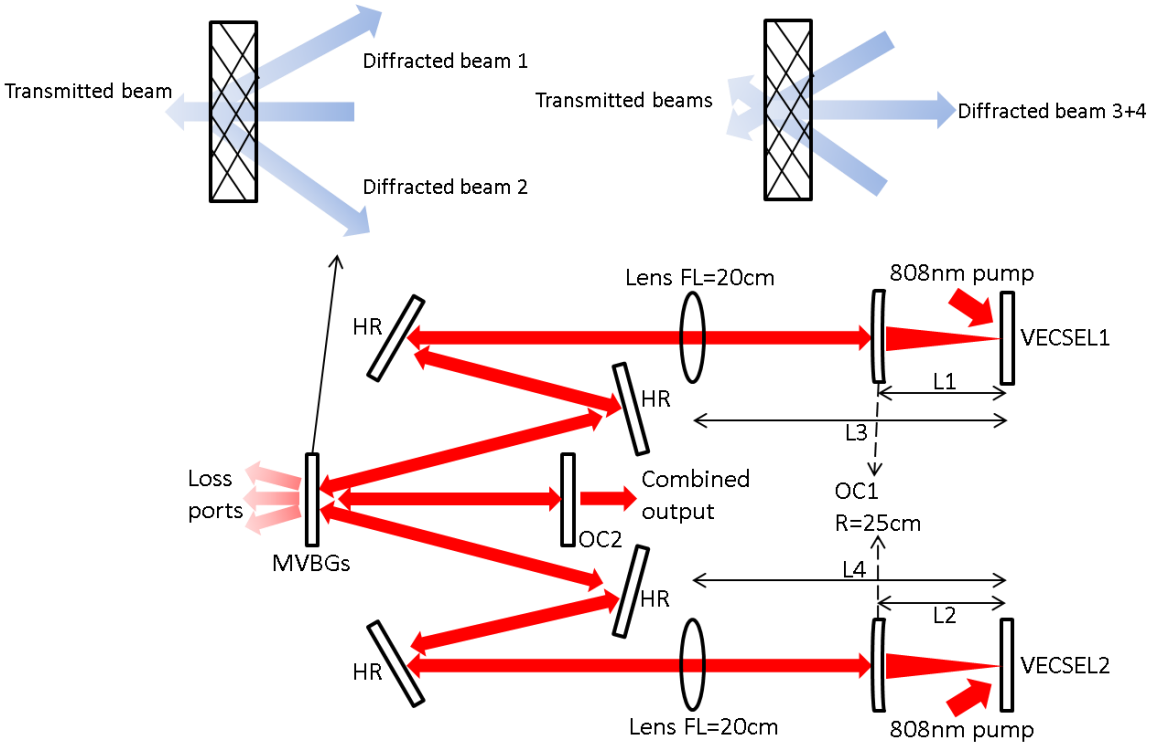

Fig 5.7 VECSELs wavelength beam combining experimental setup using the MVBGs

5.2.2 Experimental Results

The experimental results for the case of 30% and 10% reflectivity OC2 are shown in Fig 5.8 and Fig 5.9, respectively. In Fig 5.8, top plot shows the combined output power characteristic at increased pump power level and bottom plot shows spectra of individual lasers and combined output. Top plot of Fig 5.9 shows the output characteristics and bottom plot shows the measured quality beam M^2 of ~1.2 at 5W combined output. In this compound cavity configuration, we obtained 6.25 W for the 10% reflectivity OC2 and spectrally narrowed combined output with ~100% combining efficiency (calculated as $\eta = \frac{P_{out}}{P_{laser1}+P_{laser2}}$). Similar to the coherent addition experiment, the output power is limited due to the VECSELs emission wavelengths shift outside of the diffraction wavelength of the MVBGs.

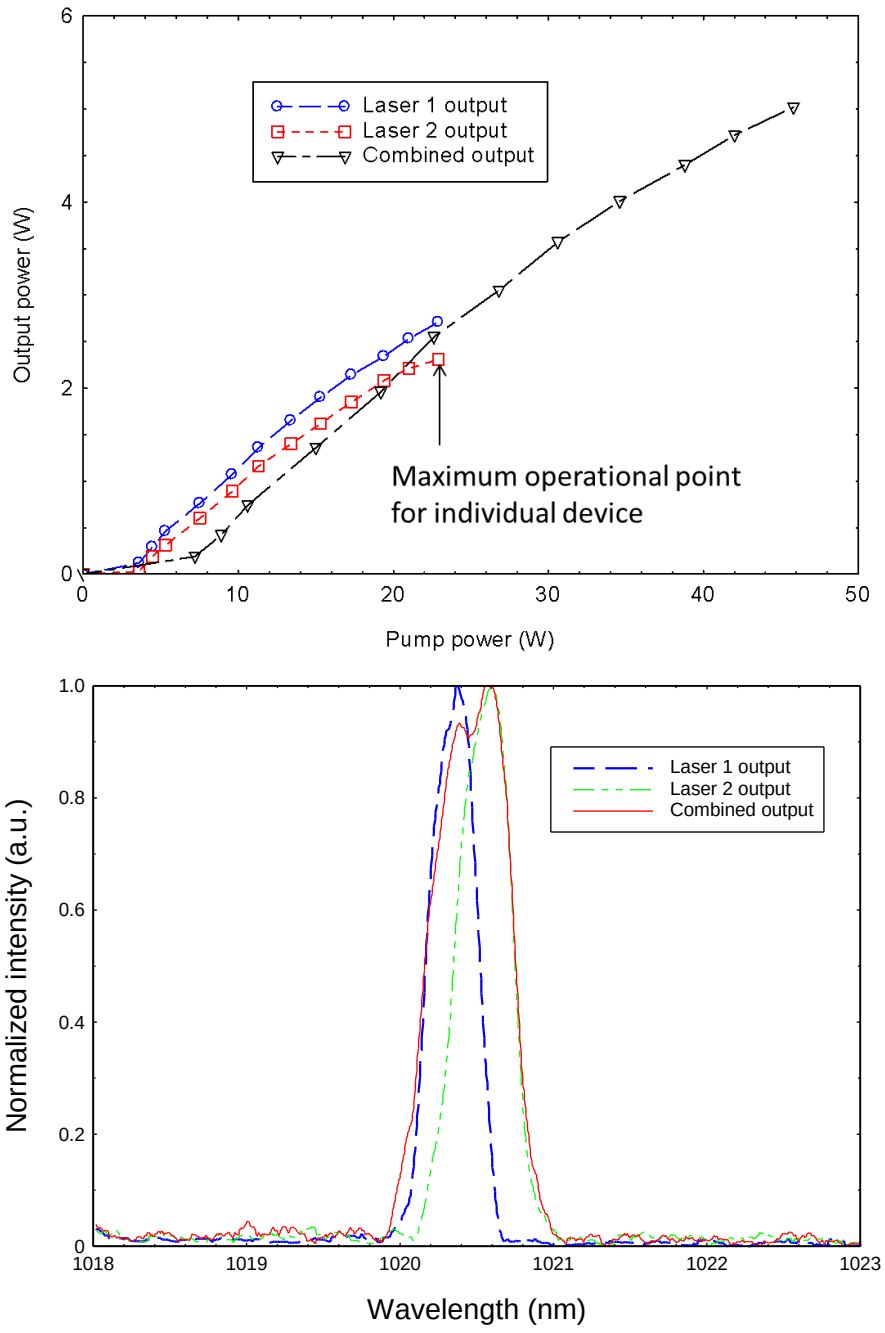

Fig 5.8 Output characteristics with 30% reflectivity output coupler

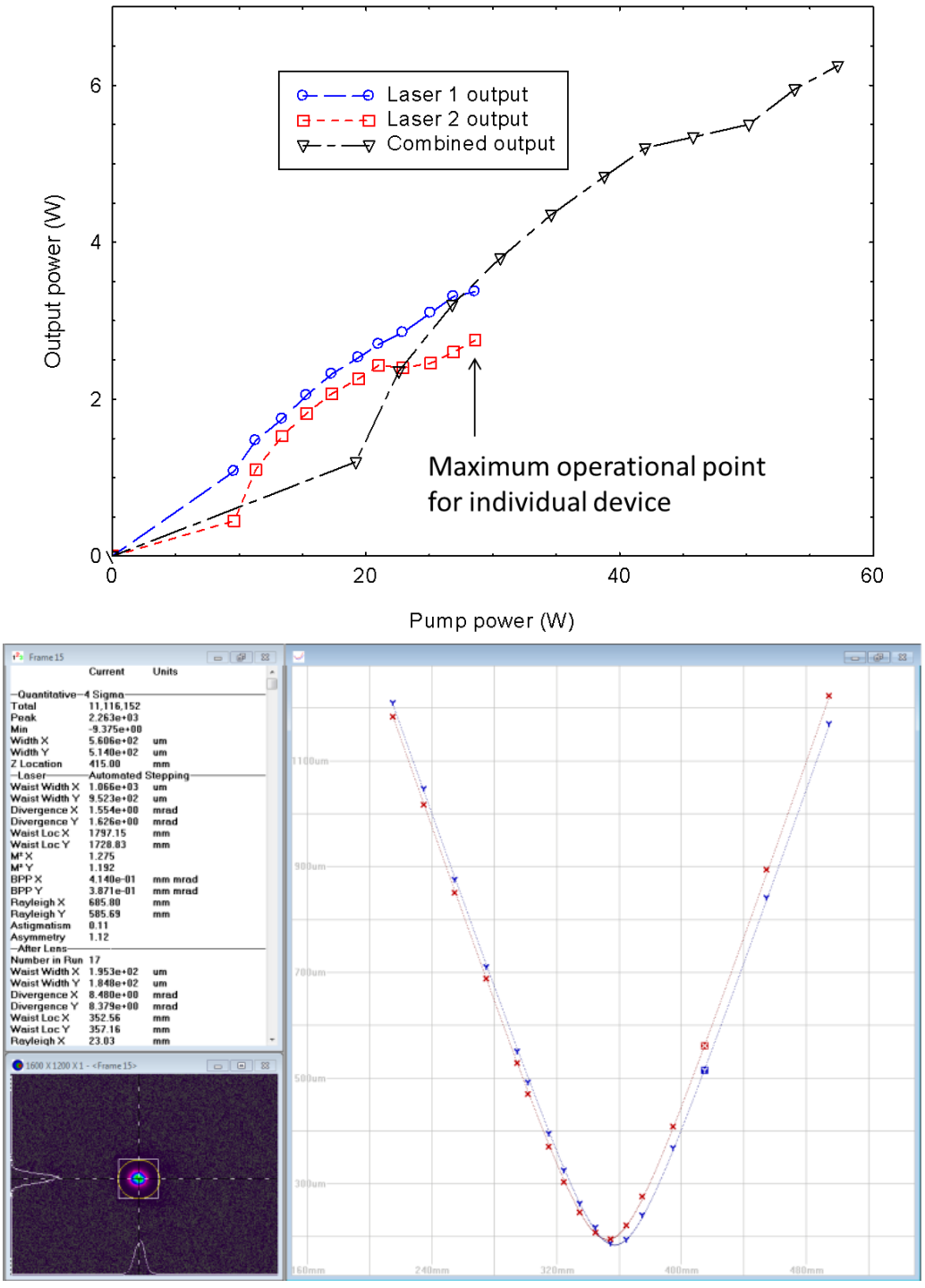

Fig 5.9 Combined output characteristics at increased pump power level with 10% reflectivity output coupler

5.3 Summary

In this chapter, we have demonstrated narrow linewidth coherent addition of two VECSELs using VBGs Z-shaped cavity with >3W output and 8% slope efficiency. In addition, we have also shown an approach to spectrally narrow and combine two VECSELs using the reflective MVBGs in a compound cavity with 6.25 W high spectral density output and ~100% combining efficiency. The combined output in both cases produce near diffraction limited output.

Chapter 6 : Conclusion

In this dissertation, we validated new approaches for beam combining multiple high brightness laser sources using the holographic beam combining element - VBGs. We have first performed the theoretical study of the VBGs and the MVBGs using the coupled wave theory. The simulation shows the combining efficiency is highly sensitive to the thickness of the combiner in the case of the transmissive MVBGs. While the combining efficiency remains constant for the reflective MVBGs, as long as the combiner exceeds the critical thickness. Then we demonstrated the MVBGs beam combining effect experimentally using two types of high brightness laser sources: fiber lasers and VECSELs.

For the fiber lasers, we first constructed the active coherent beam combining experimental study using the transmissive MVBGs and the active phase locking control LOCSET. With five high power fiber lasers, we obtained greater than 80% beam combining efficiency for total input power less than 400 W and 70% combining efficiency at our maximum input power of 670 W. The primary cause of degradation in combining efficiency is due to the heating of the MVBGs at high incident power. We have shown improved beam combining results with the recoated MVBGs. Applying cooling to the MVBGs and/or reducing the incident laser intensities by expanding the beam diameters can further increase the combining efficiency at high input power.

We also implemented the passive coherent beam combining experiment using the reflective MVBGs in two different cavity geometries. In the standing wave cavity, the two fiber amplifiers experienced self-pulsation effect at ~500 mW combined output. To mitigate the pulsation, we employed a reference seed laser and constructed the seeded

unidirectional ring cavity. In this beam combining geometry, we obtained ~90% combining efficiency at ~5 W of combined output.

For the VECSELs, we have demonstrated narrow linewidth coherent addition of two VECSELs using the non-multiplexed VBGs Z-shaped cavity and obtained >3W output and 8% slope efficiency. In addition, we have also shown an approach to spectrally narrow and combine two VECSELs simultaneously. With two VECSELs, we obtained 6.25 W high spectral density output and ~100% combining efficiency using the reflective MVBGs wavelength beam combining compound cavity. In both schemes, the output powers were limited by the redshifted effect in the VECSELs at high pump power. To further increase the combined output power, one can design a matching pair of the MVBGs and the VECSELs to work at the desired wavelength and pump power.

However, the transmission window of the PTR glass decreases significant for the wavelength longer than 2.3μm. It has been demonstrated to efficiently combine several quantum cascade lasers using surface gratings [49], so we believe it is also possible to combine multiple laser devices with longer wavelength using surface gratings with the similar approaches shown in this thesis. The results shown here also enable possibility for implementing efficient hybrid beam combining scheme involves both coherent and incoherent beam combining techniques using single MVBGs.

Appendices

A. LOCSET Theory

Appendix A : LOCSET Theory

LOCSET (locking of optical coherence by single-detector electronic-frequency tagging) is an electronic phase locking approach to establish full-phase correction between the input lasers for coherent beam combining [28] [29] [36]. The technique eliminates the need for a reference laser and only one photo-detector is needed to accomplish the beam combining effect. As mentioned in Chapter 2 and shown in Fig. A.1, LOCSET has two operational configurations: self-referenced phase locking mode and self-synchronous phase locking mode. In the self-referenced phase locking mode, N-1 laser channels are each tagged with a unique RF phase dither that is used to demodulate the phase difference between the untagged laser channel and the rest of the tagged laser channels. Phase modulated laser channels $E_i(t)$ and unmodulated reference laser channel $E_u(t)$ can be expressed as:

$$E_i(t) = E_{io}\cos(\omega_L t + \phi_i(t) + \beta_i \sin(\omega_i t)) \qquad \text{(A-1)}$$

$$E_u(t) = E_{uo}\cos(\omega_L t + \phi_u(t)) \qquad \text{(A-2)}$$

where E_{io} and E_{uo} are the field amplitudes, ω_L represents the laser frequency, and $\phi_i(t)$ and $\phi_u(t)$ are the time dependent phase variation of the modulated and unmodulated lasers, respectively. The term $\beta_i \sin(\omega_i t)$ is the applied sinusoidal phase modulation with β_i as the amplitude and ω_i as the RF modulation frequency.

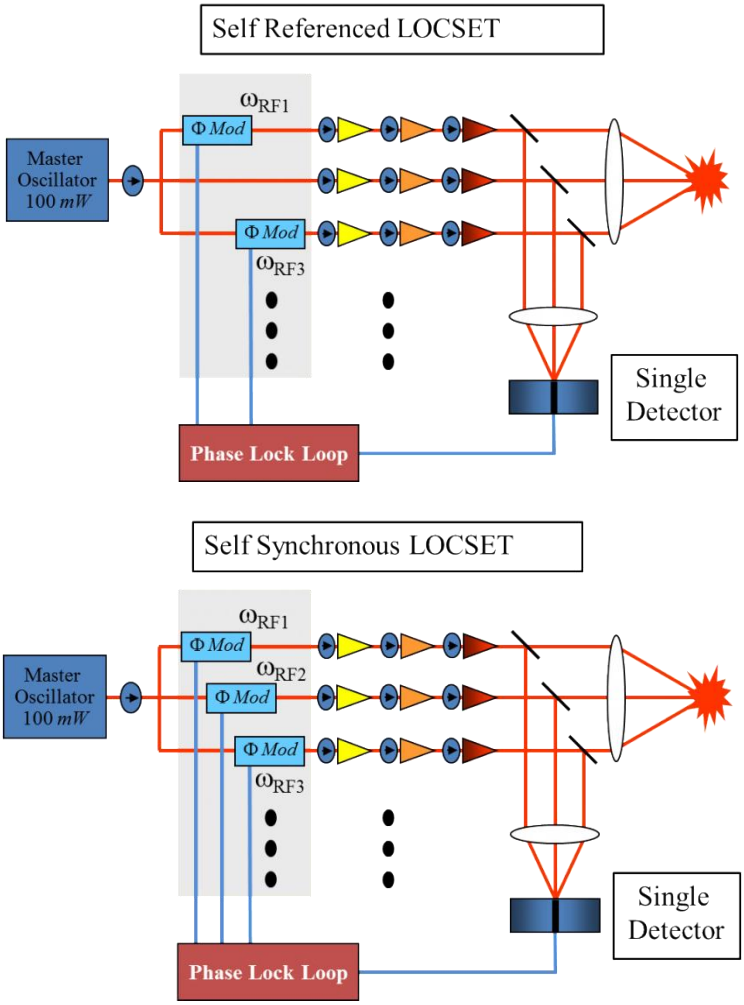

Fig A. 1 LOCSET synchronous multi-dither technique for active coherent combining operated under self-synchronous mode and self-referenced mode

A basic electronic signal processing schematic is shown in Fig. A.2, where the photo-detector collects the sample of the to-be phased laser array and generates the photocurrent that is tagged with a unique RF frequency through the mixer; after integration, each control loop produces a phase error signal that is applied to the phase modulator for phase dithering. The overlapped laser field $E_i(t)$ at the photo-detector is:

$$E_T(t) = E_u(t) + \sum_{i=1}^{N-1} E_i(t) \qquad \text{(A-3)}$$

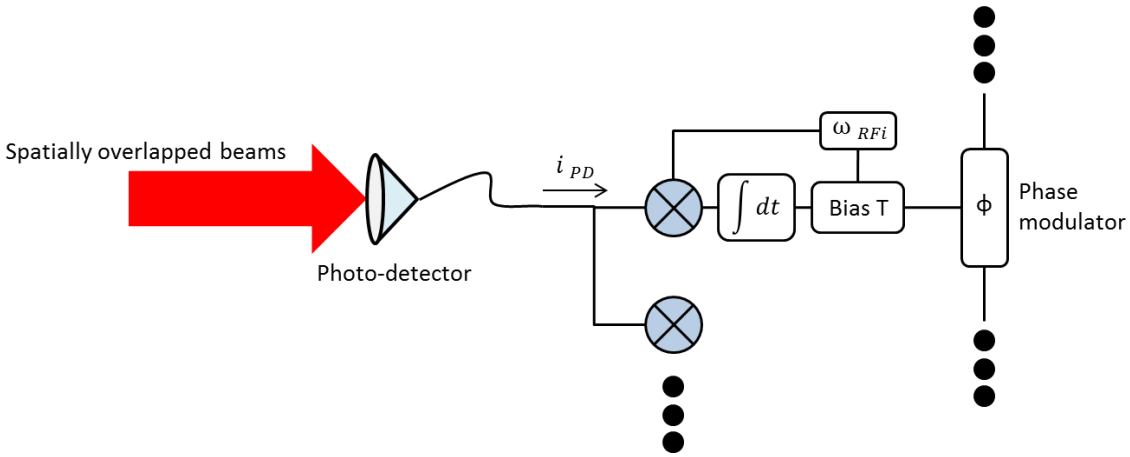

Fig A. 2 LOCSET electronic processing schematic

And the photocurrent $i_{PD}(t)$ produced by the detector can be represented as:

$$i_{PD}(t) = \frac{R_{PD}A}{2}\sqrt{\frac{\varepsilon_0}{\mu_0}}{E_T}^2(t) \qquad \text{(A-4)}$$

where R_{PD} is the responsivity of the photo-detector and A is the active area of the detector. Substituting (A-3) into (A-4) yields:

$$i_{PD}(t) = \frac{R_{PD}A}{2}\sqrt{\frac{\varepsilon_0}{\mu_0}}\left({E_u}^2(t) + 2E_u(t)\sum_{i=1}^{N-1}E_i(t) + \sum_{i=1}^{N-1}E_i(t)\sum_{j=1}^{N-1}E_j(t)\right) \qquad \text{(A-5)}$$

The above expression can be further divided into three components: a photocurrent produced by the unmodulated reference laser source $i_u(t)$, a photocurrent from sum of the interferences between the reference laser and each individual phase modulated laser $i_{uj}(t)$, and a photocurrent formed for sum of the interference between the individual phase modulated lasers $i_{jk}(t)$. The three components then can be expanded as following by substituting (A-1) and (A-2) into (A-5):

$$i_u(t) = \frac{R_{PD}P_u}{2}(1 + \cos(2\omega_L t + 2\phi_u)) \approx \frac{R_{PD}P_u}{2} \qquad \text{(A-6)}$$

$$i_{uj}(t) = R_{PD}\sqrt{P_u}\sum_{j=1}^{N-1}\sqrt{P_j}\left(\cos(\phi_u - \phi_j)\cos(\beta_i\sin(\omega_j t)\right)$$

$$+ \sin(\phi_u - \phi_j)\sin\left(\beta_i \sin\left(\omega_j t\right)\right) \qquad \text{(A-7)}$$

$$i_{jk}(t) = \frac{R_{PD}}{2}\sum_{j=1}^{N-1}\sqrt{P_j}\sum_{k=1}^{N-1}\sqrt{P_k}\,[\cos\left(\phi_k - \phi_j\right)A(k,n_k,t)B\left(j,n_j,t\right)$$

$$-\ \sin\left(\phi_k - \phi_j\right)C(k,n_k,t)B\left(j,n_j,t\right) + \sin\left(\phi_k - \phi_j\right)A(k,n_k,t)D\left(j,n_j,t\right)$$

$$+\ \cos\left(\phi_k - \phi_j\right)C(k,n_k,t)D\left(j,n_j,t\right)] \qquad \text{(A-8)}$$

where P_u is the optical power of the unmodulated reference laser. P_j or P_k are the optical powers of the modulated lasers. The components of (A-8) are represented as:

$$A(k,n_k,t) = J_0(\beta_k) + 2\sum_{n_k=1}^{\infty} J_{2n_k}(\beta_k)\cos(2n_k\omega_k t) \qquad \text{(A-9)}$$

$$B\left(j,n_j,t\right) = J_0\left(\beta_j\right) + 2\sum_{n_j=1}^{\infty} J_{2n_j}\left(\beta_j\right)\cos(2n_j\omega_j t) \qquad \text{(A-10)}$$

$$C(k,n_k,t) = 2\sum_{n_k=1}^{\infty} J_{2n_k-1}(\beta_k)\sin[(2n_k-1)\omega_k t] \qquad \text{(A-11)}$$

$$D\left(j,n_j,t\right) = 2\sum_{n_j=1}^{\infty} J_{2n_j-1}\left(\beta_j\right)\cos[(2n_j-1)\omega_j t)] \qquad \text{(A-12)}$$

where J_n is the n_{th} order Bessel function of the first kind. The photocurrent $i_{PD}(t)$ is then demodulated with an RF demodulation signal $\sin(\omega_c t)$ and integrating over time τ to produce the phase error signal:

$$S_x = \frac{1}{\tau}\int_0^{\tau} i_{PD}(t)\sin(\omega_{cx}t)\,dt \qquad \text{(A-13)}$$

here ω_{cx} represents the demodulation frequency of the x_{th} channel and S_x is the phase error signal of the x_{th} modulated laser channel. After substituting (A-6), (A-7), and (A-8) into (A-13), we obtain the following phase error signal function:

$$S_{SRx} = R_{PD}\sqrt{P_x}J_1(\beta_x)[\sqrt{P_u}\sin\left(\phi_u - \phi_j\right) + \frac{1}{2}\sum_{\substack{j=1\\ j\neq x}}^{N-1}\sqrt{P_j}J_0\left(\beta_j\right)\sin\left(\phi_j - \phi_x\right)] \qquad \text{(A-14)}$$

Ideal phase optimization occurs when the phase error signals proportional to the sinusoid phase difference are minimal, i.e. $\sin\left(\phi_u - \phi_j\right) = \sin\left(\phi_j - \phi_x\right) = 0$.

For operating LOCSET in the self-synchronous mode, the power of the unmodulated reference laser P_u is set to zero thus the phase error signal becomes:

$$S_{SSx} = R_{PD}\sqrt{P_x}J_1(\beta_x)[\frac{1}{2}\sum_{\substack{j=1 \\ j\neq x}}^{N-1}\sqrt{P_j}J_0(\beta_j)\sin(\phi_j - \phi_x)] \quad \text{(A-15)}$$

Here we assume the total number of the phase modulated channels is N. The input lasers are phase locked when $\sin(\phi_j - \phi_x) = 0$.

References

[1] T. H. Maiman, "Stimulated Optical Radiation in Ruby," Nature, 187 4736, pp. 493-494 (1960)

[2] Fan, T. Y. "Heat generation in Nd: YAG and Yb: YAG." *Quantum Electronics, IEEE Journal of* 29.6 (1993): 1457-1459.

[3] G. P. Agrawal, *Nonlinear Fiber Optics*, 4th edn., Academic Press, New York (2007)

[4] E. P. Ippen and R. H. Stolen, "Stimulated Brillouin scattering in optical fibers", Appl. Phys. Lett. 21, 539 (1972)

[5] R.G. Smith, "Optical Power Handling Capacity of Low Loss Optical Fibers as Determined by Stimulated Raman and Brillouin Scattering," Appl. Opt. 11, 2489-2494 (1972)

[6] R.W. Boyd, Nonlinear Optics, Boston: Academic Press, Inc., 1992

[7] V. Roy, M. Piché, F. Babin, and G. W. Schinn, "Nonlinear wave mixing in a multilongitudinal-mode erbium doped fiber laser," Opt. Express **13**(18), 6791–6797 (2005).

[8] J. Rothenberg, "Passive coherent phasing of fiber laser arrays," Proceedings of SPIE 6873, 687315-687315-9 (2008).

[9] J. Bourderionnet, et al, "Collective coherent phase combining of 64 fibers," Opt. Express **19**, 17053 (2011).

[10] Shawn M. Redmond, et al, "Active coherent beam combining of diode lasers," Opt. Lett. **36**, 999-1001 (2011).

[11] Bochove, Erik J. "Theory of spectral beam combining of fiber lasers." *Quantum Electronics, IEEE Journal of* 38.5 (2002): 432-445.

[12] T. Y. Fan, "Laser beam combining for high-power, high-radiance sources", IEEE J. Sel. Top. Quantum Electron. 11 (3), 567 (2005)

[13] Sprangle, Phillip, et al. "Incoherent combining and atmospheric propagation of high-power fiber lasers for directed-energy applications." *Quantum Electronics, IEEE Journal of* 45.2 (2009): 138-148.

[14] Efimov, Oleg M., et al. "Process for production of high efficiency volume diffractive elements in photo-thermo-refractive glass." U.S. Patent No. 6,586,141. 1 Jul. 2003.

[15] O. M. Efimov, L. B. Glebov, and V. I. Smirnov, “High efficiency volume diffractive elements in photo-thermo-refractive glass.” U.S. Patent 6 673 497, 2004

[16] Glebov, Leonid B., et al. "New approach to robust optics for HEL systems." *AeroSense 2002*. International Society for Optics and Photonics, 2002.

[17] Lu, Chunte A., et al. "Coherent Beam Combination of Fiber Laser Arrays via Multiplexed Volume Bragg Gratings." *CLEO: Science and Innovations*. Optical Society of America, 2012.

[18] Lu, Chunte A., et al. "Active coherent superposition of five fiber amplifiers at 670W using multiplexed volume Bragg gratings." *SPIE LASE*. International Society for Optics and Photonics, 2013.

[19] Lu, Chunte A., et al. "Beam combination of multiple vertical external cavity surface emitting lasers via volume Bragg gratings." *SPIE LASE*. International Society for Optics and Photonics, 2014.

[20] Madasamy, Pratheepan, et al. "Dual-grating spectral beam combination of high-power fiber lasers." *Selected Topics in Quantum Electronics, IEEE Journal of* 15.2 (2009): 337-343.

[21] Christian Wirth, Oliver Schmidt, Igor Tsybin, Thomas Schreiber, Ramona Eberhardt, Jens Limpert, Andreas Tünnermann, Klaus Ludewigt, Michael Gowin, Eric ten Have, and Markus Jung, "High average power spectral beam combining of four fiber amplifiers to 8.2 kW," Opt. Lett. **36**, 3118-3120 (2011)

[22] Hamilton, Charles E., et al. "High-power laser source with spectrally beam-combined diode laser bars." *Lasers and Applications in Science and Engineering*. International Society for Optics and Photonics, 2004.

[23] Mark Kimmel, et al. "Dual wavelength laser damage testing for high energy lasers", Proc. SPIE 7842, Laser-Induced Damage in Optical Materials: 2010, 78421O (December 02, 2010);

[24] Giet, S., et al. "Spectral narrowing and locking of a vertical external-cavity surface-emitting laser using an intracavity volume Bragg grating." (2006).

[25] Drachenberg, Derrek, et al. "High-power spectral beam combining of fiber lasers with ultra high-spectral density by thermal tuning of volume Bragg gratings." *SPIE LASE*. International Society for Optics and Photonics, 2011.

[26] Divliansky, Ivan, et al. "Multiplexed volume Bragg gratings for spectral beam combining of high power fiber lasers." *SPIE LASE*. International Society for Optics and Photonics, 2012.

[27] David J. Brady, "Multiplex sensors and the constant radiance theorem," Opt. Lett. 27, 16-18 (2002)

[28] Thomas M. Shay, "Theory of electronically phased coherent beam combination without a reference beam," Opt. Express **14**, 12188-12195 (2006)

[29] Shay, Thomas M., et al. "Self-synchronous and self-referenced coherent beam combination for large optical arrays." *Selected Topics in Quantum Electronics, IEEE Journal of* 13.3 (2007): 480-486.

[30] Vorontsov, M. A., and V. P. Sivokon. "Stochastic parallel-gradient-descent technique for high-resolution wave-front phase-distortion correction." *JOSA A* 15.10 (1998): 2745-2758.

[31] Zhou, Pu, et al. "Coherent beam combining of fiber amplifiers using stochastic parallel gradient descent algorithm and its application." *Selected Topics in Quantum Electronics, IEEE Journal of* 15.2 (2009): 248-256.

[32] Yu, C. X., et al. "Coherent combining of a 4 kW, eight-element fiber amplifier array." *Optics letters* 36.14 (2011): 2686-2688.

[33] Vorontsov, Mikhail A., and Svetlana L. Lachinova. "Laser beam projection with adaptive array of fiber collimators. I. Basic considerations for analysis." *JOSA A* 25.8 (2008): 1949-1959.

[34] Jones, David C., et al. "Beam steering of a fiber-bundle laser output using phased array techniques." *Lasers and Applications in Science and Engineering*. International Society for Optics and Photonics, 2004.

[35] Bruesselbach, Hans, et al. "Power-scalable phase-compensating fiber-array transceiver for laser communications through the atmosphere." *JOSA B* 22.2 (2005): 347-353.

[36] Shay, Thomas M., et al. "Coherent Beam Combining of Fiber Amplifiers in a kW Regime." (2011).

[37] H. Dammann, "Color separation gratings," Appl. Opt. **17**, 2273-2279 (1978)

[38] Redmond, Shawn M., et al. "Diffractive coherent combining of a 2.5 kW fiber laser array into a 1.9 kW Gaussian beam." *Optics letters* 37.14 (2012): 2832-2834.

[39] Thielen, Peter A., et al. "Two-dimensional diffractive coherent combining of 15 fiber amplifiers into a 600 W beam." *Optics letters* 37.18 (2012): 3741-3743.

[40] Uberna, Radoslaw, Andrew Bratcher, and Bruce G. Tiemann. "Coherent polarization beam combination." *Quantum Electronics, IEEE Journal of* 46.8 (2010): 1191-1196.

[41] Moore, Gerald T. "Binary coherent beam combination with mirror pairs." *Applied optics* 41.30 (2002): 6399-6409.

[42] Talbot, Hy Fox. "XLIV. Experiments on light." *The London and Edinburgh Philosophical Magazine and Journal of Science* 5.29 (1834): 321-334.

[43] Lucas-Leclin, Gaelle, et al. "External-cavity designs for phase-coupled laser diode arrays." *High Power Diode Lasers and Systems Conference, 2009. HPD 2009*. IEEE, 2009.

[44] Wrage, M., et al. "Phase locking in a multicore fiber laser by means of a Talbot resonator." *Optics letters* 25.19 (2000): 1436-1438.

[45] C. J. Corcoran and F. Durville, "Experimental demonstration of a phase-locked laser array using a self-Fourier cavity," *Applied Physics Letters* **86**(20), 201118 (2005)

[46] Loftus, Thomas H., et al. "Four-channel, high power, passively phase locked fiber array." *Advanced Solid-State Photonics*. Optical Society of America, 2008.

[47] Shirakawa, Akira, et al. "Coherent addition of fiber lasers by use of a fiber coupler." *Optics Express* 10.21 (2002): 1167-1172.

[48] Wang, Baishi, et al. "All-fiber 50 W coherently combined passive laser array." *Optics letters* 34.7 (2009): 863-865.

[49] Bloom, Guillaume, et al. "Passive coherent beam combining of quantum-cascade lasers with a Dammann grating." *Optics letters* 36.19 (2011): 3810-3812.

[50] Jain, Apurva, et al. "Passive coherent locking of fiber lasers using volume Bragg gratings." *SPIE LASE*. International Society for Optics and Photonics, 2010.

[51] Cowley, John Maxwell. Diffraction physics. Elsevier, 1995.

[52] H. Kogelnik, "Coupled wave theory for thick hologram gratings," The Bell System Technical Journal **48**, 2909–2947 (1969).

[53] E. Honea, et al. "Spectral Beam Combining of Fiber Lasers for Power Scaling," in Lasers, Sources, and Related Photonic Devices, OSA Technical Digest, 2012, paper AW3A.1.

[54] L. Liu, et al. "Phase-locking of tiled fiber array using SPGD feedback controller," Proc. SPIE 5895, 58950P (2005).

[55] R. Paschotta, et al. "Ytterbium-doped fiber amplifiers," IEEE Journal of Quantum Electronics, vol. 33, no. 7, pp. 1049–1056, 1997.

[56] H. M. Pask, et al. “Ytterbium-doped silica fiber lasers: versatile sources for the 1-1.2 _m region,” IEEE Journal Selected Topics in Quantum Electronics, vol. 1, no. 1, pp. 2–13, 1995.

[57] C. Barnard, P. Myslinski, et al. “Analytical model for rare-earth-doped fiber amplifiers and lasers,” IEEE Journal of Quantum Electronics, vol. 30, pp. 1817–1830, 1994.

[58] Cheo, Peter, ”Fiber Optics & Optoelectronics,” Prentice Hall, New Jersey, 1990.

[59] Luo, Liguo, and P. L. Chu, "Suppression of self-pulsing in an erbium-doped fiber laser." *Optics letters* 22.15 (1997): 1174-1176.

[60] Guan, W., and J. R. Marciante. "Complete elimination of self-pulsations in dual-clad ytterbium-doped fiber lasers at all pumping levels." *Optics letters* 34.6 (2009): 815-817.

[61] Heinen, B., et al., “106 W continuous-wave output power from vertical-external-cavity surface-emitting laser,” Electronics Letters, Volume 48, Issue 9 (2012)

[62] T. Leinonen, et al.," High power (23W) vertical external cavity surface emitting laser emitting at 1180 nm ", Proc. SPIE 8606, Vertical External Cavity Surface Emitting Lasers (VECSELs) III, 860604 (February 18, 2013)

[63] Li Fan, et al., "Extended Tunability in a Two-Chip VECSEL," Photonics Technology Letters, IEEE, vol.19, no.8, pp.544,546, April15, 2007

[64] Chris Hessenius, et al., “High-power tunable two-wavelength generation in a two chip co-linear T-cavity vertical external-cavity surface-emitting laser,” Applied Physics Letters 101, 121110 (2012)

[65] Yushi Kaneda, et al., “High Brightness Spectral Beam Combination of High-Power Vertical-External-Cavity Surface-Emitting Lasers,” IEEE Photonics Technology Letters, Vol. 18, No. 17 (2006)

[66] Oleksiy Andrusyak, et al., “Spectral Combining and Coherent Coupling of Lasers by Volume Bragg Gratings,” IEEE Journal of Selected Topics in Quantum Electronics, Vol. 15, No. 2 (2009)

[67] Alexander R. Albrecht, et al., “Progress towards cryogenic temperatures in intra-cavity optical refrigeration using a VECSEL,” Proc. Of SPIE 8638, Laser Refrigeration of Solids VI, 863805-1 (2013)